Design and Realisation of High Accuracy Emissivity Measurement Instruments for Radiation Thermometry

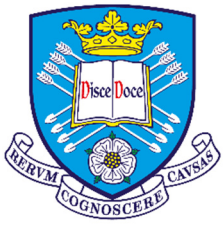

The University Of Sheffield.

Chengxi Zhu

Department of Electronic and Electrical Engineering

University of Sheffield

This thesis is submitted for the degree of

Doctor of Philosophy

November 2019

Acknowledgement

I would like to express my sincere gratitude to my supervisor, Dr. Jon Willmott, for giving me such a wonderful opportunity to be a PhD student at the University of Sheffield and for his continuous encouragement, guidance, and advice. I also want to thank Dr. Cornelia Rodenburg for her valuable knowledge and experience in the area of scanning electron microscopy. I am grateful for Prof. John David for sharing his expertise and advice for my PhD studies, helping me to plan my academic career. I would also like to acknowledge the Department of Electronic and Electrical Engineering and EPSRC for my research funding.

This work would not have been done without the help from the Kroto Research Institute. I am in debt to Dr. L. Ma and Dr. P. Zeng for teaching the sample preparation and the electron microscope operation. I would like to give special thanks to Dr. R. Masters for his efforts on observing and analysing the surface condition of oxidised samples.

I appreciate the friendship and discussion with all the members of sensor system group; Dr. M. Hobbs, Dr. R. Hodgkinson, Dr. T. Rockett, A. Heeley, L. Stanger, M. Davies, M. Grainger, M. Stuart, and N. Boone. I would particularly acknowledge Dr. M. Hobbs for his advice and comments on my publications, and for his great help on developing electrical circuits for emissivity measurements. I would also like to thank N. Boone for training the equipment in iForge. I am also grateful to the whole EEE staff, particularly I. Wraith and S. Dorward, for their help on developing instruments for this work.

Finally, I thank my family, particularly my parents, for all of their care and support through my time in Sheffield, which I sincerely appreciate.

Abstract

Emissivity is the quantity representing the radiative properties of materials that must be prior measured precisely to undertake accurate measurements for radiation thermometry. This work presents the development and validation of three emissivity measurement instruments to undertake studies on emissivity behaviours for materials with complex surface conditions from 200 to 1150 °C. These instruments aim to offer accurate emissivity references for use in non-contact temperature measurements and materials science.

The first instrument was developed to compare the measurement uncertainty between direct and indirect methods from 200 to 450 °C. With use of a pair of cups coated by Vantablack® and gold respectively, the instrument can achieve three different measurement methods: gold-cup (indirect), black-cup (direct), and dual-cup (in-situ direct) methods. The dual-cup method was firstly invented in this work to eliminate the temperature deviation between a blackbody and a sample. The studies offered the guidance in the selection of appropriate methods for emissivity measurements, with respect to prior properties of materials.

This work firstly achieved the Monte Carlo simulation on the ray tracing of a gold-cup. This method is a key technique for investigating the relation of emissivity enhancement and the geometric properties of a gold-cup. The related studies can be used for solving the problem on the optimisation of gold coated reflectors in temperature measurements which has existed since the invention of this method.

The second instrument was developed with a controlled atmosphere to study the impacts on emissivity variations due to the surface condition change from 700 to 1150 °C. By using this instrument, the observations successfully presented the connection between emissivity variations and the surface condition changes of stainless steel 304 (SS304) during the oxidation process. Studies on SS304 proved that the surface condition change, including the chemical composition and surface roughness, dominated the emissivity variation of objects. This instrument offered the capability for industry to measure the

emissivity with the consideration of the actual atmosphere and to trace the emissivity change due to the oxidation process.

At last, a scanning instrument was developed based on a MEMS mirror for producing 160 × 120 pixel emissivity maps across the target from 500 to 1100 °C. Each pixel on the map represented an independent emissivity measurement with fully characterised uncertainty estimation. This instrument was capable of outputting the live emissivity map of an object heated under a complex environment, and therefore, to trace the detailed emissivity variation over the whole scene.

List of publications

C. Zhu, M. J. Hobbs, and J. R. Willmott, "An accurate instrument for emissivity measurements by direct and indirect methods," Measurement Science and Technology, vol. 31, no. 4, pp. 044007, 2020.

C. Zhu, M. J. Hobbs, R. C. Masters, C. Rodenburg, and J. R. Willmott, "An Accurate Device for Apparent Emissivity Characterisation in Controlled Atmospheric Conditions up to 1423 K," *IEEE Transactions on Instrumentation and Measurement,* vol. 69, no. 7, pp. 4210-4221, 2020.

C. Zhu, M. J. Hobbs, M. P. Grainger, and J. R. Willmott, Design and realization of a wide field of view infrared scanning system with an integrated micro-electromechanical system mirror," *Applied Optics,* vol. 57, no. 36, pp. 10449, 2018.

M. J. Hobbs, **C. Zhu**, M. P. Grainger, C. H. Tan, and J. R. Willmott, "Quantitative traceable temperature measurement using novel thermal imaging camera," *Optics express,* vol. 26, no. 19, pp. 24904-24916, 2018.

N. Boone, **C. Zhu**, C. Smith, I. Todd, and J. R. Willmott, "Thermal near infrared monitoring system for electron beam melting with emissivity tracking," Additive Manufacturing, vol. 22, pp. 601-605, 2018.

M. J. Hobbs, M. P. Grainger, **C. Zhu**, C. H. Tan, and J. R. Willmott, "Quantitative thermal imaging using single-pixel Si APD and MEMS mirror," Optics express, vol. 26, no. 3, pp. 3188-3198, 2018.

G. Meyers, **C. Zhu**, M. Mayfield, D. D. Tingley, J. Willmott, and D. Coca, "Designing a Vehicle Mounted High Resolution Multi-Spectral 3D Scanner: Concept Design," in Proceedings of the 2nd Workshop on Data Acquisition to Analysis, 2019, pp. 16-21.

Glossary of terms

Symbol in Radiometry

a	Projected area	m^2
A	Area	m^2
C_s	Specific heat capacity of a sample	$J \cdot Kg^{-1} \cdot K^{-1}$
E	Irradiance	$W \cdot m^{-2}$
G	Geometrical factor in gold-cup method	
I	Radiant intensity	$W \cdot sr^{-1}$
I_0	Radiant intensity along normal direction	$W \cdot sr^{-1}$
I_h	Current passing a heating element	A
k	Coverage factor	
k_c	Correction factor	
L	Radiance	$W \cdot sr^{-1} \cdot m^{-2}$
m	Divisor with respect of the probability distribution	
m_s	Mass of a sample	Kg
M	Radiant exitance	$W \cdot m^{-2}$
N	Number of rays for Monte Carlo method	
Q	Radiant energy	J
r	Radius	m
$R(\lambda)$	Spectral responsivity of detectors	$A \cdot W^{-1}$ or $V \cdot W^{-1}$
R_h	Resistance of a heating element	Ω
S	Electrical signal	A or V
t	Time	s
T	Temperature	K
$u_i(x)$	Standard uncertainty	
$u_c(x)$	Combined standard uncertainty	
U	Expanded uncertainty	
V	Volume	m^3
w	Energy density	$J \cdot m^{-3}$
W	Radiant energy intensity	$J \cdot m^{-3}$
α	Absorptivity	
ε	Emissivity	
λ	Wavelength	μm
ρ	Reflectivity	
σ_0	Surface roughness	
σ_{SSE}	Size of source effect	
τ	Transmissivity	
τ_{air}	Propagation coefficient of atmosphere	
Φ	Radiant power/Radiant flux	W

Ω	Solid angle	sr

Symbol in Optics

B	Magnetic induction	$Wb \cdot m^{-2}$
C	Constant amplitude	
C'	Constant	
d_i	Distance between image plane and exit pupil plane	mm
d_o	Distance between object plane and entrance pupil plane	mm
D_{APD}	Dimension of active area of an APD	mm
D_{ep}	Diameter of entrance pupil	mm
D_{ExW}	Diameter of exit window	mm
D_{ExP}	Diameter of the exit pupil	mm
D_{meas}	Dimension of measurement area	mm
D	Electric displacement	$C \cdot m^{-2}$
E	Electric field intensity	$V \cdot m^{-1}$
f and f'	Front and rear focal lengths	mm
f_{cutoff}	Cut-off frequency of an optical system	Hz
F and F′	Front and rear focal points	
$\mathcal{G}_g(f_x, f_y)$	Normalised frequency spectra of ideal image	
$\mathcal{G}_i(f_x, f_y)$	Normalised frequency spectra of image	
h and h'	Object and image heights	mm
$h(x_i, y_i; x_o, y_o)$	Point spread function	
$h_I(x_i, y_i)$	Intensity point spread function	
$H_{MTF}(f_x, f_y)$	Modulation transfer function	
$\mathcal{H}_{OTF}(f_x, f_y)$	Normalised transfer function	
H	Magnetic field intensity	$A \cdot m^{-1}$
$I_g(x_i, y_i)$	Intensity function of ideal image	
$I_i(x_i, y_i)$	Intensity function of image	
J	Electric current density	$A \cdot m^{-2}$
J_1	The first-order Bessel function of the first kind	
k	Wavenumber	
l and l'	Principal points to object and image axial points	mm
M	Transverse magnification	
$MTF(f_x, f_y)$	Modulation transfer function	
n	Refractive index	
$\bar{n}$	Complex refractive index	
O and O′	Axial object and image points	
P and P′	Principal points	
$P(\xi, \eta)$	Pupil function	

r_{Airy}	Radius of the Airy pattern	µm
S	Poynting vector	$W \cdot m^{-2}$
u_M	The paraxial maximum marginal ray angle	rad
u_C	The paraxial maximum chief ray angle	rad
$U_i(x_i, y_i)$	Image function	
$U_g(x_i, y_i)$	Ideal image function predicted by geometrical optics	
$U_o(x_o, y_o)$	Object function	
z and z'	Focal point to object and image distances	mm
α_E	Fraction of enclosed radiant power percent	%
θ	Polar angle	°
κ	Extinction coefficient	
μ	Magnetic permeability	$H \cdot m^{-1}$
ρ_f	Charge density	$C \cdot m^{-3}$
σ_c	Specific conductivity	$S \cdot m^{-1}$
φ	Azimuth angle	°
$\phi(f_x, f_y)$	Phase transfer function	
ω	Angular frequency	$rad \cdot s^{-1}$

Subscript

a	Absorbed
$actl$	Actual value
b	Blackbody
bc	Black-cup method
BG	Background
cup	Internal area of the hemispherical cup
$dual$	Dual-cup method
eff	Effective quantity
ep	Entrance pupil
ExP	Exit pupil
ExW	Exit window
gap	The gap between the cup and sample
gc	Gold-cup method
ho	The hole opening on top of the hemispherical cup
i	Incident
max	Maximum value
$meas$	Measured
$mult-rfl$	Multi-reflection
n	Normal direction
$noml$	Nominal value
r	Reflected
rfl	Reflection

RES	Residual
s	Sample
sur	Surroundings
S	Area of a sphere
t	Transmitted
$wall$	Instrument wall
λ	Spectral
Ω	Directional
$\cap$	Hemispherical space
$\perp$	Perpendicular component
$\parallel$	Parallel component

Superscript

F	Fourier transform
$'$	Image space

Physical Constant

b	Wien's displacement constant	$2897.8\ \mu m \cdot K$
c_0	Speed of light in vacuum	$299792458\ m \cdot s^{-1}$
c_1	First radiation constant	$3.741771 \times 10^{-16}\ W \cdot m^2$
c_2	Second radiation constant	$1.438775 \times 10^{-2}\ m \cdot K$
h	Planck constant	$6.62607015 \times 10^{-34}\ J \cdot s$
k_B	Boltzmann constant	$1.3806488 \times 10^{-23}\ J \cdot K^{-1}$
σ	Stefan-Boltzmann constant	$5.670374419 \times 10^{-8}\ W \cdot m^{-2} \cdot K^{-4}$

Abbreviation

AFM	Atomic force microscopy
APD	Avalanche photodiode
DHR	Directional hemispherical reflectivity
DMD	Digital micromirror device
DTR	Distance to target ratio
EDX	Energy-dispersive X-ray spectroscopy
Ex-InGaAs	Extended indium gallium arsenide
FN	F-number
FOV	Field-of-view

FPA	Focal-plane-array
GEO	Geometric
HDR	Hemispherical directional reflectivity
IFOV	Instantaneous field-of-view
InAsSb	Indium arsenide antimonide
InGaAs	Indium gallium arsenide
ITS-90	International temperature scale of 1990
LWIR	Long-wavelength infrared
MCT	Mercury cadmium telluride (HgCdTe)
MEMS	Micro-electromechanical systems
MTF	Modulation transfer function
MWIR	Mid-wavelength infrared
NA	Numerical aperture
NIST	National Institute of Standards and Technology
OTF	Optical transfer function
PCB	Printed circuit board
PSF	Point spread function
PTB	Physikalisch-Technische Bundesanstalt
PTF	Phase transfer function
RMS	Root Mean Square
RMSE	Root Mean Square Error
SD	Standard deviation
SEM	Scanning electron microscopy
Si	Silicon
SI	The international system of units
SNR	Signal-to-noise ratio
SSE	Size of source effect
WD	Working distance

Contents

Chapter 1. Introduction

1.1 Radiation thermometry

All substances emit electromagnetic waves continuously due to the virtue of the molecular and atomic agitation, associating with their internal energy level. Radiation thermometry involves studying the characteristics of thermal radiation, which is the electromagnetic wave emitted by a medium solely because of its temperature [1]. In terms of the classical theory, radiation is defined as the flow of energy through free space or a material medium in the form of electromagnetic waves [2]. In terms of modern quantum theory, radiation is defined as the energy flow of photons through space [3]. Electromagnetic radiation exhibits a multitude of phenomena as it interacts with charged particles in atoms, molecules, and larger objects of matter. These phenomena are created and observed depending upon the wavelength (or frequency) [4]. The behaviours of electromagnetic waves are usually quite different due to the different wavelengths carrying different amounts of energy. Depending on their behaviour or occurrence, electromagnetic waves have been grouped into a number of different categories, as shown in Figure 1.1 [5]. The common designations are gamma rays, X rays, ultraviolet rays, visible rays, infrared rays, and microwaves. The behaviours of continuum radiation over the thermal radiation spectrum are the subjects studied by radiation thermometry.

Radiation thermometry is an interdisciplinary study field involved in many subjects such as physics, chemistry, materials science, medicine, and engineering science [6]. Thermal radiation emitted from an object represents its internal energy status with respect to its thermal condition. The interaction between the radiation and objects, such as reflection, absorption, and transmission, is affected by the physical status and chemical composition of objects [1]. From the point-of-view of applications, radiation thermometry focuses on non-contact temperature measurements and radiative property measurements. For example, radiation thermometers are applied to measure temperature quickly without touching the target surface to increase productivity and quality in industry [7]; thermal

cameras are used to provide straightforward thermal images in medical sciences [8]; remote sensing aims to trace the global environmental information [9]; unique coatings have been developed to change object surface radiative properties, such as decrease the thermal absorption of buildings in civil engineering [10], and increase the light absorption in solar energy engineering [11]. The increasing specifications in radiation thermometry also propel the development of semiconductor engineering, optical engineering, and electrical engineering [12]. Being linked to various research subjects, radiation thermometry will play an important role in the future.

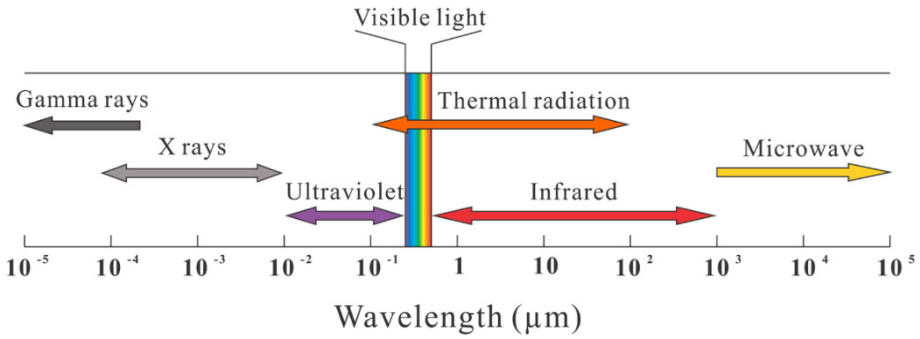

Figure 1.1 Electromagnetic wave spectrum.

1.1.1 Historical perspective

The beginning of studies on thermal radiation can be regarded as the discovery of infrared 'light'. In February 1800, when William Herschel was testing filters for observing sun spots, he found a red filter produced a lot of heat. Then, he used a prism to split the sunlight and tested the temperature of the visible spectrum. When he held a thermometer beyond the end of the red light, he was surprised to find that the thermometer showed a higher temperature than ambient air temperature. Further experimentation led Herschel to confirm the existence of infrared radiation beyond the visible spectrum [13].

Afterwards, research on thermal radiation turned in two directions: to explain the mechanism of thermal radiation theoretically and to measure the characteristics of thermal radiation experimentally.

For theoretical research, Kirchhoff (1860) first indicated that for an arbitrary body enclosed within an enclosure cavity in thermodynamic equilibrium, that body emits and

absorbs the same amount of thermal radiation from surroundings, otherwise the thermodynamic equilibrium cannot be valid [14]. That means, a blackbody is also an ideal body which radiates the greatest amount of energy compared to all other bodies at any given temperatures. Stefan (1879) and Boltzmann (1884) separately published the relationship between the total emissive power of a blackbody and temperature, known as Stefan–Boltzmann law [15, 16]. Wien (1894) proposed a spectral distribution of blackbody emissive power that is valid for short wavelengths, known as Wien's law [17]. Rayleigh (1900) and Jeans (1905) independently gave the distribution that is approximately valid in long wavelengths, known as Rayleigh–Jeans law [18, 19]. However, these two laws could not explain the behaviour of blackbody emissive power across both long and short wavelength regimes. When Wien's law is applied at long wavelengths, the blackbody radiation measured is not in accordance with the theoretical prediction. When Rayleigh–Jeans law is used in the short wavelength, blackbody radiation becomes infinite, known as the ultraviolet catastrophe. This problem was not resolved until Planck (1901) published his work on quantum statistics that assumed a molecule can emit photons only at distinct energy levels and found the spectral-blackbody emissive-power-distribution, now known as Planck's law [20].

At the same time, three tremendous achievements were realised by experimentalists. The first achievement was the introduction of a bolometer by the American astrophysicist Samuel Pierpont Langley in 1880. After that, experimentalists could use bolometers to measure thermal radiation accurately and confidently. The next achievement came with the experimental realisation of a usable blackbody source, which was performed by Wien and Lummer in 1895 [21]. The last and most important achievement was the most precious experimental findings published in that age. Based on detectors, sources, and their refinements and improvements later, large experimental works were undertaken and detailed experimental data of blackbody radiation were collected, which promoted theorists to propose and modify their distribution functions. For example, Rubens and Kurlbaum's work published in 1900 directly supported and confirmed the validity of Planck's law among the other four theories including Wien's displacement law [22].

At the end of this period, both theories and experiments achieved a good agreement to explain the spectral-blackbody emissive-power-distribution. Thereafter, researchers set their sights on applying the knowledge on research fields associated with radiation thermometry.

1.1.2 Application

Radiation thermometry is applied in non-contact temperature measurements by transferring radiant power emitted from a measurand to electrical signals using radiation thermometers. Measurements can be undertaken without physical contact with the surface of a measurand due to the inherent advantage of photoelectric effect. Therefore, this method is more suitable for measuring an object whose surface is fragile or sensitive to contaminations, is extremely hot, or is located at a far distance. In addition, radiation thermometers have a fast-response time, have minimum thermal disruption, and are immune to electrical fields [12].

In the metallurgical industry, manufacturers need to understand the temperature of products and to control the heating or cooling rate precisely during different processes. A deviation between the required and actual temperature of metal products will cause unspecified grain growth, leading to the poor quality [23, 24]. Meanwhile, the internal stress will not be fully released if products are heated or cooled too fast. On the contrary, the productivity will be reduced if the heating or cooling rate is too slow [25, 26]. Radiation thermometers are more capable than contact thermometers in metallurgical industry to process these challenges.

In additive manufacturing, metal powder is heated and melted by the laser or electron beam layer-by-layer to form the designed parts. It is crucial to measure the melting temperature at the beam focus position and feed the result back to the machine to control the output power. Otherwise internal defects, such as cracks or micro-cavities, are produced which will cause printing failure [27, 28]. At this moment, only radiation thermometry can meet the specifications of a high temperature range for contamination-free and fast-response measurements in additive manufacturing [29].

In remote sensing, researchers are interested in the acquisition of information of the Earth, including land, ocean, and plants [30, 31, 32]. This information is usually collected from the sky by satellite- or aeroplane-based instruments due to the large scale of the measurement area and limits of inaccessible places, which requires non-contact measurement methods. If the information of interest involves target temperature distribution, such as the ocean current, glacier movement, or plant growth, multi- and hyper-spectrometers are more popular in obtaining detailed thermal maps [9, 33].

In medical science, research indicates that abnormal skin temperature is mostly linked to unusual blood speed and pressure caused by physical illness [8]. Thermal imaging cameras have been used in medical thermography for more than five decades for taking passive and non-invasive thermal images [34]. By studying the skin thermal images of patients under a controlled environment, researchers can diagnose diseases such as the sports injury [35], vascular disorder [36], breast cancer [37, 38], and diabetic neuropathy [39]. With the development of focal-plane-array (FPA) detectors, data acquisition, and image processing technology, it is possible to offer real-time thermal imaging analysis for image-guided surgery [40].

Measurements in radiation thermometry involve the research in blackbody, radiation thermometers, and emissivity. Blackbody performs as a standard source for emitting radiant flux. Radiation thermometers capture radiant flux emitted from a target and produce corresponding electronic signals. Emissivity indicates the radiative properties of a target, which can be used to compute the true temperature.

1.2 Research on blackbody

A blackbody is an ideal physical body that absorbs all incident electromagnetic radiation for all wavelengths and angles of incidence. Furthermore, a blackbody is a perfect emitter that emits the maximum radiant energy at any given temperature, wavelength, and direction. The radiant energy of a blackbody can be quantified by physical laws [1]. Particularly, the emissive power of a blackbody over the whole spectrum is a function of its temperature in vacuum. Meanwhile, a blackbody is a perfect diffuser whose radiant intensity obeys Lambert's cosine law [41, 42]. Because of these unique properties, a blackbody is used as an ideal standard radiation source for calibrating other instruments. Although a perfect blackbody does not exist, several approaches can be used to develop an approximate blackbody whose absorptivity is close to 1; for example, a cavity with a small hole opening can perform as an approximate blackbody in thermal equilibrium [1]. In general, a practical blackbody can be classified as a fixed-point blackbody or a variable temperature blackbody with respect to the heating method [5].

A fixed-point blackbody achieves stabilisation of radiance temperatures by heating with fixed-point materials at their melting or freezing phase [43]. Figure 1.2 shows a typical

design of a fixed-point blackbody cell. The cavity should be designed with an appropriate length and diameter to offer the high effective emissivity as well as to achieve the uniform thermal distribution along the cavity. The cavity is surrounded by fixed-point materials contained by a crucible. The fixed-point materials are usually made from pure metals, metal-carbon eutectics, and metal-carbide-carbon peritectics [44, 43]. When a fixed-point blackbody cell is used as a radiance source, the whole cell is heated by a furnace. As the furnace reaches the specified temperature, the temperature of fixed-point materials is stabilised at their melting, freezing, eutectic, or peritectic temperature, and, thereafter, the inner cavity is also stabilised at that temperature.

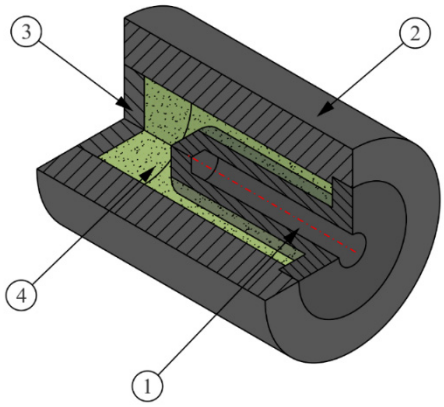

Figure 1.2 Schematic diagram of a fixed-point blackbody cell: cavity (1); crucible (2); fixed-point material (3); end seal (4).

The thermodynamic temperature of a fixed-point blackbody cell is determined by physical properties of fixed-point materials which can be traced by ITS-90 standard [43]. This advantage leads the fixed-point blackbody to be selected as the reference standard radiation source for radiation thermometry calibrations. However, a fixed-point blackbody cannot emit radiant energy within a continuous temperature range. Hence, it is necessary to develop another type of blackbody to solve the inconvenience.

A variable temperature blackbody is used to emit radiation in a continuous temperature range. Figure 1.3 shows the typical design of a variable temperature blackbody. This type of blackbody is composed of a cavity and external housing. The cavity is exposed to heating elements of the furnace directly, instead of heating by fixed-point materials. The radiance temperature is monitored by one or several thermocouples distributed along the cavity wall. By this method, the cavity can be heated and stabilised at given radiance temperature continuously.

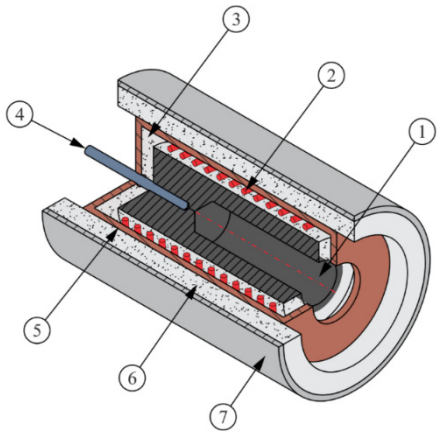

Figure 1.3 Schematic diagram of a variable temperature blackbody: cavity (1); heating elements (2); thermal isolation (3); thermocouple (4); inner housing (5); thermal isolation (6); external housing (7).

In practice, all types of blackbodies require precise calibrations before performing as standard radiance sources. The uncertainties derive from various sources such as the impure fixed-point materials, gradient thermal distribution along the cavity, drift of thermocouples, and fluctuation of heating elements [45]. After the calibration, the combined standard uncertainty of a blackbody should be stated to offer traceable results on further applications [46].

1.3 Research on radiation thermometers

A radiation thermometer transfers the radiant flux emitted from an object to electronic signals and thereafter realises the non-contact temperature measurements [47]. By calibrating against a blackbody source carefully, a radiation thermometer can be used to undertake temperature measurements or emissivity measurements. Radiation thermometers can be developed with various forms, including spot infrared pyrometers and thermal imaging cameras. Figure 1.4 shows the schematic diagram of a thermal imaging camera. The performance of a radiation thermometer is determined by three aspects: infrared detectors, optical systems, and prior calibrations.

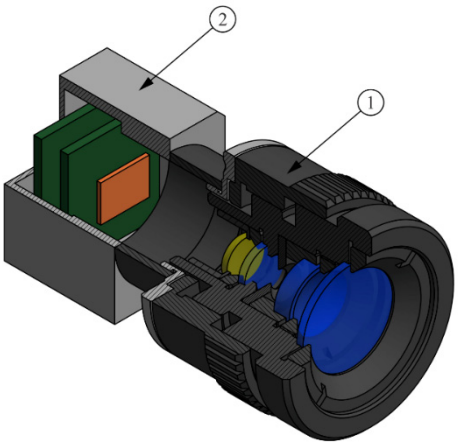

Figure 1.4 Schematic diagram of a thermal imaging camera: lens (1); infrared detector (2).

1.3.1 Infrared detector

Infrared detectors are critical components in developing radiation thermometers that determine the measurement temperature range, minimum resolvable temperature difference, and potential distinguishable thermal features. After several decades of development, numerous infrared detectors have been developed, which can be divided as two broad categories: thermal detectors and photon detectors [48].

A thermal detector changes its temperature-dependent properties after absorbing incident radiation and outputs the property change as electrical signals [48]. Thermal detectors can be of various types, including thermopiles, pyroelectric detectors, and bolometers. A thermopile is composed of thermocouples that generates voltage signals due to the thermoelectric effect. The generated potential difference on the junction of two different metals is proportional to the heating temperature [49]. A pyroelectric detector uses a pyroelectric material connected to two electrodes mounted perpendicular to the direction of spontaneous polarisation. The temperature change of the detector, caused by the absorption of incident thermal radiation, leads to the change in surface charge [50]. A bolometer measures its electrical resistance variation corresponding to the temperature change when it is heated by receiving the thermal radiation [51]. A typical thermal detector can respond to a broad waveband. To extend the application scope, the spectral responsivity of a thermal detector can be modulated by coupling optical filters in front of the detector [52].

A photon detector employs materials to absorb incident photons and produces electronic energy distribution changes that are proportional to the count of absorbed photons [53]. Photon detectors can work either at a photovoltaic or photoconductive mode, representing voltage or resistance changes, respectively. Photon detectors have faster response speed and higher sensitivity compared to thermal detectors. However, photon detectors also show a selective wavelength dependence of response. Figure 1.5 shows the spectral detectivity of different commercial infrared detectors. Since the first extrinsic photoconductive detector was developed in the early 1950s, the technique for controlled impurity introduction has led to the emergence of numerous semiconductor photon detectors [54, 55]. The IV, III-V, and II-VI semiconductors have been widely used in developing sensors due to their unique performances. Typical Silicon (Si) detectors exhibit a spectral response from 0.4 to 1.1 μm [56]. Indium gallium arsenide (InGaAs) detectors provide a high response between wavelengths of 0.9 to 1.7 μm [57]. Extended indium gallium arsenide (Ex-InGaAs) detectors are available to cover the wavelength between 0.9 to 2.6 μm [58]. Mercury cadmium telluride (HgCdTe or MCT) detectors offer a wide spectral response range from 1 to 25 μm by varying the relative component, which offers flexibility in application in mid-wavelength infrared (MWIR) and long-wavelength infrared (LWIR) cameras [59, 60].

Infrared detectors can be fabricated as single-element detectors, linear-array detectors, and focal-plane-array detectors with respect to the scale of the integrated pixels [48]. Compared with single-element and linear-array detectors, FPA detectors can produce thermal images directly. This feature has made FPA detectors an important research subject since the last five decades. During this period, many FPA detectors have been developed with a large frame and small pitch. Caulfield *et al.* reported a 2040 × 1156 indium arsenide antimonide (InAsSb) detector with a 5-μm pixel size applied in an MWIR camera [61]. Armstrong *et al.* demonstrated a 1024 × 768 HgCdTe detector with a 5-μm pitch in an LWIR camera using high-density vertically integrated photodiode architecture [62].

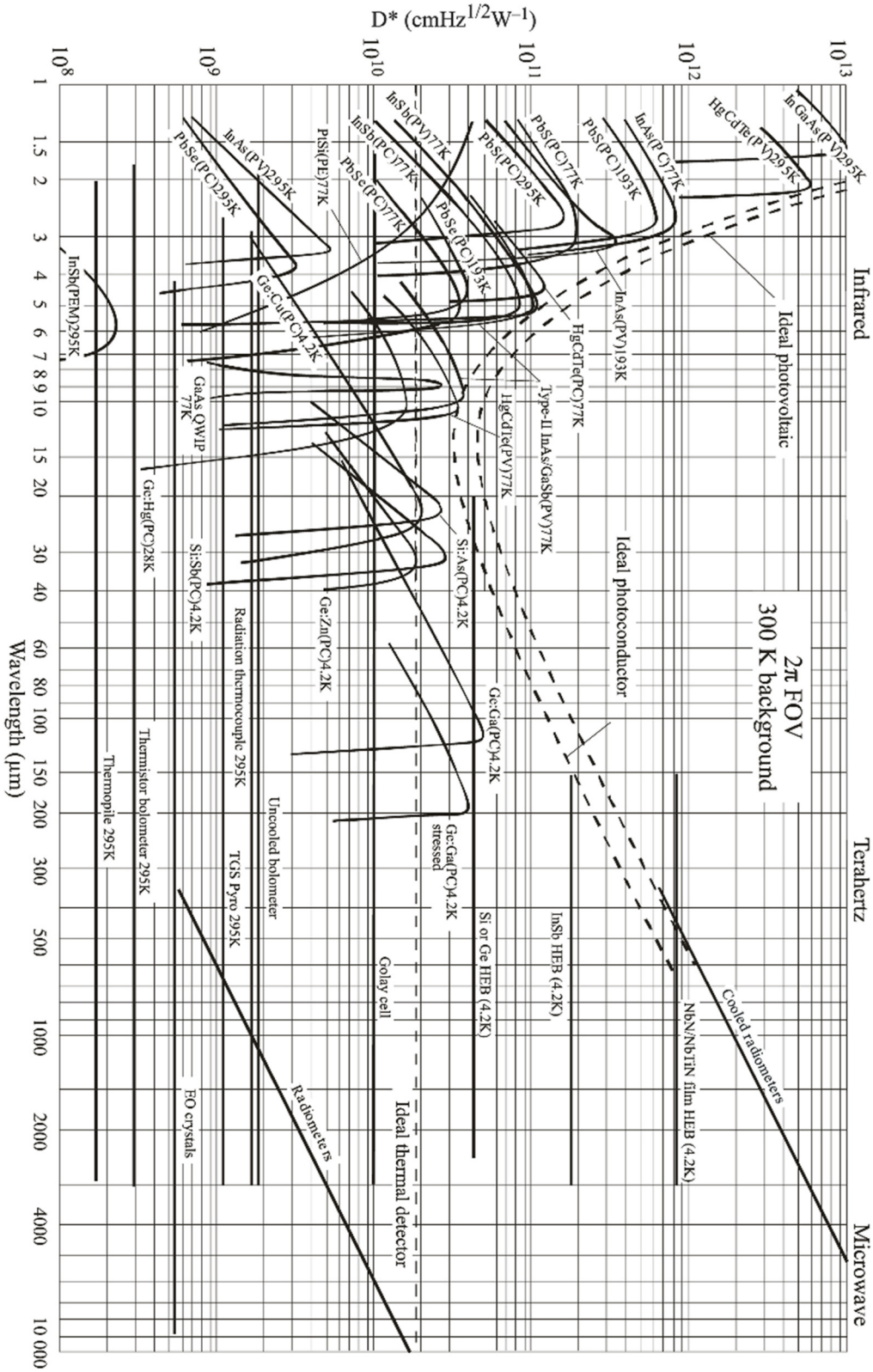

Figure 1.5 Spectral detectivity of different commercial detectors [48].

1.3.2 Optical systems

Optical systems are developed to concentrate the rays emitted from a target on a detector sensor. In practice, a radiation thermometer should be developed to operate in actual working environments that can be various case by case. Thereby, optical systems should be designed with appropriate structures to meet the specific requirements. In general, optical systems can be classified into three categories: single-point systems, scanning systems, and staring systems [2].

A single-point system is developed to measure a small axial area of a target using a single-element detector, which is widely used in industrial [47]. A typical single-point system is shown in Figure 1.6. The thermal radiation emitted from a target is collected by a lens and focused on the detector. To identify the measurement area, the visible lights leaving the same area are also collected by the same lens, split by a beam splitter and focused by an eyepiece. Such types of systems only use the paraxial area to form an image. In this case, the system can be developed with a simple structure, usually by using a singlet or a doublet. However, this system can only measure one location per time. If the temperature distribution of a target is required, users need to repeat multiple measurements across the target manually, which is time consuming and usually introduces unwanted uncertainties.

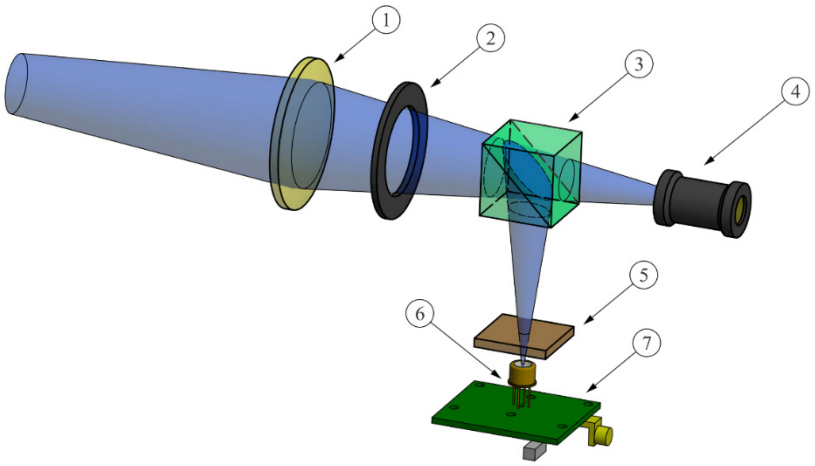

Figure 1.6 Schematic diagram of a single-point radiation thermometer: lens (1); aperture (2); beam splitter (3); eye piece (4); filter (5); detector (6); signal processor (7).

A scanning system integrates a frame of a thermal image line-by-line using a linear-array detector or point-by-point using a single-element detector. Compared with the single-point system, a scanning system can acquire the thermal information of a scene quickly. Figure 1.7 shows the schematic diagram of a typical scanning system equipped with a linear-array detector [2]. A rotating flat mirror is used as a deflecting component to change the direction of the field-of-view (FOV). Another type of scanning systems is designed to cover the whole azimuth range by rotating a linear-array detector with the use of a rotation stage, as shown in Figure 1.8. Using a pair of deflecting mirrors, scanning systems can integrate thermal images with a single-element detector [2]. Scanning systems can be designed with a wide FOV whilst maintaining a large aperture [30, 63].

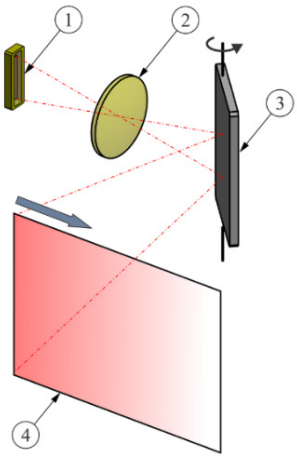

Figure 1.7 Schematic diagram of a scanning system equipped with a linear-array detector: linear detector (1); lens (2); scanning mirror (3); object plane (4).

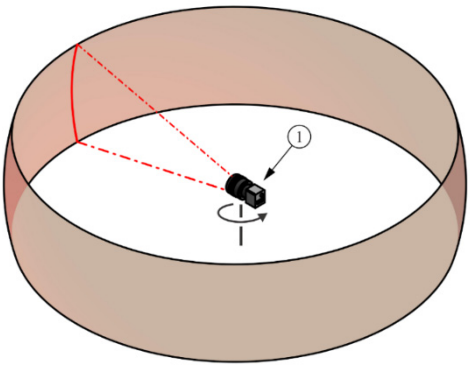

Figure 1.8 Schematic diagram of a scanning system covering the whole azimuth range: linear detector (1).

A staring system uses an FPA detector, which does not require a deflecting component or rotation stage, to produce thermal images. A staring system is mainly composed of an infrared lens and an FPA detector, as shown in Figure 1.9. In practice, the system is usually designed as two separate parts: thermal cameras and lenses. This offers the flexibility to adapt various lenses to a thermal camera to change the FOV for measuring various object scenes. Modulation transfer function (MTF) is a universal standard to evaluate the performance of lenses, which is the magnitude response to sinusoids of different spatial frequencies [2].

A staring system can be used to produce emissivity maps directly. However, challenges are raised to the design of a quantitative measurement instrument due to the non-uniformity of spectral responsivity and cross-talk amongst large numbers of pixels [64, 65]. In particular, the existence of size of source effect (SSE) changes the instantaneous field-of-view (IFOV). This leads to an unpredictable and imprecise measurement across the target, which will be analysed in Chapter 2.

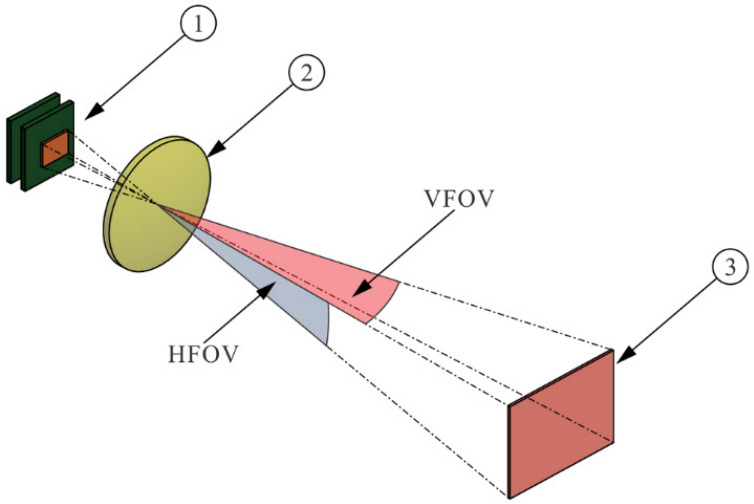

Figure 1.9 Schematic diagram of a typical staring system: FPA detector (1); lens (2); object plane (3).

1.3.3 Calibration

Before using a radiation thermometer for measurements, it is essential to undertake non-uniformity correction and radiometric calibration [45]. Non-uniformity correction is used to resolve the problem caused by different spectral responsivity of each pixel of linear-

array detectors and FPA detectors. Radiometric calibration is undertaken to correct the radiation thermometer electrical output and the blackbody radiance temperature at 1, 3 or more temperature points.

Linear-array and FPA detectors have different gain and offset among detector elements in the array, causing detector-to-detector nonuniform responsivity. This response non-uniformity leads to a fixed pattern noise for each individual detector, which is changeable with time, even when acquiring an image of the same object scene [66]. This pattern noise is due to many factors, such as the tolerance of fabrication processes, detector operating temperature, electronic readout noises, and radiance from the scene [67]. Several methods have been developed for non-uniformity correction, including calibration-based methods [68] and scene-based methods [69]. Calibration-based methods use a shutter to block the detector and offer a uniform background image as the reference, which are needed to stop image acquisition periodically [70]. Scene-based methods use adaptively updated correction coefficients based on the scene to undertake the correction in real-time, which does not require a shutter [71, 72].

Radiation thermometers are required to undertake radiometric calibrations to measure the temperature or emissivity. When measuring a thermal target, the output signal depends on the responsivity of the detector, the transmissivity of the lens, and the absorptivity along the optical path [1]. In addition, the output grey level of a detector may drift as ambient temperature changes [53]. These factors cause a difficulty in interpreting the thermal information and acquiring signals by theoretical calculations. A practical method is to calibrate the radiation thermometer with an approximate blackbody source at the interested temperatures and find out the relation between the output grey value and the blackbody radiance temperature [47]. During the measurement, a radiation thermometer receives radiant flux from the target and its surroundings because of reflection and scattering [73]. This radiation enhancement causes an uncertainty in the measurements, which should also be compensated [74].

Once the calibration of a radiation thermometer is performed, the thermometer is ready for acquiring the relative thermal information of a target. If the emissivity of that measurand is known, its true temperature can be obtained.

1.4 Research on emissivity

Emissivity is defined as the ratio of the radiant energy emitted from a body to that emitted from a blackbody at the same temperature and wavelength and under the same viewing conditions. In practice, emissivity is also affected by surface conditions, including surface roughness and chemical composition. An ideal blackbody always emits the maximum radiant energy at any given temperature and wavelength. Hence, the emissivity of a real object always ranges between 0 and 1.

1.4.1 Application

Emissivity represents the radiative properties of materials. It is an important quantity in radiation thermometry, particularly in non-contact temperature measurements and materials science.

For non-contact temperature measurements, emissivity should be prior known before computing the true temperature of an object from the relative thermal information measured by a radiation thermometer [75, 29, 76]. The accuracy for non-contact temperature measurements is determined by both the performance of a radiation thermometer and the reliability of the emissivity selected as a reference [19, 77]. The uncertainty in emissivity measurements can dominate the overall temperature measurement accuracy, for example, a relatively small emissivity variation of ± 0.01 can cause a temperature uncertainty of ± 1.12 °C at 1000 °C, using a 1 μm wavelength thermometer and ± 7.56 °C using a long wavelength thermometer, measuring at 8-14 μm. The emissivity value referred in each application should be measured accurately with stating the measurement uncertainty. Otherwise the emissivity uncertainty can lead to unacceptable and unknown overall temperature measurement errors. Often, these errors will cause quality control problems and defects within the manufacturing process [29].

Besides temperature measurements, emissivity is a fundamental measure that quantifies the heat transfer ability of materials [1]. It indicates the energy emitting and absorbing ability at the given temperature and wavelength. In materials science, researchers focus on fabricating materials with extremely low and high emissivity to meet different specifications. Low emissivity materials and coatings are widely used in military and civil applications, such as external coatings of attack aircrafts that act as infrared

camouflage [78, 79] and coatings applied to architectural glass to reduce the absorption of solar radiation [80, 10]. In contrast, high emissivity materials are applied in metrology and energy collecting systems [81, 82]. Combined with nanotechnology, researchers aim to manipulate the radiative properties of materials against wavelengths and working temperatures, to meet specific demands from various applications [83, 11]. Accurate emissivity measurements are required to characterise the radiative properties in these research fields.

Emissivity has been actively studied for several decades and a lot of research has been published. On the one hand, many hypotheses and theories have been developed to predict emissivity and characterise emission properties. On the other hand, various instruments have been developed to obtain emissivity data experimentally, which is due to the difficulty produced by numerous variables in predicting radiative properties.

1.4.2 Theoretical predictions of emissivity

The radiative properties of materials can be explained by quantum physics and classic electromagnetic wave theory [1, 5]. For optically smooth surfaces of metals, spectral reflectivity can be determined by Fresnel's equation if the refractive index and the extinction coefficient are known. These optical properties can be obtained by experimental methods or can be estimated by Drude free electron theory [84] and Hangen-Rubens equation [85]. Thus, the spectral emissivity is possible to be predicted according to Kirchhoff's law in thermal equilibrium [14]. Sievers gave extended expressions and compared the total normal and hemispherical emissivity between the predicted and experimental results for metals [86]. Kobatake *et al.* measured the spectral normal emissivity of liquid iron and nickel and compared the results with the values predicted by Drude [87].

In practice, the actual surface is not always optically smooth and may have a certain grade of surface roughness (σ_0). Hence, the emitted radiation is diffracted or reflected by the surface structure, leading to changes in emission properties. Wen *et al.* concluded previous research on the relationship between emissivity and surface roughness [88]. For a specified wavelength (λ), if the surface roughness is smaller than the wavelength ($0 < \sigma_0/\lambda < 0.2$), the reflection of incident radiation is assumed to be specular and the diffraction theory is usually applied to predict the effects of surface roughness on the

radiative properties of materials [89]. When the surface roughness is in the equivalent region compared to the wavelength ($0.2 < \sigma_0/\lambda < 1$), the spectral emissivity is analysed by models based on the bidirectional reflectance distribution function [90, 91]. If the surface roughness is larger than the wavelength ($\sigma_0/\lambda > 1$), the method of geometrical optics can be applied to predict the directional radiative behaviour whilst the effect of diffraction can be ignored [92].

A real surface may also be covered by a layer of oxide film which has a different refractive index and absorptive index to the substrate. To predict the emissivity of oxidised materials, the oxide film is usually assumed as an even, transparent, or semi-transparent layer. Thus, the emission properties can be modelled by applying the electromagnetic wave theory on processing the plane wave which is incident on a multi-layer media [4]. Iuchi *et al.* measured the emissivity of cold-rolled steels during the oxidation period and presented models to predict emissivity behaviours [93]. Wang *et al*. calculated the emission properties of multi-layered silicon wafer under nonuniform temperature distributions [94].

Although much work has been carried out to improve the theory for radiative properties, the result is not satisfying for applying these theories for a real surface accurately. This is due to the difficulty in measuring optical constants, specifying surface conditions, and controlling surface preparations. Hence, accurate emissivity references are usually obtained by experimental methods.

1.4.3 Experimental measurements of emissivity

Experimental measurements of emissivity are undertaken for offering references for application in scientific research and industrial fields. Emissivity measurements can be classified as direct and indirect methods [5]. The direct method measures the radiant flux from a measurand to obtain emissivity, whilst the indirect method measures reflectivity and transmissivity and then computes the emissivity by Kirchhoff's law [95, 96]. The details of each measurement method will be discussed in Chapter 3.

To provide reliable and traceable emissivity measurements, considerable efforts have been spent on developing high-accuracy facilities. NPL, NIST, and PTB have developed their new-generation facilities to study spectral emissivity of materials with respect of a

broad temperature range and a wide emission angle since 2004 [97, 98, 99]. The uncertainty estimation of each facility has been analysed thoroughly. The uncertainty budget is composed of the components of all applied devices, calibrations, and operations. Saunders *et al.* gave a detailed uncertainty table for calibrating radiation thermometers, which is also valid for emissivity measurements [46]. Pérez-Sáez *et al.* also gave an uncertainty analysis of direct emissivity measurement methods with the consideration of background radiation interferences [100].

Another important research topic is to study the mechanism of spectral emissivity corresponding to surface roughness. Wen *et al.* measured the spectral normal emissivity of aluminium alloys with different grades of surface roughness, and characterised the sample topography by using atomic force microscopy (AFM) [101, 102, 88]. Wang *et al.* measured the normal emissivity of polished graphite and observed the surface topography with the use of scanning electron microscopy (SEM) [103]. Although advanced microscopes have been used for emissivity measurements, results do not always agree with each other unless researchers state the detailed surface conditions. This is mainly because the characteristics of roughness may be various from surface to surface, depending on the material, manufacturing process, sample preparation, etc.

The impacts on emissivity variations due to surface oxidation is another important research direction. Surface oxidation can affect radiative properties of solid materials, especially for metals and semiconductors. Oxide films are formed by chemical reactions and may generate thin coatings with different refractive indices and absorptive indices. These films may act as a Fabry-Pérot interferometer or perform as an opaque layer at other wavelength ranges, leading to emissivity variations. Huntz *et al.* measured the emissivity of oxidised stainless steels from 850 to 950 °C and analysed the surface topography changes after experiments [104]. Ham *et al.* studied the relation between the oxidation and emissivity for transformation-induced plasticity steels during the annealing process at a waveband of 8 to 12 μm [105].

1.5 Motivation

This work focuses on the development of three instruments to undertake studies on emissivity of opaque materials. These studies aim to solve several problems that have

existed in emissivity measurements for decades, including the uncertainty analysis for direct and indirect measurement methods, impacts on emissivity variations due to the surface condition change, and methods for mapping emissivity of a target with complex surface conditions. The instruments developed in this work can also provide accurate emissivity measurements in materials science and offer references for end users in radiation thermometry.

Although many instruments have been developed for emissivity measurements, the uncertainty budget of these instruments is usually insufficient, leading to unreliable measurements [106, 107, 108]. Furthermore, emissivity can be measured by either direct or indirect methods. Each method has its own inherent advantages and disadvantages, which therefore dictates the most suitable emissivity measurement range [109, 110]. However, the boundary of the measurement range between the direct and indirect methods has not been systematically studied. The lack of a clear understanding of the most suitable measurement range of each method prevents undertaking measurements with lower uncertainties.

Emissivity of opaque materials depends on the surface conditions, particularly the surface roughness and chemical composition. Great efforts have been spent on studying the relationship between the emissivity and surface roughness. However, surface conditions are not always constant during measurements. When a sample is heated in air, oxidation changes the surface chemical composition as well as surface roughness. For some metal alloys heated to a high temperature, chemical reactions are inevitable even under a vacuum environment, which causes the emergence of new chemical compounds between alloy elements and new surface features. The variation in surface conditions leads to changes in emissivity properties, which are determined by different factors such as temperature, heating and cooling rate, and environmental atmosphere. The emissivity properties should be analysed by considering the changes of surface conditions, which have not been fully studied.

In practice, the specimen surface condition is usually complex when it is collected from the actual working environment due to surface oxidations, chemical reactions, and contaminations. Single-point radiation thermometers are not suitable to obtain the emissivity distribution across the specimen. Thermal cameras can be used to investigate the emissivity map of a specimen. Due to the non-uniformity and cross-talk between

pixels, thermal cameras cannot offer a quantitative measurement, unless it is calibrated and corrected carefully, which is time consuming and expensive. A single-pixel scanning system is a potential low-cost solution to produce accurate emissivity maps across the object of interest quantitatively. Due to the usage of a single-element detector, this system does not have the problem of the non-uniformity and cross-talk. However, the development of this system in emissivity measurements has not been fully completed and reported.

1.6 Thesis overview

This thesis is organised as follows:

Chapter 2 briefly introduces the background theories in radiation thermometry and optics, including blackbody radiation, radiative properties of real surfaces, electromagnetic theory, image quality analysis, and method for developing a high-performance radiation thermometer.

Chapter 3 summarises the current emissivity measurement methods, including direct and indirect measurement methods.

Chapter 4 gives details for developing an emissivity measurement instrument from 200 to 450 °C, with a waveband of 2.1 to 2.5 μm. The instrument can offer both direct and indirect emissivity measurement methods. The uncertainty was discussed thoroughly to determine the most suitable measurement range of each method.

Chapter 5 provides the development of an emissivity measurement instrument from 700 to 1150 °C, with a waveband of 0.85 to 1.05 μm. The emissivity of stainless steel 304 was measured under several controlled oxidation procedures. The surface oxide conditions of samples were studied by using scanning electron microscopy and energy-dispersive X-ray spectroscopy to investigate the relationship between emissivity variations and surface condition changes.

Chapter 6 introduces the design and development of an emissivity mapping instrument based on a MEMS mirror device. The instrument can offer fast scanning of the sample surface and produce 160 × 120 pixel emissivity maps. The information of each pixel

represents a measurement undertaken by a fully calibrated single-point radiation thermometer.

Chapter 7 summarises the work of this thesis and provides the outlook of future work on emissivity measurements and applications.

Chapter 8 gives the methodology for undertaking the uncertainty analysis in direct emissivity measurement methods.

References

[1] J. R. Howell, and R. Siegel, *Thermal radiation heat transfer*, 3rd ed., New York: Hemisphere Publishing Co., 1992.

[2] M. Bass *et al.*, *Handbook of Optics, Third Edition Volume I: Geometrical and Physical Optics, Polarized Light, Components and Instruments(set)*: McGraw-Hill, Inc., 2010.

[3] D. F. Walls, and G. J. Milburn, *Quantum optics*: Springer Science & Business Media, 2007.

[4] M. Born, E. Wolf, and A. B. Bhatia, *Principles of Optics: Electromagnetic Theory of Propagation, Interference and Diffraction of Light*: Cambridge University Press, 2000.

[5] M. F. Modest, *Radiative heat transfer*: Academic press, 2013.

[6] R. Gade, and T. B. Moeslund, "Thermal cameras and applications: a survey," *MACH VISION APPL,* vol. 25, no. 1, pp. 245-262, 2013.

[7] M. Vollmer, and K.-P. Möllmann, *Infrared thermal imaging: fundamentals, research and applications*: John Wiley & Sons, 2017.

[8] B. B. Lahiri *et al.*, "Medical applications of infrared thermography: A review," *Infrared Phys. Technol.,* vol. 55, no. 4, pp. 221-235, 2012.

[9] C. J. Tomlinson *et al.*, "Remote sensing land surface temperature for meteorology and climatology: a review," *Meteorol. Appl.,* vol. 18, no. 3, pp. 296-306, 2011.

[10] B. P. Jelle, S. E. Kalnæs, and T. Gao, "Low-emissivity materials for building applications: A state-of-the-art review and future research perspectives," *Energy Build.,* vol. 96, pp. 329-356, 2015.

[11] X. Wang *et al.*, "High-temperature tolerance in WTi-Al2O3 cermet-based solar selective absorbing coatings with low thermal emissivity," *Nano Energy,* vol. 37, pp. 232-241, 2017.

[12] P. Childs, J. Greenwood, and C. Long, "Review of temperature measurement," *Rev. Sci. Instrum.,* vol. 71, no. 8, pp. 2959-2978, 2000.

[13] M. Rowan-Robinson, *Night vision: Exploring the infrared universe*: Cambridge University Press, 2013.

[14] G. Kirchhoff, "Ueber das Verhältniss zwischen dem Emissionsvermögen und dem Absorptionsvermögen der Körper für Wärme und Licht," *Ann. Phys.,* vol. 185, no. 2, pp. 275-301, 1860.

[15] J. Stefan, and K.-K. H. und Staatsdruckerie, *Über die Beziehung zwischen der Wärmestrahlung und der Temperatur*: Aus der kk Hof-und Staatsdruckerei, 1879.

[16] L. Boltzmann, "Ableitung des Stefan'schen Gesetzes, betreffend die Abhängigkeit der Wärmestrahlung von der Temperatur aus der electromagnetischen Lichttheorie," *Ann. Phys.,* vol. 258, no. 6, pp. 291-294, 1884.

[17] W. Wien, "Temperatur und entropie der strahlung," *Ann. Phys.,* vol. 288, no. 5, pp. 132-165, 1894.

[18] J. H. Jeans, "On the partition of energy between matter and ether," *The London, Edinburgh, and Dublin Philosophical Magazine and Journal of Science,* vol. 10, no. 55, pp. 91-98, 1905.

[19] R. P. Madding, "Emissivity measurement and temperature correction accuracy considerations," in *Thermosense XXI, International Society for Optics and Photonics (SPIE)*, *Orlando, FL*, 1999, pp. 393-401.

[20] M. Planck, "On the Law of the Energy Distribution in the Normal Spectrum," *Ann. Phys.,* vol. 4, no. 553, pp. 1-11, 1901.

[21] W. Wien, and O. Lummer, "Methode zur Prüfung des Strahlungsgesetzes absolut schwarzer Körper," *Ann. Phys.,* vol. 292, no. 11, pp. 451-456, 1895.

[22] H. Rubens, and F. Kurlbaum, *Über die Emission langwelliger Wärmestrahlen durch den schwarzen Körper bei verschiedenen Temperaturen*, 1900.

[23] F. Gil, and J. Planell, "Behaviour of normal grain growth kinetics in single phase titanium and titanium alloys," *Mater. Sci. Eng., A,* vol. 283, no. 1-2, pp. 17-24, 2000.

[24] M. Shirdel, H. Mirzadeh, and M. Parsa, "Abnormal grain growth in AISI 304L stainless steel," *Mater. Charact.,* vol. 97, pp. 11-17, 2014.

[25] D. H. Shin *et al.*, "Microstructural changes in equal channel angular pressed low carbon steel by static annealing," *Acta Mater.,* vol. 48, no. 12, pp. 3245-3252, 2000.

[26] M. Smith *et al.*, "Accurate prediction of residual stress in stainless steel welds," *Comput. Mater. Sci,* vol. 54, pp. 312-328, 2012.

[27] W. E. Frazier, "Metal Additive Manufacturing: A Review," *J. Mater. Eng. Perform.,* vol. 23, no. 6, pp. 1917-1928, 2014.

[28] M. Seifi *et al.*, "Progress towards metal additive manufacturing standardization to support qualification and certification," *JOM,* vol. 69, no. 3, pp. 439-455, 2017.

[29] N. Boone *et al.*, "Thermal near infrared monitoring system for electron beam melting with emissivity tracking," *Addit. Manuf.,* vol. 22, pp. 601-605, 2018.

[30] J. B. Campbell, and R. H. Wynne, *Introduction to remote sensing*: Guilford Press, 2011.

[31] V. Klemas, "Remote sensing of coastal and ocean currents: An overview," *JCR,* vol. 28, no. 3, pp. 576-586, 2012.

[32] M. Belgiu, and L. Drăguţ, "Random forest in remote sensing: A review of applications and future directions," *ISPRS J. Photogramm. Remote Sens.,* vol. 114, pp. 24-31, 2016.

[33] F. D. Van der Meer *et al.*, "Multi-and hyperspectral geologic remote sensing: A review," *Int. J. Appl. Earth Obs. Geoinf.,* vol. 14, no. 1, pp. 112-128, 2012.

[34] R. B. Barnes, "Thermography of the Human Body: Infrared-radiant energy provides new concepts and instrumentation for medical diagnosis," *Science,* vol. 140, no. 3569, pp. 870-877, 1963.

[35] C. Hildebrandt *et al.*, "The application of medical infrared thermography in sports medicine," *An international perspective on topics in sports medicine and sports injury*: IntechOpen, 2012.

[36] S. Bagavathiappan *et al.*, "Infrared thermal imaging for detection of peripheral vascular disorders," *J Med Phys,* vol. 34, no. 1, pp. 43, 2009.

[37] D. J. Hawrysz, and E. M. Sevick-Muraca, "Developments toward diagnostic breast cancer imaging using near-infrared optical measurements and fluorescent contrast agents1," *Neoplasia,* vol. 2, no. 5, pp. 388-417, 2000.

[38] S. Mambou *et al.*, "Breast cancer detection using infrared thermal imaging and a deep learning model," *Sensors,* vol. 18, no. 9, pp. 2799, 2018.

[39] L. F. Balbinot *et al.*, "Plantar thermography is useful in the early diagnosis of diabetic neuropathy," *Clinics,* vol. 67, no. 12, pp. 1419-1425, 2012.

[40] S. Gioux, H. S. Choi, and J. V. Frangioni, "Image-guided surgery using invisible near-infrared light: fundamentals of clinical translation," *Mol. Imag.,* vol. 9, no. 5, pp. 7290.2010. 00034, 2010.

[41] J. H. Lambert, "Observationes variae in mathesin puram," *Acta Helvetica,* vol. 3, no. 1, pp. 128-168, 1758.

[42] R. M. Corless *et al.*, "On the Lambert W function," *Adv. Comput. Math.,* vol. 5, no. 1, pp. 329-359, 1996.

[43] G. Machin, "Twelve years of high temperature fixed point research: a review," in *AIP Conference Proceedings*, 2013, pp. 305-316.

[44] D. Lowe, and G. Machin, "Metal–carbon eutectic alloy high-temperature (to 2500 °C) fixed-points as stable reference sources at the National Physical Laboratory," in *Proceedings 11th Int. Metrology Conf. Metrologie 03 (College Français de Métrologie, Toulon, France)*, 2003.

[45] C. Wyatt, *Radiometric calibration: theory and methods*: Elsevier, 2012.

[46] P. Saunders *et al.*, "Uncertainty Budgets for Calibration of Radiation Thermometers below the Silver Point," *Int. J. Thermophys.,* vol. 29, no. 3, pp. 1066-1083, 2008.

[47] P. Saunders, *Radiation thermometry: fundamentals and applications in the petrochemical industry*: SPIE press, 2007.

[48] A. Rogalski, "History of infrared detectors," *Opto-Electron. Rev.,* vol. 20, no. 3, pp. 279-308, 2012.

[49] E. S. Barr, "Historical survey of the early development of the infrared spectral region," *Am. J. Phys,* vol. 28, no. 1, pp. 42-54, 1960.

[50] R. Whatmore, "Pyroelectric devices and materials," *Rep. Prog. Phys.,* vol. 49, no. 12, pp. 1335, 1986.

[51] D. Murphy *et al.*, "640× 512 17 μm microbolometer FPA and sensor development," in *Infrared Technology and Applications XXXIII*, 2007, pp. 65421Z.

[52] Y. Wang, B. J. Potter, and J. J. Talghader, "Coupled absorption filters for thermal detectors," *Opt. Lett.,* vol. 31, no. 13, pp. 1945-1947, 2006.

[53] A. Rogalski, "Infrared detectors: an overview," *Infrared Phys. Technol.,* vol. 43, no. 3-5, pp. 187-210, 2002.

[54] B. Rollin, and E. Simmons, "Long Wavelength Infra-Red Photoconductivity of Silicon at Low Temperatures," in *Proc. Phys. Soc. London, Sect. B*, 1952, pp. 995.

[55] E. Burstein, J. Oberly, and J. Davisson, "Infrared photoconductivity due to neutral impurities in silicon," *Phys. Rev.,* vol. 89, no. 1, pp. 331, 1953.

[56] R. Van Overstraeten, and H. De Man, "Measurement of the ionization rates in diffused silicon pn junctions," *Solid-State Electron.,* vol. 13, no. 5, pp. 583-608, 1970.

[57] J. B. Soole, and H. Schumacher, "InGaAs metal-semiconductor-metal photodetectors for long wavelength optical communications," *IEEE J. Quantum Electron.,* vol. 27, no. 3, pp. 737-752, 1991.

[58] Y. Arslan, F. Oguz, and C. Besikci, "Extended wavelength SWIR InGaAs focal plane array: Characteristics and limitations," *Infrared Phys. Technol.,* vol. 70, pp. 134-137, 2015.

[59] W. E. Tennant *et al.*, "MBE HgCdTe Technology: A Very General Solution to IR Detection, Described by "Rule 07", a Very Convenient Heuristic," *J. Electron. Mater.,* vol. 37, no. 9, pp. 1406-1410, 2008.

[60] H. Lutz *et al.*, "Improved high performance MCT MWIR and LWIR modules," in *Proc. SPIE Infrared Technology and Applications XLV*, 2019, pp. 1100216.

[61] J. Caulfield *et al.*, "Small pixel oversampled IR focal plane arrays," in *Proc. SPIE Infrared Technology and Applications XLI*, 2015, pp. 94512F.

[62] J. Armstrong *et al.*, "HDVIP five-micron pitch HgCdTe focal plane arrays," in *Proc. SPIE Infrared Technology and Applications XL*, 2014, pp. 907033.

[63] C. Corsi, "Infrared: a key technology for security systems," *Adv. Opt. Technol.,* vol. 2012, 2012.

[64] J. G. Harris, and Y.-M. Chiang, "Nonuniformity Correction of Infrared Image Sequences Using the Constant-Statistics Constraint," *IEEE Trans. Image Process.,* vol. 8, no. 8, pp. 1148-1151, 1999.

[65] M. A. Itzler *et al.*, "Crosstalk analysis of integrated Geiger-mode avalanche photodiode focal plane arrays," in *Proc. SPIE Advanced Photon Counting Techniques III*, 2009, pp. 73200Q.

[66] A. Milton, F. Barone, and M. Kruer, "Influence of nonuniformity on infrared focal plane array performance," *Opt. Eng.,* vol. 24, no. 5, pp. 245855, 1985.

[67] J. M. Mooney *et al.*, "Responsivity nonuniformity limited performance of infrared staring cameras," *Opt. Eng.,* vol. 28, no. 11, pp. 281151, 1989.

[68] D. L. Perry, and E. L. Dereniak, "Linear theory of nonuniformity correction in infrared staring sensors," *Opt. Eng.,* vol. 32, no. 8, pp. 1854-1860, 1993.

[69] P. Narendra, and N. Foss, "Shutterless fixed pattern noise correction for infrared imaging arrays," in *Proc. SPIE Technical Issues in Focal Plane Development*, 1981, pp. 44-51.

[70] A. E. Mudau *et al.*, "Non-uniformity correction and bad pixel replacement on LWIR and MWIR images," in *2011 Saudi International Electronics, Communications and Photonics Conference (SIECPC)*, 2011, pp. 1-5.

[71] D. A. Scribner *et al.*, "Adaptive nonuniformity correction for IR focal-plane arrays using neural networks," in *Infrared Sensors: Detectors, Electronics, and Signal Processing*, 1991, pp. 100-109.

[72] C. Zuo *et al.*, "Scene-based nonuniformity correction algorithm based on interframe registration," *JOSA A,* vol. 28, no. 6, pp. 1164-1176, 2011.

[73] E. C. Fest, and S. o. P.-o. I. Engineers, *Stray light analysis and control*: SPIE press Bellingham, 2013.

[74] C. Songtao *et al.*, "Method to remove the effect of ambient temperature on radiometric calibration," *Appl. Opt.,* vol. 53, no. 27, pp. 6274-6279, 2014.

[75] L. Cai *et al.*, "Warming up human body by nanoporous metallized polyethylene textile," *Nat Commun,* vol. 8, no. 1, pp. 496, Sep 19, 2017.

[76] J. Martinek *et al.*, "Large area scanning thermal microscopy and infrared imaging system," *Meas. Sci. Technol.,* vol. 30, no. 3, pp. 035010, 2019.

[77] A. Araújo, "Multi-spectral pyrometry—a review," *Meas. Sci. Technol.,* vol. 28, no. 8, pp. 082002, 2017.

[78] S. P. Mahulikar, H. R. Sonawane, and G. Arvind Rao, "Infrared signature studies of aerospace vehicles," *Prog. Aerosp. Sci.,* vol. 43, no. 7-8, pp. 218-245, 2007.

[79] A. C. Jones, and M. B. Raschke, "Thermal infrared near-field spectroscopy," *Nano letters,* vol. 12, no. 3, pp. 1475-81, Mar 14, 2012.

[80] R. Martın-Palma, L. Vazquez, and J. Martınez-Duart, "Silver-based low-emissivity coatings for architectural windows: Optical and structural properties," *Sol. Energy Mater. Sol. Cells,* vol. 53, no. 1-2, pp. 55-66, 1998.

[81] Q.-C. Zhang, "Recent progress in high-temperature solar selective coatings," *Sol. Energy Mater. Sol. Cells,* vol. 62, no. 1-2, pp. 63-74, 2000.

[82] X. He *et al.*, "High emissivity coatings for high temperature application: Progress and prospect," *Thin Solid Films,* vol. 517, no. 17, pp. 5120-5129, 2009.

[83] E. Sani *et al.*, "Spectrally selective ultra-high temperature ceramic absorbers for high-temperature solar plants," *J. Renewable Sustainable Energy,* vol. 4, no. 3, pp. 033104, 2012.

[84] P. Drude, "Bestimmung der optischen Constanten der Metalle," *Ann. Phys.,* vol. 275, no. 4, pp. 481-554, 1890.

[85] E. Hagen, and H. Rubens, "Das Reflexionsvermögen von Metallen und belegten Glasspiegeln," *Ann. Phys.,* vol. 306, no. 2, pp. 352-375, 1900.

[86] A. Sievers, "Thermal radiation from metal surfaces," *JOSA,* vol. 68, no. 11, pp. 1505-1516, 1978.

[87] H. Kobatake, H. Khosroabadi, and H. Fukuyama, "Normal spectral emissivity measurement of liquid iron and nickel using electromagnetic levitation in direct current magnetic field," *Metall. Mater. Trans. A,* vol. 43, no. 7, pp. 2466-2472, 2012.

[88] C.-D. Wen, and I. Mudawar, "Modeling the effects of surface roughness on the emissivity of aluminum alloys," *Int. J. Heat Mass Transfer,* vol. 49, no. 23-24, pp. 4279-4289, 2006.

[89] H. Bennett, and J. Porteus, "Relation between surface roughness and specular reflectance at normal incidence," *JOSA,* vol. 51, no. 2, pp. 123-129, 1961.

[90] R. A. Dimenna, and R. O. Buckius, "Quantifying specular approximations for angular scattering from perfectly conducting random rough surfaces," *J. Thermophys Heat Transfer,* vol. 8, no. 3, pp. 393-399, 1994.

[91] K. Tang, and R. O. Buckius, "The geometric optics approximation for reflection from two-dimensional random rough surfaces," *Int. J. Heat Mass Transfer,* vol. 41, no. 13, pp. 2037-2047, 1998.

[92] A. Seifter, K. Boboridis, and A. Obst, "Emissivity measurements on metallic surfaces with various degrees of roughness: a comparison of laser polarimetry and integrating sphere reflectometry," *Int. J. Thermophys.,* vol. 25, no. 2, pp. 547-560, 2004.

[93] T. Iuchi, T. Furukawa, and S. Wada, "Emissivity modeling of metals during the growth of oxide film and comparison of the model with experimental results," *Appl. Opt.,* vol. 42, no. 13, pp. 2317-2326, 2003.

[94] L. Wang, S. Basu, and Z. Zhang, "Direct and indirect methods for calculating thermal emission from layered structures with nonuniform temperatures," *J. Heat Transfer,* vol. 133, no. 7, pp. 072701, 2011.

[95] P. Honnerová *et al.*, "New experimental device for high-temperature normal spectral emissivity measurements of coatings," *Meas. Sci. Technol.,* vol. 25, no. 9, pp. 095501, 2014.

[96] O. Riou *et al.*, "Accurate methods for single-band apparent emissivity measurement of opaque materials," *Measurement,* vol. 89, pp. 239-251, 2016.

[97] L. M. Hanssen, S. N. Mekhontsev, and V. B. Khromchenko, "Infrared spectral emissivity characterization facility at NIST," in *Thermosense XXVI*, 2004, pp. 1-12.

[98] B. Zhang, J. Redgrove, and J. Clark, "New apparatus for measurement of the spectral, angular, and total emissivity of solids," *High Temperatures-High Pressures,* vol. 36, no. 3, pp. 289-302, 2004.

[99] C. Monte *et al.*, "Radiation thermometry and emissivity measurements under vacuum at the PTB," *Int. J. Thermophys.,* vol. 30, no. 1, pp. 203, 2009.

[100] R. B. Pérez-Sáez, L. Del Campo, and M. J. Tello, "Analysis of the accuracy of methods for the direct measurement of emissivity," *Int. J. Thermophys.,* vol. 29, no. 3, pp. 1141-1155, 2008.

[101] C.-D. Wen, and I. Mudawar, "Emissivity characteristics of roughened aluminum alloy surfaces and assessment of multispectral radiation thermometry (MRT) emissivity models," *Int. J. Heat Mass Transfer,* vol. 47, no. 17-18, pp. 3591-3605, 2004.

[102] C.-D. Wen, and I. Mudawar, "Emissivity characteristics of polished aluminum alloy surfaces and assessment of multispectral radiation thermometry (MRT) emissivity models," *Int. J. Heat Mass Transfer,* vol. 48, no. 7, pp. 1316-1329, 2005.

[103] F. Wang *et al.*, "Effect of surface microstructures on the infrared emissivity of graphite," *Int. J. Thermophys.,* vol. 35, no. 1, pp. 62-75, 2014.

[104] A. M. Huntz *et al.*, "Oxidation of AISI 304 and AISI 439 stainless steels," *Mater. Sci. Eng., A,* vol. 447, no. 1-2, pp. 266-276, 2007.

[105] S. H. Ham *et al.*, "Relation between emissivity evolution during annealing and selective oxidation of TRIP steel," *Corros. Sci.,* vol. 132, pp. 185-193, 2018.

[106] C.-D. Wen, and I. Mudawar, "Mathematical determination of emissivity and surface temperature of aluminum alloys using multispectral radiation thermometry," *Int. Commun. Heat Mass Transfer,* vol. 33, no. 9, pp. 1063-1070, 2006.

[107] G. Goett *et al.*, "Emissivity and temperature determination on steel above the melting point," *Weld. World,* vol. 57, no. 4, pp. 595-602, 2013.

[108] P. Wang *et al.*, "A new experimental apparatus for emissivity measurements of steel and the application of multi-wavelength thermometry to continuous casting billets," *Rev. Sci. Instrum.,* vol. 89, no. 5, pp. 054903, 2018.

[109] Z. M. Zhang, B. K. Tsai, and G. Machin, *Radiometric Temperature Measurements: II. Applications*, Cambridge, MA: Academic Press, 2009.

[110] L. P. Wang, S. Basu, and Z. M. Zhang, "Direct and Indirect Methods for Calculating Thermal Emission from Layered Structures with Nonuniform Temperatures," *J. Heat Transfer,* vol. 133, no. 7, pp. 072701, 2011.

Chapter 2. Background theory

2.1 Introduction

In this chapter, the background theories for developing an instrument for emissivity measurements are introduced in advance. The knowledge in radiation thermometry focuses on the physics part of emission phenomena of an object. The knowledge in optics focuses on the introduction of the construction of a typical optical system and the criteria for evaluating its performance. After that, the method to develop a qualified optical system for radiation thermometers is discussed from the point of view of optics. Then the relation of the wavelength selection, emissivity uncertainty, and temperature measurement error is discussed. At last, the method for enhancing emissivity of opaque materials is introduced by using the gold-cup method.

2.2 Radiation thermometry

2.2.1 Basic definitions

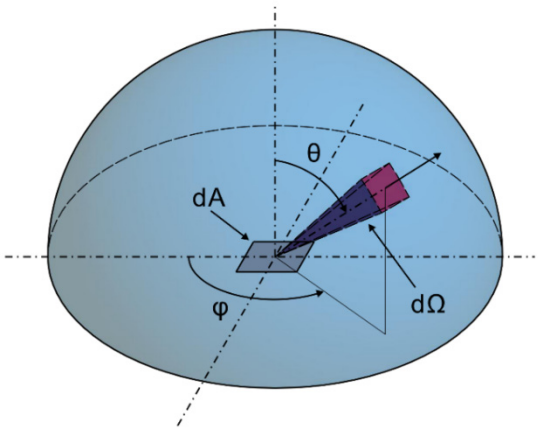

Figure 2.1 Geometry of the radiative model from a surface.

Figure 2.1 shows the schematic geometry diagram of the radiative model. The radiant flux leaves the emission surface A and projects to the space at the direction of (θ, ψ). The physical quantities of the process of radiation are expressed as follows.

Solid angle is a three dimensional angle subtended by the viewing area projected onto a sphere and by the radius of that sphere [1]. The dimensionless unit of solid angle is steradian, with a 4π steradians within a full sphere space.

$$\Omega = a/r^2 \tag{2.1}$$

where a is the viewing area projected onto a sphere, and r is the radius of the sphere.

In spherical coordinates, the infinitesimal solid angle is expressed as:

$$d\Omega = \sin\theta \, d\theta \, d\varphi \tag{2.2}$$

The solid angle of the full space can be obtained by the integral of the spherical area:

$$\Omega = \iint_S \sin\theta \, d\theta \, d\varphi = 4\pi \tag{2.3}$$

Radiant energy intensity is the radiation energy per unit volume:

$$W = \frac{d\mathrm{Q}}{d\mathrm{V}} \tag{2.4}$$

where Q is the radiation energy, and V is the volume.

Radiant power, also named as radiant flux, is the radiant energy emitted, reflected, transmitted or received per second. Particularly, the radiant energy emitted by a surface is also named as emissive power. Radiant power is expressed as:

$$\Phi = \frac{d\mathrm{Q}}{d\mathrm{t}} \tag{2.5}$$

where t is time.

Irradiance is the radiant power received by a surface per unit area:

$$E = \frac{d\Phi}{d\mathrm{A}} \tag{2.6}$$

Radiant exitance, also named as radiant emittance, is the radiant power emitted by a surface per unit area:

$$M = \frac{d\Phi}{d\mathrm{A}} \tag{2.7}$$

Radiant intensity is the radiant power emitted, reflected, transmitted or received by a surface per unit solid angle:

$$I = \frac{d\Phi}{d\Omega} \tag{2.8}$$

Radiance is the radiant power emitted, reflected, transmitted or received by a surface per solid angle per unit projected area. Radiance is an important quantity for radiation thermometry which represents the optical throughput determined by the measurement area, working distance, and the aperture stop of a radiation thermometer. In practice, radiation emitted beyond the nominal measurement area may also be collected by a radiation thermometer, termed as the size of source effect (SSE) [2].

$$L = \frac{d^2\Phi}{d\Omega(\cos\theta\, d\mathrm{A})} \tag{2.9}$$

2.2.2 Blackbody

A blackbody is an ideal body which allows all the incident radiation to pass into it and internally absorbs all the incident radiation, without any radiation reflection and transmission, for all wavelengths and for all incident angles [3, 4]. In thermal equilibrium, a blackbody is also a perfect emitter which emits as much or more thermal radiation as any other body for all wavelengths at a given temperature. The emissive radiation, called “blackbody radiation”, has the following properties.

(1) A blackbody emits the maximum radiation to surroundings simultaneously when its temperature is above the absolute zero. The spectral radiance of blackbody radiation can be given by Planck’s law.

(2) The emissive peak of the spectral irradiance of blackbody radiation follows the Wien’s displacement law at any given temperature.

(3) The total exitance of blackbody radiation can be calculated by Stefan–Boltzmann law at any given temperature.

(4) The emissive radiation from a blackbody is independent of the observing direction. That is, a blackbody is a perfect diffuser, which obeys Lambert's cosine law.

2.2.2.1 Planck's law

Planck's law indicates the spectral radiance of a blackbody in thermal equilibrium at a given temperature [5]:

$$L_{\lambda,b}(\lambda,T)=\frac{2hc_0^2}{\lambda^5[exp(hc_0/\lambda k_B T)-1]}=\frac{c_1}{\pi\lambda^5[exp(c_2/\lambda T)-1]} \tag{2.10}$$

where $h=6.62607015\times10^{-34}\,\mathrm{J\cdot s}$ is the Planck constant, $k_B=1.3806488\times10^{-23}\,\mathrm{J/K}$ is the Boltzmann constant, $c_0=299792458\,\mathrm{m/s}$ is the speed of light in vacuum, c_1 is the first radiation constant, and c_2 is the second radiation constant.

$$c_1=2\pi hc_0^2=3.741771\times10^{-16}\,\mathrm{W\cdot m^2} \tag{2.11}$$

$$c_2=hc_0/k_B=1.438775\times10^{-2}\,\mathrm{m\cdot K} \tag{2.12}$$

The spectral radiant emittance of a blackbody can be expressed as Equation (2.13) as a blackbody is an ideal diffuse emitter.

$$M_{\lambda,b}(\lambda,T)=\frac{c_1}{\lambda^5[exp(c_2/\lambda T)-1]} \tag{2.13}$$

Figure 2.2 shows the spectral radiant exitance of a blackbody at given temperatures.

If $\lambda \ll c_2/T$, Equation (2.10) can be simplified in the short wavelength regime, which is known as Wien approximation. This simplification brings convenient in radiance calculation in the engineering field.

$$L_{\lambda,b}(\lambda,T)=\frac{c_1}{\pi\lambda^5 exp(c_2/\lambda T)} \tag{2.14}$$

2.2.2.2 Wien's displacement law

Wien's displacement law indicates the peak at wavelengths of spectral radiance of blackbody radiation at given temperatures:

$$\lambda_{max} = \frac{b}{T} \tag{2.15}$$

where $b \approx 2897.8\ \mu\text{m} \cdot \text{K}$ is the Wien's displacement constant.

2.2.2.3 Stefan–Boltzmann law

Stefan-Boltzmann law indicates the total radiant exitance of a blackbody by taking the integral of Equation (2.13) over the whole spectrum:

$$M_b(T) = \int_0^\infty \frac{c_1}{\lambda^5[exp(c_2/\lambda T) - 1]} d\lambda = \sigma T^4 \tag{2.16}$$

where $\sigma = 5.670374419 \times 10^{-8}\ \text{W} \cdot \text{m}^{-2} \cdot \text{K}^{-4}$ is the Stefan-Boltzmann constant.

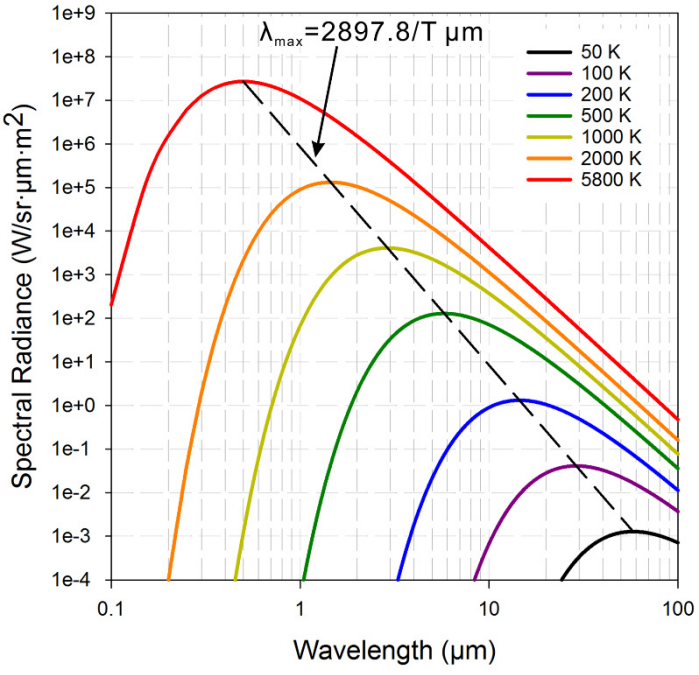

Figure 2.2 Spectral radiant exitance of a blackbody [6].

2.2.2.4 Lambert's cosine law

Lambert's cosine law indicates that the radiant intensity emitted or reflected by an ideal diffuse surface is directly proportional to the cosine of the angle between the incident direction and surface normal:

$$I = I_0 \cos\theta \tag{2.17}$$

where I_0 is the radiant intensity along the surface normal direction.

2.2.3 Radiative properties of real surfaces

2.2.3.1 Emissivity

Emissivity is defined as the energy emitted from a body to that from a blackbody at the same temperature and viewing condition [4]. Emissivity can be termed as different forms with respect to the criteria of the wavelength and viewing condition.

The spectral directional emissivity

The spectral directional emissivity compares the actual spectral, directional radiance of a body to that of a blackbody, which can be expressed as

$$\varepsilon_{\lambda,\Omega}(T,\lambda,\theta,\varphi) = \frac{L_{\lambda,\Omega}(T,\lambda,\theta,\varphi)}{L_{b,\lambda}(T,\lambda)} \tag{2.18}$$

where subscript "b" denotes blackbody, "λ" denotes spectral, "Ω" denotes directional, T is temperature, λ is wavelength, and (θ,φ) is vector direction.

The spectral hemispherical emissivity

The spectral hemispherical emissivity describes the spectral emissive power of a surface to the hemispherical space, which can be expressed as

$$\varepsilon_{\lambda}(T,\lambda) = \frac{M_{\lambda}(T,\lambda)}{M_{b,\lambda}(T,\lambda)} \tag{2.19}$$

The spectral hemispherical emissivity can be related to spectral directional emissivity.

$$\varepsilon_{\lambda}(T,\lambda) = \frac{1}{\pi}\int_0^{2\pi}\int_0^{\pi/2} \varepsilon_{\lambda,\Omega}(T,\lambda,\theta,\varphi)\cos\theta\sin\theta\, d\theta\, d\varphi \tag{2.20}$$

For a diffuse surface, the spectral directional emissivity is independent of the viewing direction.

$$\varepsilon_{\lambda}(T,\lambda) = \varepsilon_{\lambda,\Omega}(T,\lambda,\theta,\varphi) \tag{2.21}$$

The total directional emissivity

The total directional emissivity represents the directional emissive power over the whole spectrum, which can be expressed as

$$\varepsilon_{\Omega}(T,\theta,\varphi) = \frac{L_{\Omega}(T,\theta,\varphi)}{L_{b,\Omega}(T,\theta,\varphi)} = \frac{1}{\sigma T^4}\int_0^{\infty} \varepsilon_{\lambda,\Omega}(T,\lambda,\theta,\varphi) M_{b,\lambda}(T,\lambda)\, d\lambda \tag{2.22}$$

The total hemispherical emissivity

The total hemispherical emissivity represents the emissive power to the full hemispherical space and over the whole spectrum, which can be expressed as

$$\varepsilon(T) = \frac{M(T)}{M_b(T)} = \frac{1}{\sigma T^4}\int_0^{\infty} \varepsilon_{\lambda}(T,\lambda) M_{b,\lambda}(T,\lambda)\, d\lambda \tag{2.23}$$

If a surface has the constant spectral emissivity (lower than 1) for all wavelengths, it is termed as a grey surface. Its total hemispherical emissivity equals the spectral hemispherical emissivity. Particularly, for a grey diffuse surface, its emissivity has following relationships between different forms.

$$\varepsilon(T) = \varepsilon_{\lambda}(T,\lambda) = \varepsilon_{\Omega}(T,\theta,\varphi) = \varepsilon_{\lambda,\Omega}(T,\lambda,\theta,\varphi) \tag{2.24}$$

2.2.3.2 Absorptivity

Absorptivity defines the power of a surface to absorb radiant energy. It is the ratio of the absorbed radiant energy to the total incident power to a surface. Similar to emissivity, absorptivity can be characterised by both the directional and spectral dependence. The incident radiant power to an infinitesimal area dA, from the direction, (θ, φ), over a solid angle, $d\Omega_i$, in the wavelength interval, $d\lambda$, can be written as [4]

$$d^3\Phi_{\lambda,i}(\lambda,\theta,\varphi) = L_{\lambda,i}(\lambda,\theta,\varphi)\cos\theta_i \, d\mathrm{A} d\Omega_\mathrm{i} d\lambda \tag{2.25}$$

where subscript "i" denotes incident.

The spectral directional absorptivity

The spectral directional absorptivity is defined as the fraction of the spectral energy absorbed that is incident from the direction (θ,φ), which can be expressed as

$$\alpha_{\lambda,\Omega}(\lambda,\theta,\varphi,T) = \frac{d^3\Phi_{\lambda,\Omega,a}(\lambda,\theta,\varphi,T)}{d^3\Phi_{\lambda,\Omega,i}(\lambda,\theta,\varphi)} \tag{2.26}$$

where subscript "a" denotes absorbed.

The spectral hemispherical absorptivity

The spectral hemispherical absorptivity represents the fraction of the spectral energy absorbed that is incident from all directions of a surrounding hemisphere, which can be expressed as

$$\alpha_\lambda(\lambda,T) = \frac{d^2\Phi_{\lambda,a}(\lambda,T)}{d^2\Phi_{\lambda,i}(\lambda)} = \frac{\int_\cap \alpha_{\lambda,\Omega}(\lambda,\theta,\varphi,T) L_{\lambda,i}(\lambda,\theta,\varphi)\cos\theta_i \, d\Omega_\mathrm{i}}{\int_\cap L_{\lambda,i}(\lambda,\theta,\varphi)\cos\theta_i \, d\Omega_\mathrm{i}} \tag{2.27}$$

where subscript "$\cap$" denotes the hemispherical space.

The total directional absorptivity

The total directional absorptivity represents the fraction of energy that is absorbed from the energy that is incident from the direction (θ,φ) and over the whole spectrum, which can be expressed as

$$\alpha_\Omega(\theta,\varphi,T) = \frac{d^2\Phi_{\lambda,a}(\theta,\varphi,T)}{d^2\Phi_{\lambda,i}(\theta,\varphi)} = \frac{\int_0^\infty \alpha_{\lambda,\Omega}(\lambda,\theta,\varphi,T) L_{\lambda,i}(\lambda,\theta,\varphi) d\lambda}{\int_0^\infty L_{\lambda,i}(\lambda,\theta,\varphi) d\lambda} \tag{2.28}$$

The total hemispherical absorptivity

The total hemispherical absorptivity represents the fraction of energy absorbed that is incident from the full hemispherical space and over the whole spectrum, which can be expressed as

$$\alpha(T) = \frac{d\Phi_a(T)}{d\Phi_i} = \frac{\int_0^\infty \int_\cap \alpha_{\lambda,\Omega}(\lambda,\theta,\varphi,T) L_{\lambda,i}(\lambda,\theta,\varphi)\, cos\,\theta_i\, d\Omega_\mathrm{i} d\lambda}{\int_0^\infty \int_\cap L_{\lambda,i}(\lambda,\theta,\varphi)\, cos\,\theta_i\, d\Omega_\mathrm{i} d\lambda} \tag{2.29}$$

2.2.3.3 Reflectivity

Reflectivity represents the efficiency of a surface to reflect incident energy. It is the ratio of the reflected radiant power by a surface to the incident radiant power. The reflectivity of a surface depends on two directions: the radiation incident direction and the radiation reflected direction. Reflectivity can also be characterised by both the directional and spectral dependence.

The spectral bidirectional reflectivity

The spectral bidirectional reflectivity expresses the ratio of the spectral energy per unit area reflected to the direction (θ_r, φ_r) to the spectral energy per unit area incident from the direction (θ_i, φ_i).

$$\rho_\lambda(\lambda,\theta_r,\varphi_r,\theta_i,\varphi_i) = \frac{L_{\lambda,r}(\lambda,\theta_r,\varphi_r,\theta_i,\varphi_i)}{L_{\lambda,i}(\lambda,\theta_i,\varphi_i)\, cos\,\theta_i\, d\Omega_\mathrm{i}} \tag{2.30}$$

where subscript "r" denotes reflected.

The spectral directional-hemispherical reflectivity

The spectral directional-hemispherical reflectivity indicates the ratio of energy per area and wavelength reflected to the full hemispherical space to that incident from the direction (θ_i, φ_i).

$$\rho_\lambda(\lambda,\theta_i,\varphi_i) = \frac{d^3\Phi_{\lambda,r}(\lambda,\theta_i,\varphi_i)}{d^3\Phi_{\lambda,i}(\lambda,\theta_i,\varphi_i)} = \int_\cap \rho_\lambda(\lambda,\theta_r,\varphi_r,\theta_i,\varphi_i)\, cos\,\theta_r\, d\Omega_\mathrm{r} \tag{2.31}$$

The spectral hemispherical-directional reflectivity

The spectral hemispherical-directional reflectivity is defined by the ratio of energy per area and wavelength reflected to a specific direction (θ_r, φ_r) to the integrated average energy per area and wavelength incident from the full hemispherical space, which can be expressed as

$$\rho_\lambda(\lambda,\theta_r,\varphi_r)=\frac{\int_\cap \rho_\lambda(\lambda,\theta_r,\varphi_r,\theta_i,\varphi_i)L_{\lambda,i}(\lambda,\theta_i,\varphi_i)\,cos\,\theta_i\,d\Omega_\mathrm{i}}{1/\pi\int_\cap L_{\lambda,i}(\lambda,\theta_i,\varphi_i)\,cos\,\theta_i\,d\Omega_\mathrm{i}} \tag{2.32}$$

The spectral hemispherical reflectivity

The spectral hemispherical reflectivity indicates the ratio of spectral energy reflected by a unit area to the full hemispherical space to that incident from the full hemispherical space, which can be expressed as

$$\rho_\lambda(\lambda)=\frac{d^2\Phi_{\lambda,r}(\lambda)}{d^2\Phi_{\lambda,i}(\lambda)}=\frac{\int_\cap \rho_\lambda(\lambda,\theta_i,\varphi_i)L_{\lambda,i}(\lambda,\theta_i,\varphi_i)\,cos\,\theta_i\,d\Omega_\mathrm{i}}{\int_\cap L_{\lambda,i}(\lambda,\theta_i,\varphi_i)\,cos\,\theta_i\,d\Omega_\mathrm{i}} \tag{2.33}$$

The total bidirectional reflectivity

The total bidirectional reflectivity is the integration of the spectral bidirectional reflectivity over the whole spectrum.

$$\rho(\theta_r,\varphi_r,\theta_i,\varphi_i)=\frac{\int_0^\infty \rho_\lambda(\lambda,\theta_r,\varphi_r,\theta_i,\varphi_i)L_{\lambda,i}(\lambda,\theta_i,\varphi_i)d\lambda}{\int_0^\infty L_{\lambda,i}(\lambda,\theta_i,\varphi_i)d\lambda} \tag{2.34}$$

The total directional-hemispherical reflectivity

The total directional-hemispherical reflectivity is the integration of the spectral directional-hemispherical reflectivity over the whole spectrum.

$$\rho(\theta_i,\varphi_i)=\frac{\int_0^\infty \rho_\lambda(\lambda,\theta_i,\varphi_i)L_{\lambda,i}(\lambda,\theta_i,\varphi_i)d\lambda}{\int_0^\infty L_{\lambda,i}(\lambda,\theta_i,\varphi_i)d\lambda} \tag{2.35}$$

The total hemispherical-directional reflectivity

The total hemispherical-directional reflectivity is the integration of the spectral hemispherical-directional reflectivity over the whole spectrum.

$$\rho(\theta_r,\varphi_r)=\frac{\int_0^\infty \rho_\lambda(\lambda,\theta_r,\varphi_r)L_{\lambda,i}(\lambda)d\lambda}{\int_0^\infty L_{\lambda,i}(\lambda)d\lambda} \tag{2.36}$$

The total hemispherical reflectivity

The total hemispherical reflectivity is the integration of the spectral hemispherical reflectivity over the whole spectrum.

$$\rho = \frac{d\Phi_r}{d\Phi_i} = \frac{\int_0^\infty \int_\cap \rho_\lambda(\lambda, \theta_r, \varphi_r, \theta_i, \varphi_i) L_{\lambda,i}(\lambda, \theta_i, \varphi_i) \cos\theta_i \, d\Omega_\mathrm{i} d\lambda}{\int_0^\infty \int_\cap L_{\lambda,i}(\lambda, \theta_i, \varphi_i) \cos\theta_i \, d\Omega_\mathrm{i} d\lambda} \tag{2.37}$$

2.2.3.4 Transmissivity

Transmissivity represents the effectiveness of incident energy to transmit a semi-transparent material. It is the ratio of the transmitted radiant energy to the total incident energy. Transmissivity can be characterised by both the directional and spectral dependence [7].

The spectral bidirectional transmissivity

The spectral bidirectional transmissivity can be expressed as the ratio of penetrated energy to the direction (θ_r, φ_r) to the energy incident from direction (θ_i, φ_i)] per area and wavelength.

$$\tau_\lambda(\lambda, \theta_r, \varphi_r, \theta_i, \varphi_i) = \frac{L_{\lambda,t}(\lambda, \theta_t, \varphi_t, \theta_i, \varphi_i)}{L_{\lambda,i}(\lambda, \theta_i, \varphi_i) \cos\theta_i \, d\Omega_\mathrm{i}} \tag{2.38}$$

where subscript "t" denotes transmitted.

The spectral hemispherical transmissivity

The spectral hemispherical transmissivity describes the ratio of penetrated energy per unit area and wavelength to the full hemispherical space to the energy incident from all directions of a surrounding hemisphere.

$$\tau_\lambda(\lambda) = \frac{\int_\cap \tau_\lambda(\lambda, \theta_i, \varphi_i) L_{\lambda,i}(\lambda, \theta_i, \varphi_i) \cos\theta_i \, d\Omega_\mathrm{i}}{\int_\cap L_{\lambda,i}(\lambda, \theta_i, \varphi_i) \cos\theta_i \, d\Omega_\mathrm{i}} \tag{2.39}$$

The total hemispherical transmissivity

The total hemispherical transmissivity is the integration of spectral hemispherical transmissivity over the whole spectrum range, which can be expressed as

$$\tau = \frac{d\Phi_\tau}{d\Phi_i} = \frac{\int_0^\infty \int_\cap \tau_\lambda(\lambda, \theta_t, \varphi_t, \theta_i, \varphi_i) L_{\lambda,i}(\lambda, \theta_i, \varphi_i) \cos\theta_i \, d\Omega_\mathrm{i} d\lambda}{\int_0^\infty \int_\cap L_{\lambda,i}(\lambda, \theta_i, \varphi_i) \cos\theta_i \, d\Omega_\mathrm{i} d\lambda} \tag{2.40}$$

2.2.3.5 Kirchhoff's law

Kirchhoff's law indicates that the spectral directional absorptivity equals spectral directional emissivity of a body in thermal equilibrium [3]. Kirchhoff's law can be expressed with different forms with respect to associating restrictions, which will be used to calculate emissivity by indirect methods [4]. The basic form can be expressed as

$$\alpha_{\lambda,\Omega}(\lambda,\theta,\varphi,T) = \varepsilon_{\lambda,\Omega}(\lambda,\theta,\varphi,T) \tag{2.41}$$

The total directional absorptivity equals the total directional emissivity only if the incident radiation has the same spectral distribution proportional to that of a blackbody at the specified temperature, or the illuminated body has a directional-grey surface.

$$\alpha_{\Omega}(\theta,\varphi,T) = \varepsilon_{\Omega}(\theta,\varphi,T) \tag{2.42}$$

The spectral hemispherical absorptivity equals the spectral hemispherical emissivity only if the incident radiation is independent of angle or the illuminated body has diffuse surface.

$$\alpha_{\lambda}(\lambda,T) = \varepsilon_{\lambda}(\lambda,T) \tag{2.43}$$

The total hemispherical absorptivity equals the total hemispherical emissivity only if these assumptions are valid: (1) the incident radiation is independent of angle and has a spectral distribution proportional to that of a blackbody at the specified temperature; (2) the incident radiation is independent of angle and the illuminated body has a directional-grey surface; (3) the incident radiation has spectral distribution proportional to that of a blackbody from each direction or the illuminated body has a diffuse-spectral surface; (4) or the illuminated body has a diffuse-grey surface.

$$\alpha(T) = \varepsilon(T) \tag{2.44}$$

Kirchhoff's law is valid in thermodynamic equilibrium within an isothermal enclosure and, thereafter, no net heat transfer is occurring on the surface. In practice, this requirement is very difficult to be satisfied. If an object can maintain itself in a local thermodynamic equilibrium, then the energy states that take part in the emission and absorption processes can be regarded to a very close approximation. In this case, Kirchhoff's law can be extended to non-equilibrium systems and the radiative properties

of objects which can maintain their own thermal status are independent of the surrounding radiation field.

2.2.3.6 Relationship between emissivity, absorptivity, reflectivity, and transmissivity

For the most general situation of a semi-transparent medium, the radiation incident to that medium may be absorbed, reflected or transmitted. From the view of energy balance, the relationship obeys

$$Q_i = Q_a + Q_r + Q_t \tag{2.45}$$

By applying the definition of absorptivity in spectral directional quantity, and reflectivity and transmissivity in spectral directional-hemispherical quantities, Equation (2.45) can be rewritten as

$$\alpha_{\lambda,\Omega}(\lambda,\theta,\varphi,T) + \rho_{\lambda,\Omega}(\lambda,\theta,\varphi,T) + \tau_{\lambda,\Omega}(\lambda,\theta,\varphi,T) = 1 \tag{2.46}$$

For an opaque body, its transmissivity equals zero. In this case, Equation (2.46) can be simplified to

$$\alpha_{\lambda,\Omega}(\lambda,\theta,\varphi,T) + \rho_{\lambda,\Omega}(\lambda,\theta,\varphi,T) = 1 \tag{2.47}$$

With the consideration of Kirchhoff's law, the spectral directional emissivity and reflectivity of an opaque body in thermal equilibrium can be expressed as

$$\varepsilon_{\lambda,\Omega}(\lambda,\theta,\varphi,T) + \rho_{\lambda,\Omega}(\lambda,\theta,\varphi,T) = 1 \tag{2.48}$$

If the incident spectral energy is arriving at an opaque body from all directions over the hemisphere, Equation (2.48) can be expressed as

$$\varepsilon_{\lambda}(\lambda,T) + \rho_{\lambda}(\lambda,T) = 1 \tag{2.49}$$

Particularly, for the total hemispherical values of absorptivity and reflectivity, Equation (2.49) turns to

$$\varepsilon(T) + \rho(T) = 1 \tag{2.50}$$

2.3 Optics

The propagation of radiation is the propagation of electromagnetic wave in essence, which can be explained by classical electromagnetic theory. The radiation behaviours such as the reflection, refraction, and scattering are the interaction between electromagnetic wave and medium. This section discusses the basic knowledge in electromagnetic theory, geometrical optics and the criteria for evaluating the image quality of an optical system.

2.3.1 Classical electromagnetic theory

Maxwell's equations can be used to describe the interaction of electric and magnetic fields within an isotropic medium, including vacuum, under the condition of no accumulation of static charge. Maxwell's equations can be expressed by four fundamental equations in differential forms with SI units [8]:

Gauss's law

$$\nabla \cdot \mathbf{D} = \rho_f \tag{2.51}$$

Gauss's law for magnetism

$$\nabla \cdot \mathbf{B} = 0 \tag{2.52}$$

Maxwell–Faraday equation

$$\nabla \times \mathbf{E} = -\frac{\partial \mathbf{B}}{\partial t} \tag{2.53}$$

Ampere's circuital law

$$\nabla \times \mathbf{H} = \mathbf{J} + \frac{\partial \mathbf{D}}{\partial t} \tag{2.54}$$

where **D** is the electric displacement, **B** is the magnetic induction, **E** is the electric field intensity, **H** is the magnetic field intensity, ρ_f is the free charge density, and **J** is the free electric current density.

2.3.2 Materials equations

The classic Maxwell equations contains five basic quantities **D**, **B**, **E**, **H**, and **J**. When applying Maxwell equations to analyse a given distribution of electric and magnetic field vectors, it is necessary to know the response of medium to the electromagnetic field. For the linear, homogeneous, isotropic medium, the relationships can be described by materials equations [8].

$$\mathbf{J} = \sigma_c \mathbf{E} \tag{2.55}$$

$$\mathbf{D} = \varepsilon_p \mathbf{E} \tag{2.56}$$

$$\mathbf{B} = \mu \mathbf{H} \tag{2.57}$$

where σ_c is the specific conductivity, ε_p is the permittivity, and μ is the magnetic permeability.

2.3.3 Wave propagation

The propagation of a plane wave within isotropic homogeneous medium is the combination of the oscillation of electric and magnetic waves, as shown in Figure 2.3, which are perpendicular to the traveling direction.

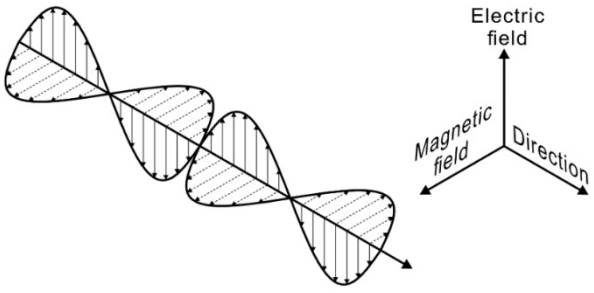

Figure 2.3 Schematic diagram of the wave propagation.

When a plane wave propagates within isotropic medium, the wave traveling the positive x direction is given by the wave equation:

$$E_y = E_{y,0} exp\left[i\omega\left(t - \frac{n}{c_0}x\right)\right] \tag{2.58}$$

where ω is the angular frequency, t is the time, n is the refractive index, and c_0 is the speed of light.

When a plane wave propagates within imperfect dielectric material, it is necessary to consider the wave attenuation. Then Equation (2.58) can be rewritten as:

$$E_y = E_{y,0} exp\left[i\omega\left(t - \frac{\bar{n}}{c_0}x\right)\right] \tag{2.59}$$

where $\bar{n} = n - i\kappa$ is the complex refractive index, and κ is the extinction coefficient.

From the point of view of energy balance, the rate of energy transfer in a unit volume equals the rate of electromagnetic energy flux leaving that space plus the work done on a charge distribution, which is given by Poynting's theorem.

$$-\frac{\partial w}{\partial \mathrm{t}} = \nabla \cdot \mathbf{S} + \mathbf{J} \cdot \mathbf{E} \tag{2.60}$$

where w is the energy density, and $\mathbf{S}$ is the Poynting vector.

The Poynting vector indicates the instantaneous energy carried by an electromagnetic wave per unit time and per unit area.

$$\mathbf{S} = \mathbf{E} \times \mathbf{H} \tag{2.61}$$

The magnitude of the Poynting vector is given by

$$|\mathbf{S}| = \frac{\bar{n}}{\mu c_0}|\mathbf{E}|^2 \tag{2.62}$$

2.3.4 Law of reflection and refraction

When the electromagnetic wave propagates to another material's interface, it occurs in reflection and refraction at the same time, as shown in Figure 2.4.

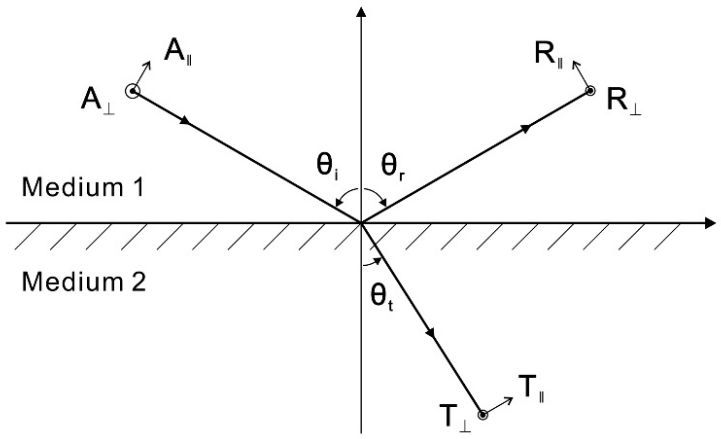

Figure 2.4 Schematic diagram of reflection and refraction.

The relationship between incident, reflected, and refracted waves for a nonattenuating medium can be expressed as

$$n_1 \sin\theta_i = n_1 \sin\theta_r = n_2 \sin\theta_t \tag{2.63}$$

where n_1 is the complex refractive index of incident medium, and n_2 is the complex refractive index of refracted medium.

Snell's law indicates the relation between the incident wave and refracted wave, which can be expressed as

$$\frac{\sin\theta_t}{\sin\theta_i} = \frac{n_1}{n_2} \tag{2.64}$$

Fresnel's equation gives the spectral directional hemispherical reflectivity for unpolarised ray hitting upon an interface between two perfect dielectric media.

$$\rho_\lambda(\lambda,\theta) = \frac{\rho_{\lambda\parallel}(\lambda,\theta) + \rho_{\lambda\perp}(\lambda,\theta)}{2} = \frac{1}{2}\left[\frac{\tan^2(\theta_i-\theta_t)}{\tan^2(\theta_i+\theta_t)} + \frac{\sin^2(\theta_i-\theta_t)}{\sin^2(\theta_i+\theta_t)}\right] \tag{2.65}$$

For the special case that the incident wave is normal to the interface, the normal-hemispherical reflectivity can be converted from Equation (2.65) to

$$\rho_{\lambda,n}(\lambda) = \left(\frac{n_2-n_1}{n_2+n_1}\right)^2 \tag{2.66}$$

For opaque nonattenuating materials, the spectral normal hemispherical emissivity can be obtained by Equations (2.41), (2.47), and (2.66). Thereafter, emissivity of optical smooth materials can be predicted if the refractive index of medium is known.

$$\varepsilon_{\lambda,n}(\lambda,T) = 1 - \left(\frac{n_2 - n_1}{n_2 + n_1}\right)^2 = \frac{4(n_2/n_1)}{[(n_2/n_1)+1]^2} \tag{2.67}$$

For the absorbing materials, the behaviour of reflection and refraction becomes complex, more details can be obtained from [4] and [8].

2.3.5 Geometrical optics

In this section, the knowledge in geometric optic is introduced to offer the essential knowledge on developing an optical system by using ray tracing method [9]. A typical optical system consists of a singlet is the simplest focal system, as shown in Figure 2.5. In this system, the space is separated into object space and image space by the optical centre. Quantities with superscript ($'$) are in imaging space whilst those without ($'$) are in object space. Focal points, F and F$'$, denote the position where the singlet converges the collimated rays to the axis. Principle points, P and P$'$, denote the position where the incident and outgoing rays have the same magnification. Axial conjugate points, O and O$'$, denote the object point and image point on axis.

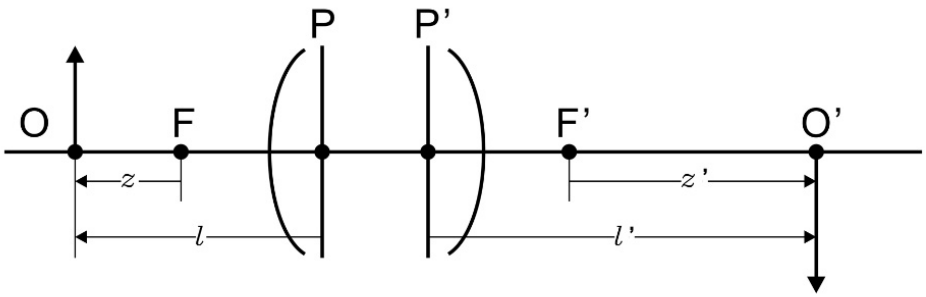

Figure 2.5 Schematic diagram of a focal system.

For an optical system with the given focal length, f, if the objective distance, l, is known, the image distance, l', can be determined by using the Gaussian lens formula with the paraxial approximation, assuming that the system has the same medium in object and image space.

$$1 = \frac{f}{l} + \frac{f'}{l'} \tag{2.68}$$

By applying the distance, z and z', from the conjugate points to the focal points, the relation can also be expressed by Newton's equation.

$$zz' = ff' \tag{2.69}$$

If the object height, h, is given, the image height, h', can be calculated by

$$h' = -\frac{f}{z}y = -\frac{z'}{f'}y \tag{2.70}$$

The transverse magnification is defined by the ratio of image height to object height.

$$M = \frac{h'}{h} \tag{2.71}$$

Basic concept of an imaging system

Figure 2.6 shows the basic concept of an imaging system. A typical imaging system consists of the lens, aperture stop, field stop, and imaging plane. Particularly, the entrance and exit pupils are the image of the aperture stop formed by the lens. The entrance widow is the image of the field stop formed by the whole optical system.

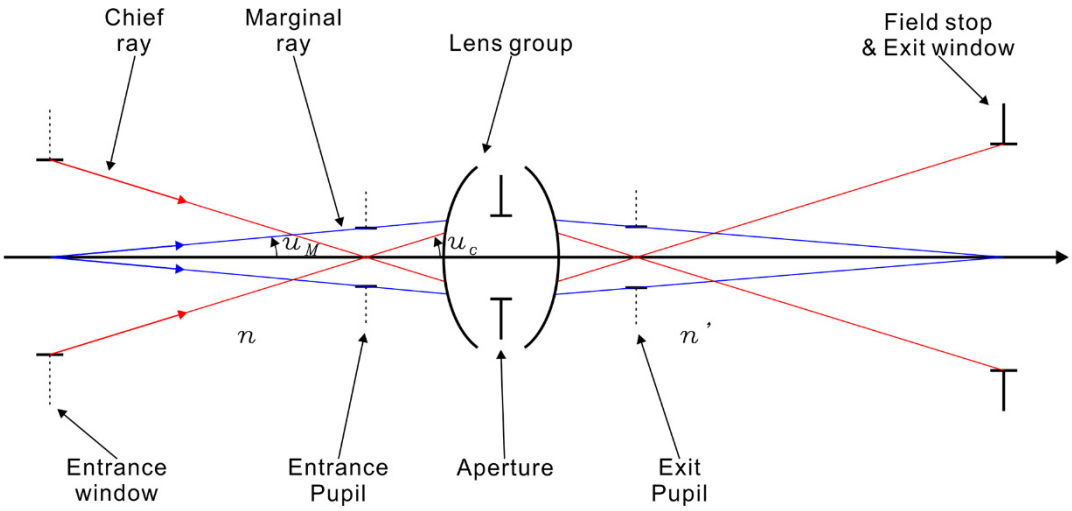

Figure 2.6 Schematic diagram of the basic concept of an imaging system.

Aperture stop: The aperture that limits the size of the axial beam passing through the system.

Chief ray: A ray that passes through the centre of the aperture stop and the edge of the image or object. The chief ray always passes through the centre of the aperture stop.

Marginal ray: The extreme ray from the axial point of the object through the edge of the aperture stop.

Entrance pupil: The image of the aperture stop in object space. The chief ray passes or appears to pass through the centre of the entrance pupil.

Exit pupil: The image of the aperture stop in image space. The chief ray passes or appears to pass through the centre of the exit pupil.

Field stop: An aperture that limits the size of an intermediate or final image.

Entrance window: The image of the field stop in object space. The chief ray passes or appears to pass through the centre of the entrance window.

Exit window: The image of the field stop in image space. The chief ray passes or appears to pass through the centre of the exit window.

F-number (FN): The effective focal length of an objective divided by its entrance-pupil diameter. F-number describes the capability of a lens to accept rays. If the object is located at infinity, F-number can be expressed as

$$FN = \frac{f}{D_{ep}} \tag{2.72}$$

where f is the focal length, and D_{ep} is the diameter of entrance pupil.

Numerical aperture (NA): The refractive index times the sine value of the half maximum slope angle.

$$NA = n_i \sin u_M \tag{2.73}$$

where n_i is the refractive index, and u_M is the paraxial maximum marginal ray angle.

Field-of-view (FOV): If the object is not located at infinity, FOV is expressed as the size of the entrance window. If the object is located at the infinity, FOV is expressed as the angular term, which can be expressed as

$$FOV = 2u_C = 2\tan^{-1}\left(\frac{D_{ExW}}{f'}\right) \tag{2.74}$$

where u_C is the paraxial maximum chief ray angle, and D_{ExW} is the diameter of exit window.

In radiation thermometry, measurements are undertaken at a finite working distance. FOV is defined as the ratio of the size of the measurement area to the working distance by using a single-point radiation thermometer. It is also be named as distance to target ratio (DTR), which can be expressed as

$$DTR = \frac{D_{meas}}{WD} : 1 \tag{2.75}$$

where D_{meas} is the size of the measurement area, and WD is the working distance.

2.3.6 Image quality

The generalised model of a typical optical system is shown in Figure 2.7. The coordinate of object plane, exit pupil, and image plane are $x_o o y_o$, $\xi o \eta$, and $x_i o y_i$, respectively. The distance between the object plane and entrance pupil plane is d_o, and the distance between the image plane and exit pupil plane is d_i. The lenses are treated as a black box placed between the entrance pupil and exit pupil planes.

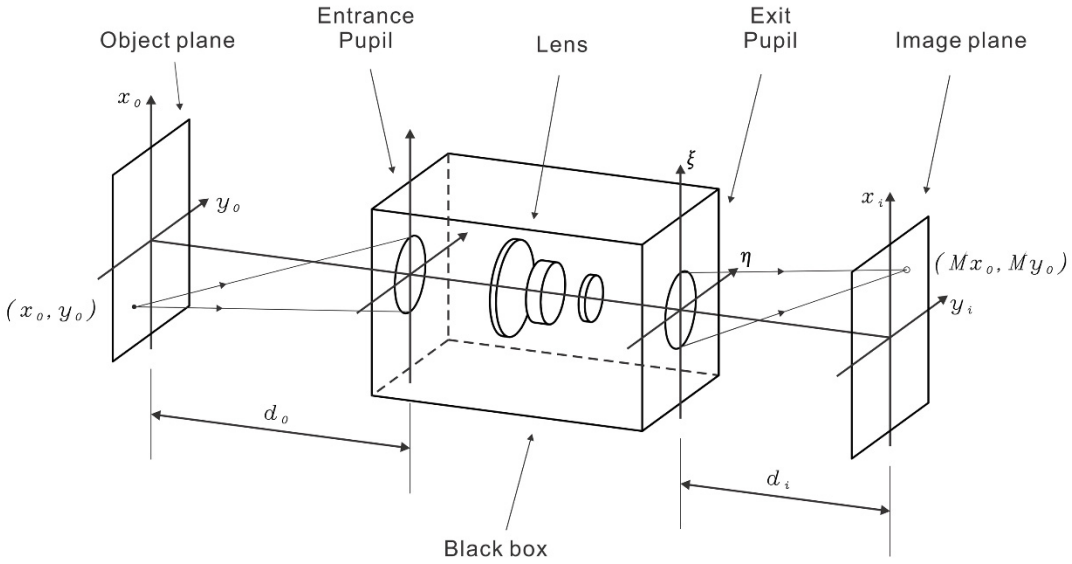

Figure 2.7 Generalised model of a typical optical system.

The diffraction limited system indicates that a diverging spherical wave emitting from a point-source object can be converted by the system to a new perfect spherical wave towards an ideal point in the image plane, where the location of ideal image point is related to the location of the original object point by the magnification. The optical system is degraded by aberrations if the wavefront leaving the exit pupil departs significantly from the ideal spherical wave shape, leading to the defects in the spatial frequency response of the imaging system. The final image formed by a diffraction limited system is not a perfect spot but affected by the diffraction effects due to limitation of entrance and exit pupils. The best achievable image quality of a generalised system can be understood by analysing the properties of a diffraction limited imaging system.

Monochromatic illumination system

If the object is illuminated by monochromatic lights, its image function in the image plane can be expressed as

$$U_i(x_i, y_i) = \iint_{-\infty}^{+\infty} h(x_i, y_i; x_o, y_o) U_o(x_o, y_o)\, dx_o\, dy_o \tag{2.76}$$

where $h(x_i, y_i; x_o, y_o)$ is the impulse response, or point spread function (PSF), at image coordinates in response to a point-source at object coordinates, and $U_o(x_o, y_o)$ is the object function.

The PSF can be rewritten in reduced coordinates by applying the Fresnel diffraction formula.

$$h(x_i - \tilde{x}_o, y_i - \tilde{y}_o) = \frac{C}{\lambda d_i} \iint_{-\infty}^{+\infty} P(\xi, \eta) \exp\left\{-j \frac{2\pi}{\lambda d_i} [(x_i - \tilde{x}_o)\xi + (y_i - \tilde{y}_o)\eta]\right\} d\xi\, d\eta \tag{2.77}$$

where C is a constant amplitude, $\tilde{x}_o = Mx_o$ and $\tilde{y}_o = My_o$ are the reduced coordinates in object space, M is the ideal transverse magnification, and $P(\xi, \eta)$ is the pupil function (it is 1 inside the lens and 0 outside).

Equation (2.77) indicates that the impulse response of a diffraction limited system is the Fraunhofer diffraction pattern (also the Fourier transform) of the exit pupil, centred on the image coordinates $x_i = Mx_o$ and $y_i = My_o$.

By defining the ideal image predicted by geometrical optics

$$U_g(x_i, y_i) = \frac{1}{|M|} U_o\left(\frac{x_i}{M}, \frac{y_i}{M}\right) \tag{2.78}$$

and the impulse response

$$\tilde{h}(x_i - \tilde{x}_o, y_i - \tilde{y}_o) = \frac{1}{|M|} h(x_i - \tilde{x}_o, y_i - \tilde{y}_o) \tag{2.79}$$

Equation (2.76) can be rewritten as the form of

$$\begin{aligned} U_i(x_i, y_i) &= \iint_{-\infty}^{+\infty} U_g(\tilde{x}_o, \tilde{y}_o)\tilde{h}(x_i - \tilde{x}_o, y_i - \tilde{y}_o) d\tilde{x}_o \, d\tilde{y}_o \\ &= U_g(x_i, y_i) * \tilde{h}_i(x_i, y_i) \end{aligned} \tag{2.80}$$

Incoherent polychromatic illumination system

For the object illuminated by incoherent polychromatic light, the intensity in the image plane obeys

$$I_i(x_i, y_i) = C' \iint_{-\infty}^{+\infty} I_g(\tilde{x}_o, \tilde{y}_o) h_I(x_i - \tilde{x}_o, y_i - \tilde{y}_o) d\tilde{x}_o \, d\tilde{y}_o \tag{2.81}$$

where C' is the constant, $I_g(\tilde{x}_o, \tilde{y}_o)$ is the intensity of ideal image, and $h_I(x_i - \tilde{x}_o, y_i - \tilde{y}_o) = |h_i(x_i - \tilde{x}_o, y_i - \tilde{y}_o)|^2$ is the intensity point spread function.

The normalised frequency spectra, $\mathcal{G}_g$, $\mathcal{G}_g$, and $\mathcal{H}_{OTF}$, are defined as

$$\mathcal{G}_g(f_x, f_y) = \frac{I_g^F(f_x, f_y)}{I_g^F(0,0)} \tag{2.82}$$

and

$$\mathcal{G}_i(f_x, f_y) = \frac{I_i^F(f_x, f_y)}{I_i^F(0,0)} \tag{2.83}$$

and

$$\mathcal{H}_{OTF}(f_x, f_y) = \frac{H_I^F(f_x, f_y)}{H_I^F(0,0)} \tag{2.84}$$

where $I_g^F(f_x, f_y)$ and $I_i^F(f_x, f_y)$ are the Fourier transform of $I_g(\tilde{x}_o, \tilde{y}_o)$ and $I_i(x_i, y_i)$, and $H_I^F(f_x, f_y)$ is the Fourier transform of $h_I(x_i, y_i)$.

Application of the convolution theorem to Equation (2.81) then yields the frequency-domain relation, which can be expressed as

$$\mathcal{G}_i(f_x, f_y) = \mathcal{H}_{OTF}(f_x, f_y)\mathcal{G}_g(f_x, f_y) \tag{2.85}$$

where $\mathcal{G}_g(f_x, f_y)$ is the normalised spectra of ideal image, $\mathcal{G}_i(f_x, f_y)$ is the normalised spectra of image, $\mathcal{H}_{OTF}(f_x, f_y)$ is the normalised transfer function of the system, which is also termed as optical transfer function (OTF) of incoherent illumination system. For the actual system, OTF is a complex function, which can be expressed as

$$\mathcal{H}_{OTF}(f_x, f_y) = H_{MTF}(f_x, f_y)\exp[-j\phi(f_x, f_y)] \tag{2.86}$$

where $H_{MTF}(f_x, f_y)$ is the modulation transfer function (MTF), and $\phi(f_x, f_y)$ is the phase transfer function (PTF).

MTF is the ratio of image modulation to object modulation, which describes the modulation depth as the function of spatial frequency, ranging between 0 and 1.

$$MTF(f_x, f_y) = \frac{|\mathcal{G}_i(f_x, f_y)|}{|\mathcal{G}_g(f_x, f_y)|} \tag{2.87}$$

For the diffraction limited imaging system with an exit pupil of full width with D_{ExP}, the image-space cut-off frequency can be given by

$$f_{cutoff} = \frac{D_{ExP}}{\lambda d_i} \tag{2.88}$$

Diffraction limited MTFs represent the best performance that an optical system can achieve. For an actual system, optical aberrations lead to the defects in special frequency response. If the imaging system is designed with MTF value greater than 0.5 at the specific resolution, it can be regarded to offer a good contrast for observing the objects of interest [10].

When the aperture of a diffraction limited system is circular, $\tilde{h}_i(x_i, y_i)$ is the two dimensional Fourier transform, which gives the Airy-function

$$I(r_{Airy}) = \left[\frac{kD_{ExP}^2}{8d_i}\right]^2 \left[\frac{2J_1(kD_{ExP}r_{Airy}/2d_i)}{kD_{ExP}r_{Airy}/2d_i}\right]^2 \tag{2.89}$$

where J_1 is the first-order Bessel function of the first kind, $k = 2\pi/\lambda$ is the wavenumber, D_{ExP} is the diameter of the exit pupil, and r_{Airy} is radius of the Airy pattern.

The first zero of the Airy pattern locates at the distance

$$r_{Airy}(0) = \frac{1.22 d_i \lambda}{D_{ExP}} \tag{2.90}$$

According to the Rayleigh criterion of resolution, two incoherent point sources can be resolved by a diffraction limited system, which comes with a circular pupil, when the centre of the Airy pattern of the first source locates on the first zero of the Airy pattern of the second source.

2.4 Design considerations of radiation thermometers

2.4.1 Systematic signal output

Radiation thermometer is used to receive the radiation leaving an object and output the result as electrical signals. Figure 2.8 shows a schematic diagram of a typical radiation thermometer equipped with a single-point photodiode. The radiation leaving the surface is absorbed and scattered by the atmosphere along the optical path. The penetrated radiation is focused by the lens to the photodiode and transferred to electrical signals.

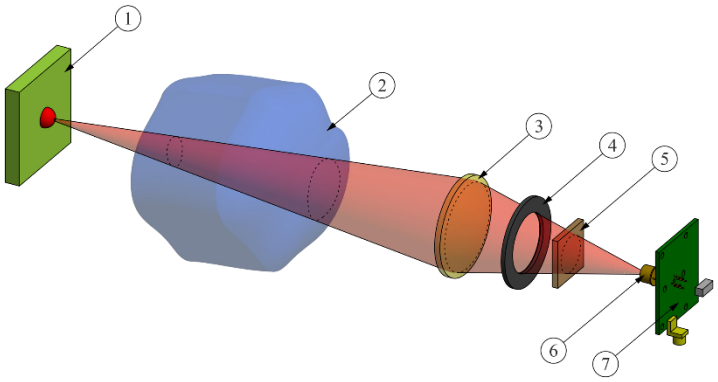

Figure 2.8 Schematic diagram of a radiation thermometer: object (1); atmosphere (2); lens (3); aperture stop (4); filter (5); photodiode (6); signal processor (7).

The electrical signal output can be expressed as

$$S_s(\lambda, T_s) = \Omega_s A_s \tau_{air} \int_{\lambda_1}^{\lambda_2} \varepsilon_s(\lambda, T_s) L_b(\lambda, T_s) R(\lambda) \tau(\lambda)\, d\lambda \tag{2.91}$$

where subscript "b" denotes blackbody, "s" denotes sample, Ω is the solid angle, A is the measurement area upon the target, τ_{air} is the propagation coefficient of the atmosphere, $R(\lambda)$ is the spectral responsivity of detectors, and $\tau(\lambda)$ is the total transmissivity of optical systems.

The spectral responsivity of a detector and total transmissivity of a radiometer's optical system are functions of wavelength. If a narrow band pass filter is used in the system, these two factors can be regarded as independent of wavelength. Equation (2.91) can be rewritten as

$$S_s(\lambda, T_s) = \Omega_s A_s \tau_{air} \tau R \int_{\lambda-\Delta\lambda/2}^{\lambda+\Delta\lambda/2} \varepsilon_s(\lambda, T_s) L_b(\lambda, T_s)\, d\lambda \tag{2.92}$$

In this equation, the correction factor k_c is defined as

$$k_c = \Omega_s A_s \tau_{air} \tau R \tag{2.93}$$

The correction factor k_c is the constant which is determined by the solid angle, measurement area, atmosphere properties, and spectral responsivity of the detector. In practice, the value of k_c can be determined through calibration using a blackbody source at the temperature of interest.

2.4.2 Wavelength selection, emissivity uncertainty, and measurement error

Each type of radiation thermometer works at its specific wavelength due to use of respective detectors. For a given output signal obtained from a target, substituting a measured emissivity, ε_{meas}, will yield a measured temperature, T_{meas}, whilst substituting the true emissivity, ε, will yield the true temperature, T. For a narrow waveband radiation thermometer, the relation between the emissivity variance, $\delta\varepsilon$, and expected error of a temperature measurement, δT, can be expressed as Equation (2.94),

by assuming the spectral responsivity of the instrument and the emissivity are independent to that waveband [11].

$$\delta\varepsilon = \frac{\int_{\lambda_1}^{\lambda_2} L_b(\lambda, T)\, d\lambda - \int_{\lambda_1}^{\lambda_2} L_b\big(\lambda, T(1+\delta T)\big)\, d\lambda}{\int_{\lambda_1}^{\lambda_2} L_b\big(\lambda, T(1+\delta T)\big)\, d\lambda} \tag{2.94}$$

where $\delta\varepsilon$ is the fractional variance in emissivity, $\varepsilon_{meas} = \varepsilon(1+\delta\varepsilon)$ and δT is the expected fractional error in measured temperature, $T_{meas} = T(1+\delta T)$.

Figure 2.9 shows the expected temperature error, in °C, due to a 1% emissivity variance for temperature from 0 to 3000 °C. In general, the shorter wavelength thermometers return smaller errors than the long wavelength thermometers. To obtain a higher accuracy measurement, it is necessary to select a shorter wavelength radiation thermometer whilst it can respond to the radiation from a target at the temperature of interest. Emissivity uncertainty, $\Delta\varepsilon$, can be converted to the emissivity variance from Equation (2.94), which offers guidance for understanding the expected temperature measurement error when a emissivity value is selected as the reference.

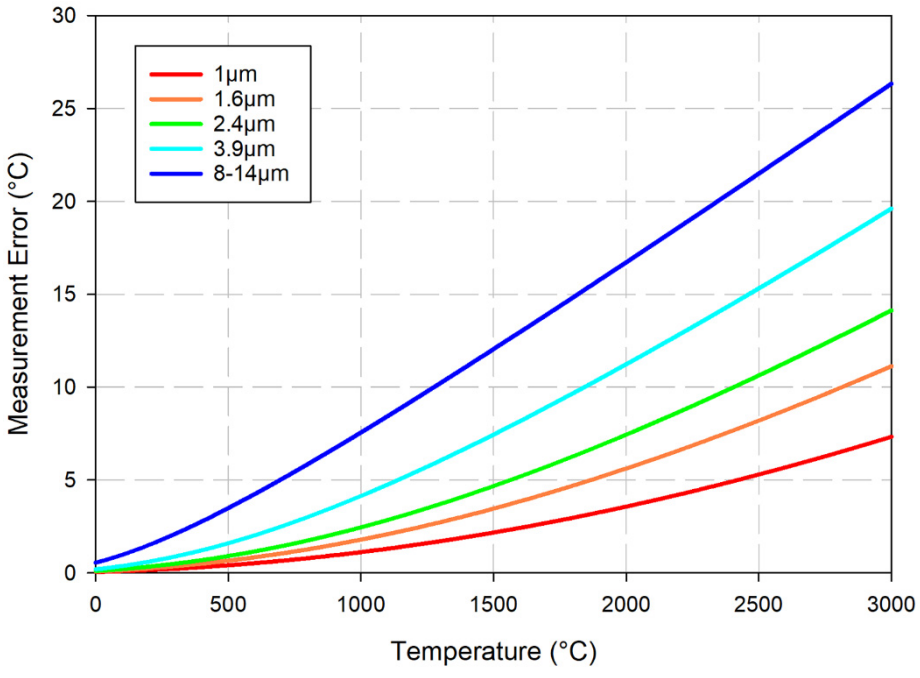

Figure 2.9 Expected temperature measurement error in °C due to a 1% emissivity variance.

In the short wavelength regime, Planck's law can be simplified by Wien approximation.

$$L_{\lambda,b}(\lambda,T)=\frac{c_1}{\pi\lambda^5 exp(c_2/\lambda T)} \tag{2.95}$$

The derivative of Equation (2.95) with respect to temperature can be used to indicate the measured emissivity variance due to the error in temperature measurements.

$$\Delta\varepsilon=-\frac{c_2\Delta T}{\lambda T^2} \tag{2.96}$$

where ΔT is the error in measured temperature, $\Delta T=T_{meas}-T$.

If the error in measured temperature is set to 1 °C, Equation (2.96) brings an important quantity in the engineering, known as percent-per-degree ($\%/°C$). This quantity represents the percentage change in output signal for a 1 °C raise in target temperature, which is used to undertake a quick estimation of the measurement accuracy of a radiation thermometer.

$$\%/°C\approx 100\times\frac{c_2}{\lambda T^2} \tag{2.97}$$

2.4.3 Confidence measurement area

Confidence measurement area is an important quantity for developing a high-quality radiation thermometer which indicates its minimum measurable target size. In radiation thermometry, the confidence measurement area, or the nominal measurement area, is defined as the size of a diffuse surface area which encloses 90% (or above) radiant energy at a given working distance, by comparing that with the size of infinite measurement area [12]. If a single-point radiation thermometer is used, the edge of its measurement area appears a region from contrastive to blur. This phenomenon is inevitable due to the optical limitation.

Figure 2.10 shows the schematic diagram of the measurement area of a single-point radiation thermometer at an arbitrary working distance. In this system, the sensor of a single-element detector projects its image on the object plane, indicating the area for measuring. The nominal measurement area is determined by the image formed of chief rays emitting from the edge of the sensor, showing as a red circle in the figure. The blurred region always exists even for an ideal optical system without reflection and scattering. This can be classified within two cases. If a diffraction limited system is used,

the blurred region is due to the diffraction phenomena distributing around the edge. If the optical system contains aberrations, the diffraction pattern turns to a blurred spot distributing along the edge. The blurred region of a diffraction limited optical system is always narrower than that of the system containing aberrations if these systems have the same F-number. In this case, an optical system with a higher image quality can produce a smaller measurement area for radiation thermometers, which means a better resolution for measurements. Meanwhile, for a given diffraction limited system, the portion of blurred region over the whole measurement area becomes larger if a smaller sensor is used.

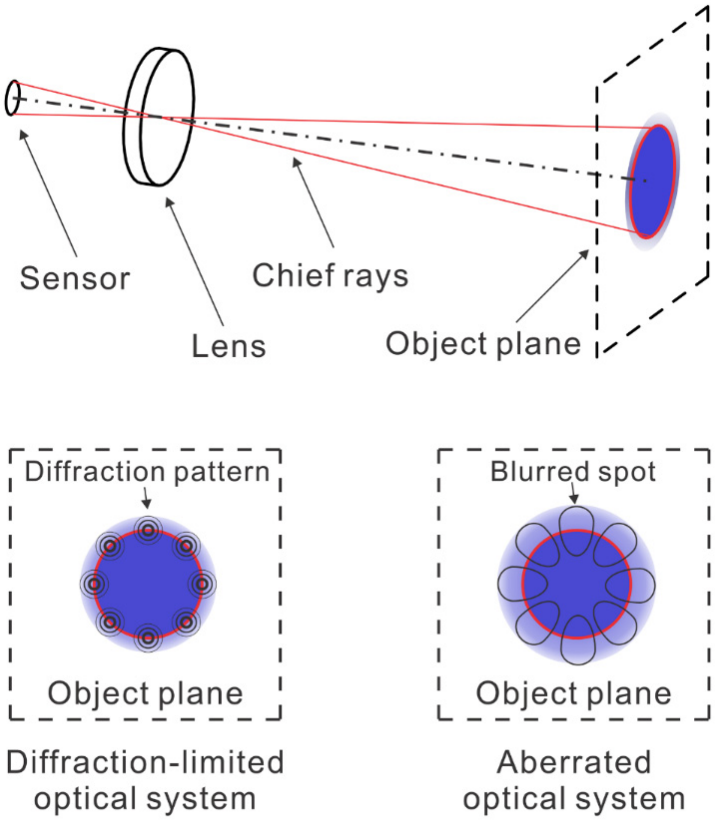

Figure 2.10 Schematic diagram of the measurement area of single-point radiation thermometer.

For a radiation thermometer equipping a FPA detector, the measurement area of each pixel is different due to the existence of optical aberrations. Some aberrations depend upon the optical field-of-view, such as the coma and astigmatism, which leads to the unpredictable shape of the measurement area for each pixel. The non-uniform of measurement area from the centre to the full FOV generates great challenges to undertake reliable measurements, which requires careful calibrations and corrections.

The blurred region around the measurement area can be characterised by the size of source effect, which describes the phenomenon that a radiometer receives radiation from the region outside the nominal measurement area. It arises as a consequence of optical aberrations, diffractions, and reflections and scatterings between lens interfaces [13]. SSE can be characterised using direct [14], indirect [15], and scanning methods [16].The direct method can be expressed as

$$\sigma_{SSE}(r, r_{max}) = \frac{S(r,\ L)}{S(r_{max},\ L)} \tag{2.98}$$

where r is the radius of the aperture, r_{max} is the size of the maximum aperture, L is the working distance, $S(r, L)$ is the signal at the radius r, and $S(r_{max}, L)$ is the signal at the maximum aperture.

2.5 Emissivity enhancement by gold-cup method

Gold-cup method has been widely used for fast temperature measurements since 1951 by enhancing the emissivity of an object [17]. In general, radiation thermometers are calibrated against the radiance temperature of an approximate blackbody furnace. Users need to know the surface emissivity of the object of interest to calculate its true temperature. If the emissivity of a measurement can be enhanced to approximate 1, temperature measurements become emissivity independent of the measurement area, which is ideal for the unknown emissivity materials. Figure 2.11 shows the schematic diagram for using the gold-cup method to measure the temperature of an object. A fibre optic thermometer is mounted on top of a hemispherical metal cup through a small hole. The internal surface of the cup is coated by gold which performs as a reflector. When measuring the temperature of a hot object, the gold-cup is attached to its surface quickly. At that moment, the radiation emitted from the measurand surface is reflected by the gold-cup back to the measurand itself. Then the reflected radiation is either absorbed or reflected by the measurand surface. Multi-reflection occurs between the gold-cup internal surface and the measurand surface until all radiation is absorbed, and thereafter, the emissivity of the measurement area is enhanced.

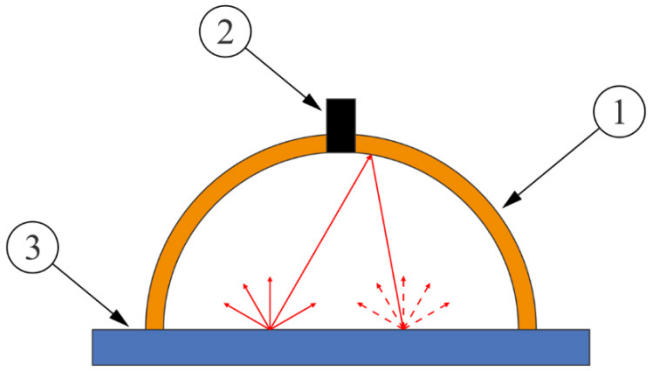

Figure 2.11 Schematic diagram of the gold-cup method: gold-cup (1); radiation thermometer (2); measurand (3).

If the measurand surface is a Lambertian surface (or approximate Lambertian surface), the enhanced effective emissivity can be calculated by

$$\varepsilon_{eff}(\lambda,T)=\frac{\varepsilon_s(\lambda,T)}{1-\rho_{cup}(\lambda,T)\rho_s(\lambda,T)} \tag{2.99}$$

where ε_s is the emissivity of the measurand surface, $\rho_{cup}\approx 0.96$ is the reflectivity of the gold coated surface at the waveband of 0.7 to 10 μm, and ρ_s is the reflectivity of the measurand surface.

Table 2.1 shows the relationship between the emissivity of objects and the enhanced effective emissivity by suing the gold-cup method. If the emissivity of an object is greater than 0.5, the effective emissivity can be enhanced to above 0.96 which can meet the assumption of the emissivity independent temperature measurement. However, the error of measurements cannot be omitted for an object whose emissivity is lower than 0.5. In practice, the surface property for most metal surfaces can be regarded as an approximate Lambertian surface, which agrees with the criteria for using the gold-cup method. For objects with specular surfaces, measurements are also dependent on the field-of-view of fibre optics thermometers, which should be analysed separately.

Surface emissivity	Enhanced effective emissivity
0.0	0.000
0.1	0.7353
0.2	0.8621
0.3	0.9146
0.4	0.9434
0.5	0.9615
0.6	0.9740
0.7	0.9831
0.8	0.9901
0.9	0.9956
1	1.0000

Table 2.1 Relationship between the emissivity of objects and effective emissivity enhanced by the gold-cup method (The object surface is assumed to be Lambertian surface.)

References

[1] M. F. Modest, *Radiative heat transfer*: Academic press, 2013.

[2] P. Saunders, *Radiation Thermometry: Fundamentals and Applications in the Petrochemical Industry*, USA: SPIE Press, 2007.

[3] G. Kirchhoff, "On the relation between the radiating and absorbing powers of different bodies for light and heat," *The London, Edinburgh, and Dublin Philosophical Magazine and Journal of Science,* vol. 20, no. 130, pp. 1-21, 1860.

[4] J. R. Howell, and R. Siegel, *Thermal radiation heat transfer*, 3rd ed., New York: Hemisphere Publishing Co., 1992.

[5] M. Planck, "Zur theorie des gesetzes der energieverteilung im normalspectrum," *Verhandl. Dtsc. Phys. Ges.,* vol. 2, pp. 237, 1900.

[6] F. P. Incropera *et al.*, *Fundamentals of heat and mass transfer*: Wiley, 2007.

[7] M. Bass *et al.*, *Handbook of optics, Volume II: Design, fabrication and testing, sources and detectors, radiometry and photometry*: McGraw-Hill, Inc., 2009.

[8] M. Born, E. Wolf, and A. B. Bhatia, *Principles of Optics: Electromagnetic Theory of Propagation, Interference and Diffraction of Light*: Cambridge University Press, 2000.

[9] M. Bass *et al.*, *Handbook of Optics, Third Edition Volume I: Geometrical and Physical Optics, Polarized Light, Components and Instruments(set)*: McGraw-Hill, Inc., 2010.

[10] J. W. Goodman, *Introduction to Fourier optics*: Roberts and Company Publishers, 2005.

[11] R. R. Corwin, and A. Rodenburgh, "Temperature error in radiation thermometry caused by emissivity and reflectance measurement error," *Applied optics,* vol. 33, no. 10, pp. 1950-1957, 1994.

[12] The British Standards Institution, "Determination of the technical data for radiation thermometers (IEC/TS 62492-2:2013)," *Industrial process control devices - Radiation thermometers*, BSI Standards Limited, 2013.

[13] H. W. Yoon, D. W. Allen, and R. D. Saunders, "Methods to reduce the size-of-source effect in radiometers," *Metrologia,* vol. 42, no. 2, pp. 89-96, 2005.

[14] T. P. Jones, and J. Tapping, "A Precision Photoelectric Pyrometer for the Realization of the IPTS-68 above 1064.43 °C," *Metrologia,* vol. 18, no. 1, pp. 23-31, 1982.

[15] T. Ricolfi, and L. Wang, "Experiments and remarks on the size-of-source effect in precision radiation thermometry," in *Procceedings of TEMPMEKO*, 1993, pp. 161-165.

[16] P. Saunders, and H. Edgar, "On the characterization and correction of the size-of-source effect in radiation thermometers," *Metrologia,* vol. 46, no. 1, pp. 62-74, 2009.

[17] M. D. Drury, K. P. Perry, and T. Land, "Pyrometers for surface-temperature measurement," *Journal of the Iron and Steel Institute,* vol. 169, no. 3, pp. 245-250, 1951.

Chapter 3. Existing experimental techniques to emissivity measurement

In radiation thermometry, emissivity is determined by temperature, wavelength, viewing direction, and surface conditions. Emissivity can be classified as spectral-, total-, directional-, and hemispherical emissivity, all of which require different methods for measurements. The emissivity measurement instruments can be classified into two categories: the direct and indirect methods [1, 2]. The direct method aims to measure the radiation emitted from a measurand and compare it with a theoretical reference to calculate emissivity. The indirect method aims to obtain absorptivity, reflectivity, and transmissivity first and thereafter compute emissivity by applying Kirchhoff's law, as discussed in Section 2.2.3. For the direct methods, emissivity can be characterised by steady-state or transient measurements. Figure 1.1 shows a possible classification of emissivity measurement methods.

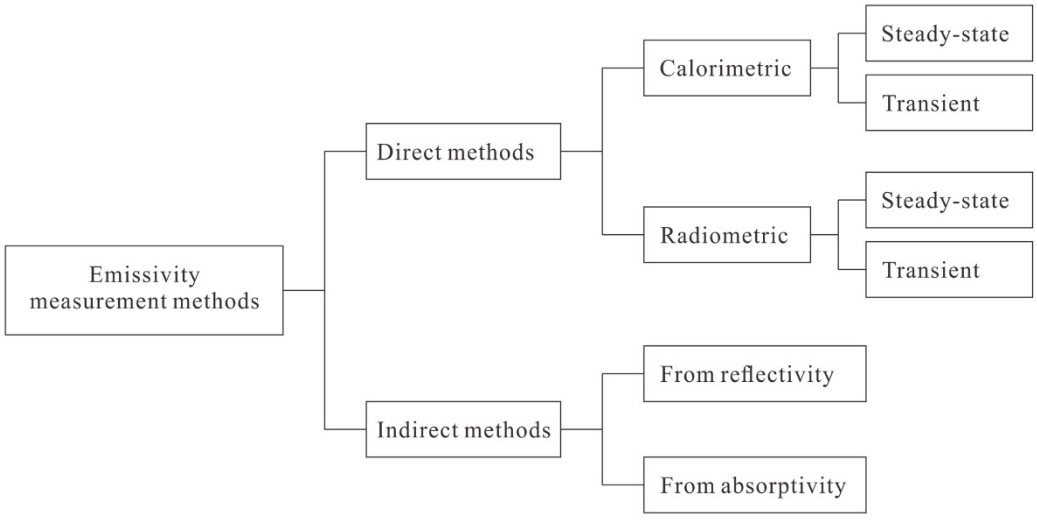

Figure 3.1 Emissivity measurement methods.

3.1 Direct methods

3.1.1 Calorimetric methods

The calorimetric method is used to determine the total hemispherical emissivity by measuring the net radiative heat exchange between a sample and the environment. Figure 3.2 shows the schematic diagram of a typical calorimetric experimental apparatus [3]. During measurement, the sample is suspended in a vacuum chamber coated with a high-emissivity paint. At least two thermocouples are used to measure the temperature of the sample and the wall of the chamber. If the sample is conductive, it is heated by passing a current through itself. Otherwise, the sample is heated by attaching it to a metal substrate which is electrically heated. When the sample is heated to the specified temperature, its emissivity can be measured by steady-state or transient methods.

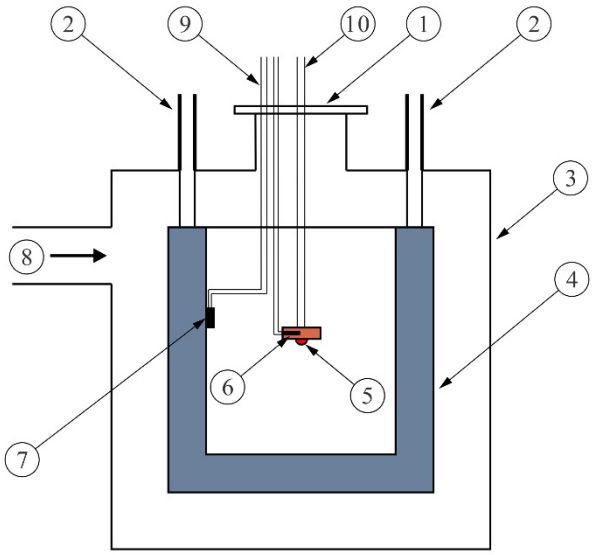

Figure 3.2 Typical setup for calorimetric emission measurements: vacuum feed-through flange (1); coolant fill and vent tubes (2); stainless steel vacuum jacket (3); chamber walls (4); sample and heating plate (5); sample thermocouple (6); wall thermocouple (7); vacuum inlet (8); thermocouple leads (9); power leads (10).

For the steady-state method, the sample is heated and kept at the desired temperature. After the sample has arrived at thermal equilibrium, the current flowing through the heating element and the temperature of the chamber wall are measured. The total hemispherical emissivity can be computed by comparing the electric heat input to the

heating element with the radiative heat exchange between the sample and its surroundings, expressed as

$$\varepsilon(T) = \frac{{I_h}^2 R_h}{A_s \sigma (T_s^4 - T_{wall}^4)} \tag{3.1}$$

where I_h is the current passing the heating element, R_h is the resistance of the heating element, A_s is the exposed surface area of the specimen, σ is the Stefan–Boltzmann constant, T_s is the temperature of the sample, and T_{wall} is the temperature of the chamber wall.

For the transient method, the current is switched off after the specified temperature has reached. The rate of temperature drop of the sample is monitored to compute the total hemispherical emissivity, expressed as

$$\varepsilon(T) = -\frac{m_s C_s \, dT_s/dt}{A_s \sigma (T_s^4 - T_{wall}^4)} \tag{3.2}$$

where m_s is the mass of the sample, and C_s is specific heat capacity of the sample.

The accuracy of measurements depends on the quantification of net-heat transfer between the sample and the environment. To avoid temperature fluctuation of chamber walls, the whole chamber is usually cooled to a low temperature. In contrast, the chamber walls are not ideal absorbers and are not perfect diffusers, which leads to the overestimation of net-heat transfer. The surface emissivity and roughness should be taken into account for the calculation of emissivity to minimise the measurement uncertainty.

3.1.2 Radiometric methods

The radiometric method is generally used to determine the directional emissivity by comparing the radiation from a sample with that from a blackbody under the same conditions. The radiometric method also includes the steady-state and transient methods for emissivity measurements. For the steady-state method, a typical experimental apparatus employs a blackbody furnace, sample furnace, radiation thermometer, and optical components. Figure 3.3(a) shows the schematic diagram of a radiometric experimental apparatus [4]. A blackbody furnace and a sample furnace are equipped on a moveable bench, which allows them to be moved to the measurement position. Both

the blackbody cavity and the sample are heated to the identical temperature of interest, and the radiant flux emitted from them is measured separately. During measurements, the blackbody furnace and the sample furnace should be positioned precisely to maintain identical viewing conditions. Instead of moving the furnaces, a rotary mirror can be used to select the radiation source for measurements, as shown in Figure 3.3(b).

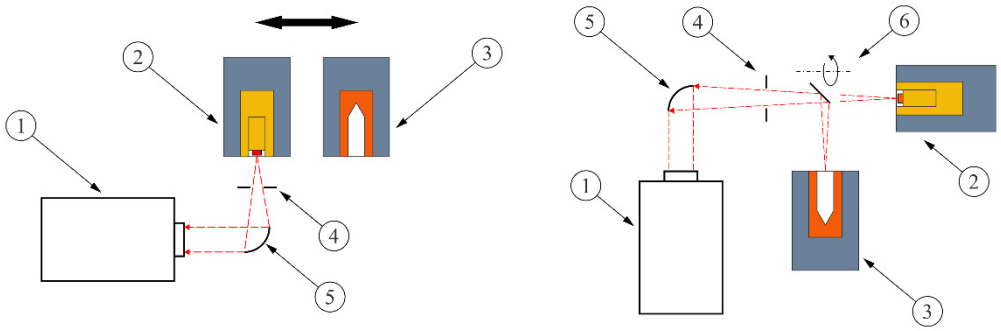

Figure 3.3 Schematic diagram of radiometric experimental apparatuses: (a) method of moving furnaces and (b) method of equipping a rotary mirror. These apparatuses include an FTIR spectrometer (1); sample furnace (2); blackbody cavity furnace (3); aperture (4); mirror (5); rotary mirror (6).

In practice, the measured signal for the blackbody cavity, $S_b(T_b,\lambda)$, also includes the background radiation, given by

$$S_b(T_b,\lambda) = R(\lambda)\left[L_{b,\lambda}(T_b,\lambda) + L_{BG}(\lambda)\right] \tag{3.3}$$

where T_b is the temperature of the blackbody, λ is the wavelength, $R(\lambda)$ is the responsivity of the apparatus, $L_b(T_b,\lambda)$ is the blackbody radiance, and $L_{BG}(\lambda)$ is the radiance due to background radiation.

The measured signal for the sample, $S_s(T_s,\lambda)$, also includes the radiation emitted by its surroundings and, thereafter, reflected by the sample surface to the detector as well as the background radiation, which can be expressed as

$$\begin{aligned} &S_s(T_s,\lambda) = \\ &R(\lambda)\left[\varepsilon_s(T_s,\lambda)L_{b,\lambda}(T_s,\lambda) + \rho_s(T_s,\lambda)\varepsilon_{sur}(T_{sur},\lambda)L_{b,\lambda}(T_{sur},\lambda) + L_{BG}(\lambda)\right] \end{aligned} \tag{3.4}$$

where T_s is the temperature of the sample, $\varepsilon_s(T_s,\lambda)$ is the sample emissivity, $\rho_s(T_s,\lambda) = 1-\varepsilon_s(T_s,\lambda)$ is the sample reflectivity, $\varepsilon_{sur}(T_{sur},\lambda)$ is the emissivity of sample

surroundings, and T_{sur} is the temperature of the sample surroundings. Only one-reflection between the sample and its surroundings is considered in this equation.

In Equations (3.3) and (3.4), the responsivity and background radiation are difficult to be quantified. These two unknown quantities can be omitted if the blackbody radiation is measured at another temperature and, thereafter, the sample emissivity can be obtained by [5]

$$\varepsilon_s(T_s,\lambda) = \frac{S_s - S_{b2}}{S_{b1} - S_{b2}} \cdot \frac{L(T_{b1}) - L(T_{b2})}{L(T_s) - \varepsilon_{sur} L(T_{sur})} + \frac{L(T_{b2}) - \varepsilon_{sur} L(T_{sur})}{L(T_s) - \varepsilon_{sur} L(T_{sur})} \tag{3.5}$$

where subscripts "$b1$" and "$b2$" denote the first and second blackbody radiance temperatures for measurements, respectively.

Great efforts have been spent on the development of high-accuracy emissivity measurement instruments based on direct methods. Hanssen et al. introduced their facility for spectral emissivity measurements at NIST in 2004 [6]. The facility at the first stage covered a wavelength range from 1 μm to 20 μm, temperatures from 600 to 1400 K, and angles from 0° to > 75°. The latest report updated that the facility had been extended to the temperature range of 473 to 1400 K and wavelengths up to 50 μm [7]. Monte et al. introduced their facility for measuring thermal radiation at PTB to provide traceable spectral emissivity measurements without atmospheric interference [8, 9, 10]. Under sealed vacuum conditions, the facility can perform directional spectral emissivity measurements in the temperature range from 0 to 430 °C, wavelengths from 1 μm to 1000 μm, and angles from 0° to ± 70°.

Compared with the case employing a separate blackbody as the reference source, another possible method is to integrate the sample and blackbody cavity to perform measurements. Figure 3.4 shows a schematic diagram of the experimental setup using an integrated blackbody method, as proposed by M. A. Postlethwait *et al*. [11]. A sample is placed at the bottom of a deep isothermal furnace tube. Both the sample and the furnace are heated to a high temperature and, thereafter, they act as an approximate blackbody cavity due to the multiple reflections between the tube walls and the sample. After recording the signal from the approximate blackbody, a cold tube is dropped into the furnace tube to block the background radiation. Then, the measured signal can be regarded as the free radiation from the sample surface.

If the measurement is undertaken quickly, the thermal interference to the sample can be omitted by inserting the cold tube. The directional emissivity of the sample is given by

$$\varepsilon_s(T,\lambda) = \frac{S_s(T,\lambda)}{S_b(T,\lambda)} \cdot \varepsilon_{eff}(T,\lambda) \tag{3.6}$$

where $\varepsilon_{eff}(T,\lambda)$ is the effective emissivity of the approximate blackbody formed by the furnace tube and the sample.

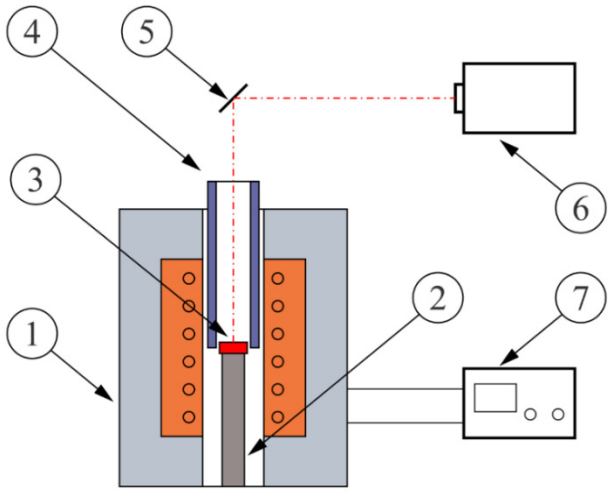

Figure 3.4 Schematic diagram of an emissivity measurement apparatus applying the drop-tube method: furnace (1); SiC supporter (2); sample (3); drop tube (4); mirror (5); FTIR spectrometer (6); temperature controller (7).

Two factors should be pre-investigated by applying this method. The first is to evaluate the temperature change rate of the sample after dropping a cold tube to determine the measurement period. The second is to estimate the effective emissivity of the formed cavity. For high emissivity materials, the formed cavity can be assumed to an approximate blackbody cavity. Otherwise, the effective emissivity should be analysed to compensate for the enhanced cavity radiance.

For the transient method, a typical experimental apparatus usually is composed of a furnace, laser module, thermocouple, and radiation thermometer. Figure 3.5 shows a schematic diagram of a typical transient radiometric measurement facility employing the laser flash technique [12]. The sample is pre-heated in a furnace to the desired temperature and then irradiated by the laser beam to a higher temperature. The

temperature rise is measured by a thermocouple buried within the sample during the measurement.

If the heat capacity of the sample and absorbed energy due to the laser irradiation are known, the directional emissivity can be obtained by

$$\varepsilon(T,\lambda) = -\frac{m_s C_s}{Q_\lambda}\Delta T \tag{3.7}$$

where Q_λ is the absorbed energy due to laser irradiation, and ΔT is the rate of temperature change.

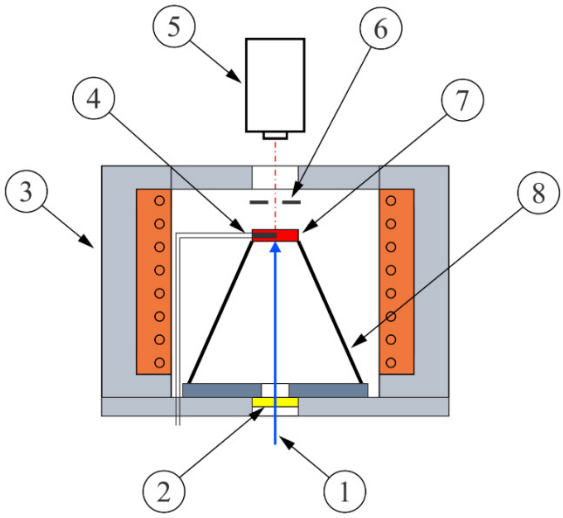

Figure 3.5 Schematic diagram of the transient emissivity measurement facility: laser beam (1); window (2); furnace (3); thermocouple (4); FTIR spectrometer (5); aperture (6); sample (7); sample holder (8).

More radiometric measurement techniques have been previously described by [13, 4].

3.2 Indirect methods

The indirect method measures absorptivity, reflectivity, and transmissivity of a sample and then computes the emissivity using Kirchhoff's law. If the sample is opaque, only the reflection properties are required to obtain emission properties. With different measurement specifications, reflection measurement methods are generally used to determine the directional-hemispherical reflectivity, hemispherical-directional reflectivity, or bidirectional reflectivity. Compared with the direct method which requires

a high measurement temperature to allow the self-emission of a sample, the indirect method can achieve an accurate measurement at low temperature conditions or for low emissivity materials. This is a benefit for relatively strong input signals with respect to the electronic noise of the measurement instrument.

For measuring hemispherical reflectivity, a classic instrument is composed of an integrating sphere, detectors, light sources, baffles, and mirrors [4]. If a sample is illuminated by an external light source directly, as shown in Figure 3.6(a), the reflected energy is diffused by the multi-reflection within an integrating sphere. The signal of diffused radiation is then recorded by a detector. When the sample is removed and replaced with a standard plate, the measured signal is considered as the reference value. The directional hemispherical reflectivity (DHR) can be computed by taking the ratio of the signal of the sample to that of the standard plate. If a sample is illuminated by the light reflected by an integrating sphere, the hemispherical directional reflectivity (HDR) can be measured, as shown in Figure 3.6(b). When an integrating sphere is used for undertaking reflectivity measurements, the temperature of interest cannot achieve a high range because of technical difficulties such as the heating method of samples and the thermal performance of integrating sphere coating. Once the spectral hemispherical reflectivity is measured, the spectral hemispherical emissivity can be obtained by Equation (2.48).

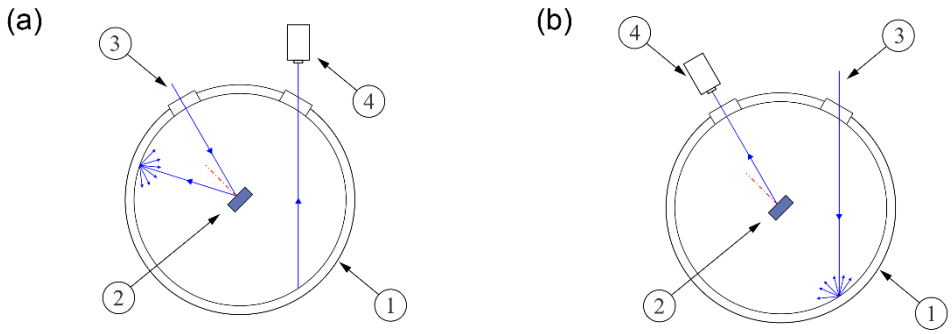

Figure 3.6 Classic integrating sphere reflectometer: (a) DHR mode, (b) HDR mode. The device includes: integrating sphere (1); sample (2); illumination light source (3); detector (4).

Spectral bidirectional reflectivity is dependent on the polar and azimuth angles, which require the instrument to characterise the reflected radiation in both directions. Figure 3.7 shows a typical bidirectional reflectivity measurement instrument. The instrument consists of a tunable laser module, a radiation detector, hot plate, and moveable brackets. The sample is illuminated by a laser beam at the desired incident angle. The reflected

radiation is measured by the detector, which can scan the whole hemispherical space. The spectral bidirectional reflectivity can be profiled by taking the ratio of the signal for the radiant flux reflected by the sample to the incident radiant flux and, therefore, the spectral directional emissivity can be obtained by Equation (2.46).

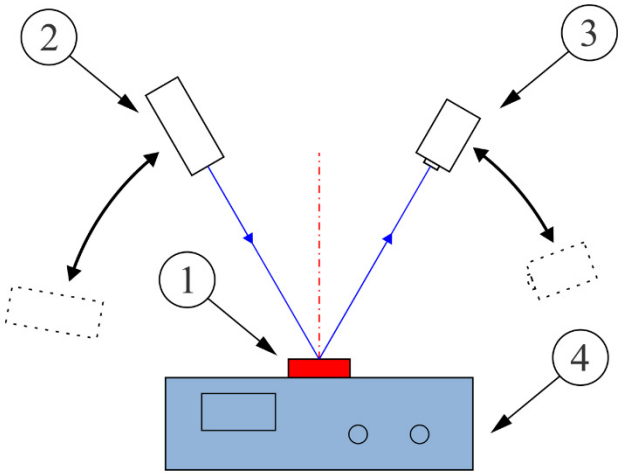

Figure 3.7 Schematic diagram of a typical bidirectional reflectivity measurement instrument: sample (1); illumination source (2); detector (3); hotplate (4).

References

[1] D. P. DeWitt, and G. D. Nutter, *Theory and practice of radiation thermometry*: John Wiley & Sons, 1988.

[2] M. F. Modest, *Radiative heat transfer*: Academic press, 2013.

[3] J. Hameury, B. Hay, and J. Filtz, "Measurement of total hemispherical emissivity using a calorimetric technique," *Int. J. Thermophys.,* vol. 28, no. 5, pp. 1607-1620, 2007.

[4] M. Honner, and P. Honnerová, "Survey of emissivity measurement by radiometric methods," *Appl. Opt.,* vol. 54, no. 4, pp. 669-683, 2015.

[5] L. del Campo *et al.*, "New experimental device for infrared spectral directional emissivity measurements in a controlled environment," *Rev. Sci. Instrum.,* vol. 77, no. 11, pp. 113111, 2006.

[6] L. M. Hanssen, S. N. Mekhontsev, and V. B. Khromchenko, "Infrared spectral emissivity characterization facility at NIST," in *Thermosense XXVI*, 2004, pp. 1-12.

[7] B. Wilthan, L. M. Hanssen, and S. Mekhontsev, "Measurements of infrared spectral directional emittance at NIST-A status update," in *AIP Conference Proceedings*, 2013, pp. 746-751.

[8] C. Monte *et al.*, "Radiation thermometry and emissivity measurements under vacuum at the PTB," *Int. J. Thermophys.,* vol. 30, no. 1, pp. 203, 2009.

[9] R. Taubert *et al.*, "Traceable calibration of radiation sources from the visible to the far infrared for space borne applications at PTB," in *Proc. SPIE Sensors, Systems, and Next-Generation Satellites XIII*, 2009, pp. 747413.

[10] A. Adibekyan *et al.*, "The development of emissivity measurements under vacuum at the PTB," *Meas. Tech.,* vol. 55, no. 10, pp. 1163-1171, 2013.

[11] M. A. Postlethwait *et al.*, "High-temperature, normal spectral emittance of silicon carbide based materials," *J Thermophys Heat Tr,* vol. 8, no. 3, pp. 412-418, 1994.

[12] S. Krenek *et al.*, "A dynamic method to measure emissivity at high temperatures," *Int. J. Thermophys.,* vol. 36, no. 8, pp. 1713-1725, 2015.

[13] P. Saunders, *Radiation thermometry: fundamentals and applications in the petrochemical industry*: SPIE press, 2007.

Chapter 4. Evaluation of emissivity measurements by direct and indirect methods

4.1 Introduction

Emissivity can be considered as the efficiency factor of thermal radiation emitted from the surface of an object. At present, emissivity is primarily measured by experimental methods that require accurate and traceable measurement instruments, as discussed in Section 1.4.2 [1, 2, 3]. Instruments for emissivity measurements can be classified into the direct and indirect measurement methods. Each method has its own inherent advantages and disadvantages, which therefore dictates the most suitable emissivity measurement range for each technique [4, 5]. The boundary of the most suitable measurement range has not been systematically studied between the direct and indirect methods so far. Furthermore, the uncertainty budgets of instruments are important to be understood for comparing the measurement accuracy quantitatively between different methods.

This chapter introduces the development of an instrument for the measurement of emissivity which can offer three different measurement methods: direct, indirect, and in situ direct methods. The instrument consists of a pair of hemispherical cups, coated with gold and Vantablack®. Measurements were performed at temperatures ranging from 200 to 450 °C, operating over a spectral range of 2.1 to 2.5 μm. The uncertainties within each method were assessed in order to determine the most suitable emissivity measurement range for different materials. At last, three commonly used materials [stainless steel 304 (SS304), aluminium alloy 6082 (Al6082), and the high emissivity paint HiE-Coat 840M] were measured to evaluate the performance of the instrument.

4.2 Experimental setup

The instrument was composed of a Vantablack® coated cup (black-cup), gold coated cup (gold-cup), custom designed radiation thermometer, hot plate (SCILOGEX MS7-H550-Pro), and data acquisition system. The schematic diagram of the instrument is shown in Figure 4.1. For each measurement, a sample was loaded on the central area of a hot plate positioned upon an optical bench. A thermocouple (TC Direct 408-053 Class-1) was inserted into a hole drilled into the sample to measure its temperature. This hole was 1.5 mm in diameter and 2 mm beneath the top surface. The black and gold cups were mounted upon a movable plate above the sample, assembling as a gold-black-cup unit. A 2 mm diameter hole was drilled at the top of each cup to allow the radiation emitted from the sample to pass through. The radiation thermometer, which was fixed at the top of the instrument, was focused onto the position of the hole in order to receive the emitted radiation. The output signal of the thermometer was recorded by the data acquisition system.

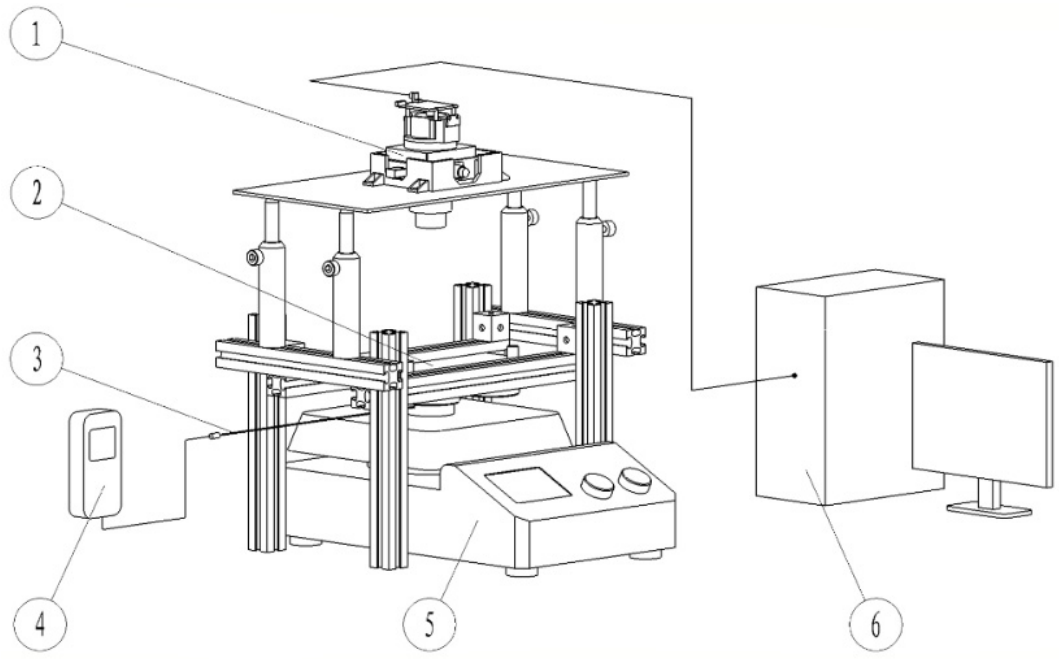

Figure 4.1 Schematic diagram of construction of the emissivity measurement instrument. Custom designed radiation thermometer (1); gold-black-cup unit (2); thermocouple (3); thermometer readout module, Fluke T3000 FC (4); hot plate (5); data acquisition system (6).

The gold-black-cup unit was placed between a sample and the radiation thermometer, as shown in Figure 4.2. Each cup was made of Aluminium 6061 and fabricated to be identical in shape, as shown in Figure 4.3. The internal surface of each cup was a half-sphere in shape, with a curvature of 20 mm in radius. The internal surface of the gold-cup was electroplated with a thin layer of Nickel, mirror polished and coated with gold by Laser Beam Products Ltd., to reflect the radiation emitted from a sample, leading to the emissivity enhancement. The internal surface of the black-cup was sand-blasted and coated with Vantablack®-S-VIS (Surrey NanoSystems Ltd.) to block the background radiation from the hot plate, thereby acting as a radiation shield. The gold-black-cup unit can be slid along the optical rail between position A and B, allowing either the gold-cup or the black-cup to be positioned above a sample for its respective measurement.

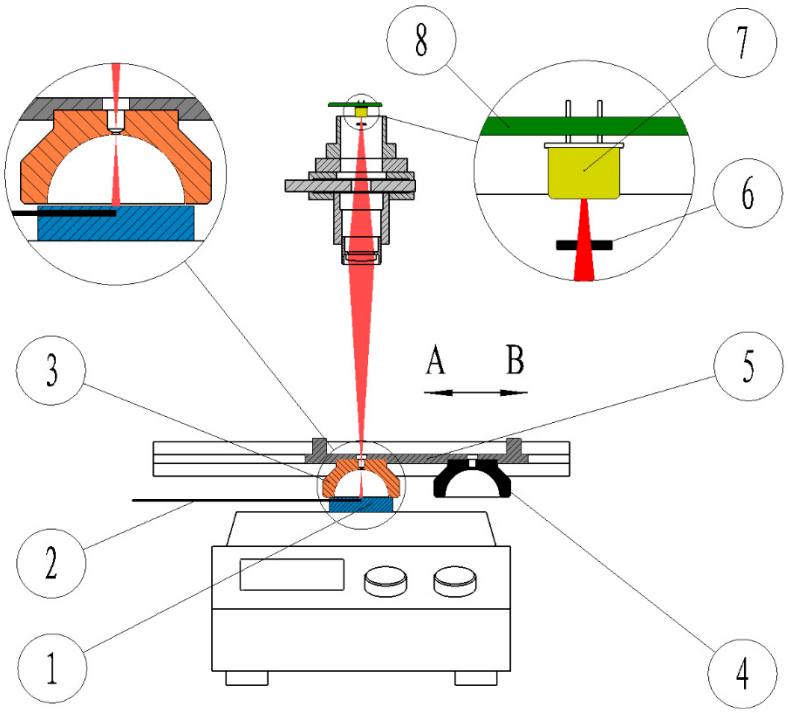

Figure 4.2 Schematic cross-section diagram of the emissivity measurement instrument. Sample (1); thermocouple (2); gold-cup (3); black-cup (4); movable plate (5); bandpass filter, 2.1 to 2.5 μm (6); Extended InGaAs photodiode (7); PCB (8).

Figure 4.3 Photo of the gold-cup and the black-cup mounted on a movable plate.

The radiation thermometer consisted of a 60 mm focal length singlet lens (Edmund Optics 45-127), a bandpass filter (2.1-2.5 μm), an extended indium gallium arsenide (Ex-InGaAs) photodiode (Hamamatsu G12183-010K), and a custom designed amplifier circuit upon a printed circuit board (PCB). The thermometer was designed as a common-path optical system with a red laser (650 nm) and the photodiode. The laser beam was used to align the focus position before each measurement. After alignment, the laser was powered off and the thermometer was changed to its radiation measurement mode. The parameters of the radiometer are listed in Table 4.1. The working distance is defined as the distance from the singlet surface to the top of the internal surface of each cup. The spot size was simulated by Zemax OpticStudio with the consideration of aberrations. The radiation thermometer was pre-calibrated with a blackbody furnace (LANDCAL P550P) from 200 to 450 °C at a working distance of 150 mm. The calibration data was stored as reference values for later emissivity measurements. The spectral responsivity of the radiation thermometer is shown in Figure 4.4.

Parameter	**Result**
Wavelength	2.1 to 2.5 μm
Focal length	60 mm
F-number	3.0
NA	0.167
Working distance	150 mm
Field stop	0.5 mm in diameter
Field-of-view/DTR (design)	80:1
Spot size at working distance (design)	1.875 mm in diameter

Table 4.1 Parameters of the radiation thermometer

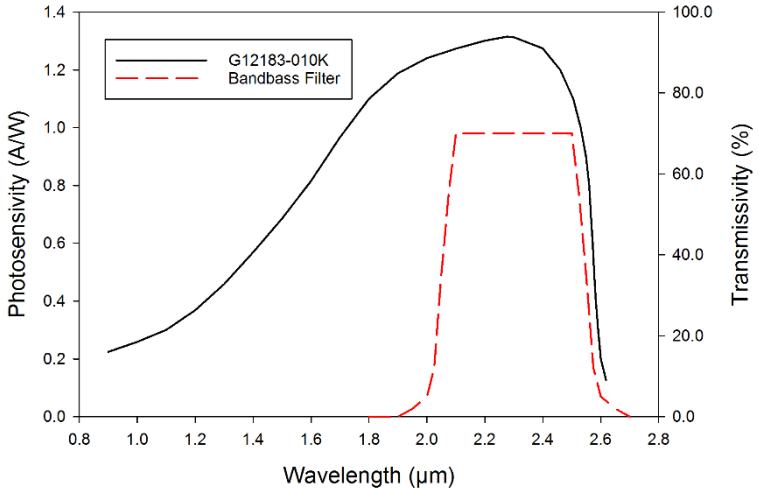

Figure 4.4 Spectral responsivity of the radiation thermometer. The left axis represents the photosensitivity of the Ex-InGaAs photodiode. The right axis represents the transmissivity of the bandpass filter.

4.3 Methodology and measurement procedures

This instrument was designed with the intention of measuring emissivity using three methods: the black-cup method, the gold-cup method, and the dual-cup method. The black-cup method is a direct emissivity measurement method. The normal emissivity is computed by measuring radiant power emitted from a sample when it is covered by the black-cup compared to that from a blackbody. The gold-cup method is an indirect measurement method. The enhanced effective emissivity of a sample is measured when it is covered by the gold-cup for computing the sample original emissivity. The dual-cup method is characterised as an in situ direct measurement method. By using this method, the normal emissivity is computed using the ratio of radiant power from a sample when it is covered by the black-cup to that when it is covered by the gold-cup. This method does not require the pre-measured data of a blackbody furnace, unlike the other two methods. In this work, emissivity is classified to low emissivity range (emissivity < 0.3), middle emissivity range (0.3 $\leqslant$ emissivity < 0.7), and high emissivity range (0.7 $\leqslant$ emissivity $\leqslant$ 1), which will simplify the discussion between different measurement methods.

4.3.1 Black-cup method

The black-cup method computes the ratio of radiant power emitted from a sample to that from a blackbody at the same temperature, wavelength, and viewing condition [6]. The radiant power from a blackbody furnace has been pre-measured from 200 to 450 °C, with temperature steps of 50 °C. When the sample is heated to the calibration temperature, the normal emissivity of a sample, $\varepsilon_s(\lambda, T)$, can be derived from Equation (2.18).

$$\varepsilon_s(\lambda, T) = \frac{L_s(\lambda, T)}{L_b(\lambda, T)} \tag{4.1}$$

where λ is the wavelength, T is the temperature, $L_s(\lambda, T)$ is the radiance from a sample, and $L_b(\lambda, T)$ is the radiance from a blackbody. The spectral radiance of a blackbody, $L_b(\lambda, T)$, can be expressed by Equation (2.10).

In practice, a radiation thermometer receives radiation not only from the sample, but also from its surroundings due to reflection and scattering. For example, radiation emitted from the hot plate may reflect onto the sample surface, leading to the enhancement of measured emissivity. The measured emissivity, $\varepsilon_{meas}(\lambda, T)$, can be described as

$$\varepsilon_{meas}(\lambda, T) = \frac{L_s(\lambda, T) + L_{sur}(\lambda, T)}{L_b(\lambda, T)} \tag{4.2}$$

where $L_{sur}(\lambda, T)$ is the radiance from the surroundings.

To block the background radiation, a cold black-cup is used to cover the sample surface during the measurement. If the measurement is taken quickly, the temperature change of a sample and the black-cup can be omitted. The measured emissivity thereby can represent the sample emissivity.

$$\varepsilon_s(\lambda, T) \approx \varepsilon_{meas}(\lambda, T) = \frac{L_{bc}(\lambda, T)}{L_b(\lambda, T)} \tag{4.3}$$

where $L_{bc}(\lambda, T)$ is the radiance from a sample covered by the black-cup.

4.3.2 Gold-cup method

The gold-cup method is used for fast temperature measurements of objects without prior knowledge of their surface emissivities [7]. Herein, a gold-cup is applied to enhance the

radiative property of a sample. This kind of enhancement is beneficial for the measurement of low emissivity materials, which will be discussed in detail further on.

The gold-cup method takes three steps to obtain the emissivity of a sample. The first step is to measure the enhanced radiant power from the sample when it is covered by the gold-cup. The second step is to compute the enhanced effective emissivity by taking the ratio of the measured radiant power from the sample to that from a blackbody at the same temperature. Once the relationship between the sample emissivity and its enhanced emissivity is known, the true emissivity of the sample can be computed as the last step.

When a sample is covered by the gold-cup, the sample and the cup form an approximate cavity. The radiation emitted from the sample surface is multi-reflected within the internal surface of the cavity and, thereafter, the effective emissivity is enhanced, as introduced in Section 2.5 [4]. The relationship between the sample emissivity and the enhanced effective emissivity is dependent upon the reflection properties of the sample surface. If the sample surface acts as a Lambertian surface, the surface reflection can be treated as directional-hemispherical reflection. If the sample surface acts as a mirror-like (specular) surface, the reflection is treated as specular reflection. To simplify the discussion, the calculations in this work assume that the sample surface either acts as a Lambertian surface or a purely specular surface. In practice, this assumption can be used to represent the majority of materials [6].

4.3.2.1 Lambertian surface

For a sample with a Lambertian surface, the radiance emitted or reflected from that surface remains constant at any viewing angle [6]. Therefore, the sample surface emits and reflects radiation uniformly to the cup, including the gap and the cup hole. The gold-cup internal surface is assumed to perform as specular reflection. The enhanced effective emissivity measured by the radiation thermometer can be derived from Equation (2.99)

$$\varepsilon_{eff}(\lambda,T)=\frac{\varepsilon_s(\lambda,T)}{1-\rho_{cup}(\lambda,T)\rho_s(\lambda,T)\left[\left(A_{cup}-A_{ho}\right)/\left(A_{cup}+A_{gap}\right)\right]} \tag{4.4}$$

where A_{ho} is the area of the gold-cup hole opening, A_{gap} is the area of the gap between a sample and gold-cup, A_{cup} is the area of the gold-cup internal surface, $\varepsilon_s(\lambda,T)$ is the

emissivity of a sample, $\rho_{cup}(\lambda, T)$ is the reflectivity of the gold-cup internal surface, and $\rho_s(\lambda, T)$ is the reflectivity of a sample.

To simplify the equation, G is defined as the geometrical factor

$$G = \left(A_{cup} - A_{ho}\right)/\left(A_{cup} + A_{gap}\right) \tag{4.5}$$

For an opaque lambertian surface, the relationship between reflectivity and emissivity can be described by Kirchhoff's law under thermal equilibrium, which is $\varepsilon_s(\lambda, T) + \rho_s(\lambda, T) = 1$, as discussed in Section 2.2.3.5 and 2.2.3.6.

Once the enhanced effective emissivity is measured, the sample emissivity can be computed by

$$\varepsilon_s(\lambda, T) = \frac{\varepsilon_{eff}(\lambda, T)\left(1 - \rho_{cup}(\lambda, T)G\right)}{1 - \varepsilon_{eff}(\lambda, T)\rho_{cup}(\lambda, T)G} \tag{4.6}$$

In Equation (4.5), the geometrical factor can be obtained from the shape of the gold-cup. The reflectivity of a polished gold surface is assumed to be 0.96 over the spectral range of 2.1 to 2.5 μm, which is the minimum value from the industry standard [8]. Therefore, the relationship between the enhanced effective emissivity and the sample emissivity is represented by the black line in Figure 4.7. When the emissivity of the sample increases from 0 to approximately 0.3, the effective emissivity is enhanced from 0 to approximately 0.8, respectively. In turn, the enhanced effective emissivity increases from 0.8 to 1 when the sample emissivity increases from approximately 0.3 to 1. The gold-cup method offers a better minimum resolvable emissivity difference for low emissivity materials due to the radiation enhancement and, therefore, improves the signal to noise ratio.

4.3.2.2 Specular surface

For a sample with a specular surface, the reflection on this surface obeys the law of reflection, similar to that on the internal surface of the gold-cup. The multi-reflection within the cavity, formed by the sample and the gold-cup, is dependent upon the incident angle of radiation. Therefore, the relationship described by Equation (4.6) is not valid in this scenario.

A Monte Carlo ray-tracing method can be applied to determine the relationship in this case. For the reflection occurring on a specular surface, the law of reflection states that the incident ray, the reflected ray, and the normal to the surface all lie in the same plane. If a ray emitted by a sample hits the gold-cup internal surface, the reflected ray is always located within the plane defined by the incident ray and normal to the gold-cup internal hemi-spherical surface. Particularly, the incident ray, the reflected ray, the normal line to the sample surface which passes through the emission point, and the normal line to the gold-cup internal surface which passes the incident point all lie in the same plane. Hence, the subsequent reflections all occur within this plane until the ray either is absorbed or escapes from the gold-cup. In this Monte Carlo simulation, all initial rays are generated which obey the uniform distribution. Hence, the simulation can be simplified to a 2D model due to the symmetric property of the gold-cup.

The Monte Carlo simulation of the ray tracing of a gold-cup has not been achieved before. In this work, Matlab is used to undertake this simulation by three steps. Firstly, the Ex-InGaAs photodiode sensor is replaced by an ideal blackbody surface, which randomly emits monochromatic rays into the gold-cup via the cup hole. The rays entering the cavity all fall within the field-of-view of the radiation thermometer. Secondly, the reflection of these rays within the cavity is then traced until all of them have either been absorbed or escaped from the cavity via the gap or the hole. Finally, by tracing large numbers of rays, the spectral absorptivity of a sample can be obtained as

$$\alpha_{eff}(\lambda, T) = N_a / N \tag{4.7}$$

where N_a is the number of rays absorbed by the sample surface, and N is the number of rays entering the cavity.

According to Kirchhoff's law, once the spectral absorptivity of an object is known, then the spectral emissivity under thermal equilibrium can be calculated

$$\varepsilon_{eff}(\lambda, T) = \alpha_{eff}(\lambda, T) \tag{4.8}$$

where $\varepsilon_{eff}(\lambda, T)$ is the enhanced effective emissivity of the assembled cavity.

Figure 4.5 shows a ray that entered the cavity and escaped from the gap after multi-reflections. Figure 4.6 shows the pattern of tracing 10,000 rays, which is an illustration for showing the optical path of each traced ray. The red dots in Figure 4.7 show the

relationship between the sample emissivity and enhanced effective emissivity after tracing 100,000 rays. The data can be fitted by a seventh-order polynomial equation, as shown in Equation (4.9). The parameters and the residual fitting error, represented by root mean square error (RMSE), are shown in Table 4.2.

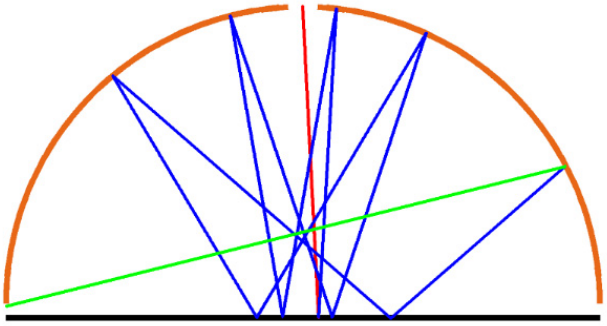

Figure 4.5 The pattern produced by tracing a single ray within the cup. The orange line is the internal surface of the gold-cup. The black line is the top surface of the sample. The red line represents the optical path of a ray entering the cup. The blue lines represent the optical paths of the ray reflecting within the cup. The green line represents the optical path of the ray escaping from the gap.

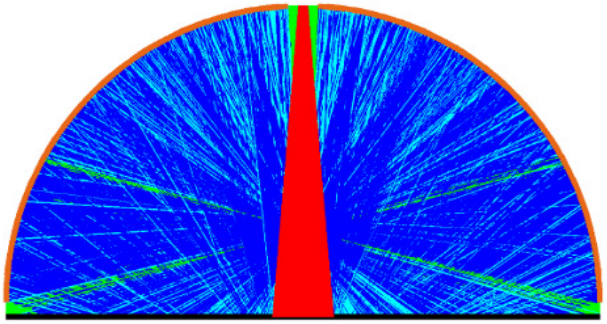

Figure 4.6 The pattern produced by tracing 10,000 rays within the cavity. The red area represents the field-of-view of the radiation thermometer. The blue area represents the internal reflections. The sky-blue area represents the optical paths where rays are finally absorbed.

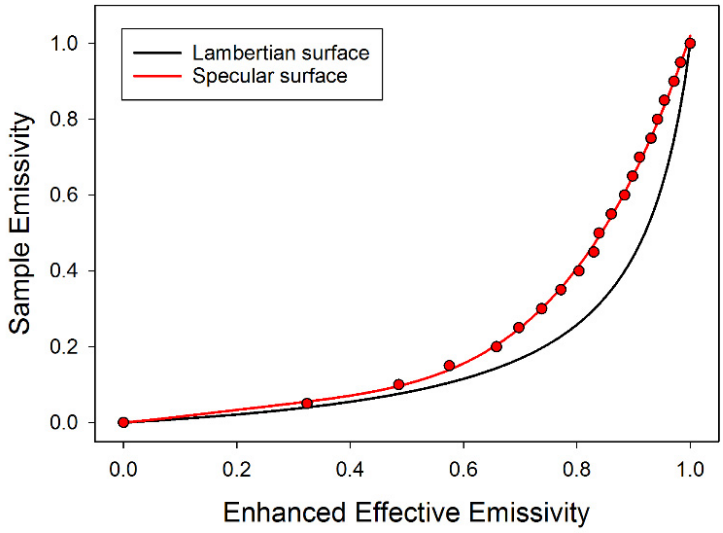

Figure 4.7 Relationship between the sample emissivity and the enhanced effective emissivity. The black line represents the relationship of a Lambertian surface. The red line represents the relationship of a specular surface.

$$\varepsilon_s = P1 \times \varepsilon_{eff}^7 + P2 \times \varepsilon_{eff}^6 + P3 \times \varepsilon_{eff}^5 + P4 \times \varepsilon_{eff}^4 + P5 \times \varepsilon_{eff}^3 + P6 \times \varepsilon_{eff}^2 + P7 \times \varepsilon_{eff} + P8 \quad (4.9)$$

Parameter	Value
P1	−0.7890
P2	1.5989
P3	−0.0423
P4	0.0478
P5	0.0127
P6	0.0696
P7	0.1209
P8	0.0000
RMSE	0.01121

Table 4.2 Parameters of fitting curve for gold-cup method (specular surface)

4.3.3 Dual-cup method

In the previous two methods, the surface temperature of the sample is measured by the embedded thermocouple within the sample. A thermal gradient along the sample vertical direction is inevitable due to the nature of the heating process, which causes the true surface temperature to be lower than the value measured by the thermocouple. This poses a challenge in selecting the reference temperature of the blackbody furnace for the computation of emissivity, thereby increasing the measurement uncertainty.

The dual-cup method can be used to address this problem. Once the relationship between the sample emissivity and enhanced effective emissivity is understood, the assembled cavity can be corrected to be an approximate blackbody. In that case, a sample is both the measurand and reference blackbody source. Equation (4.3) is now turned to

$$\varepsilon_s(\lambda,T) = \frac{L_{bc}(\lambda,T)}{L_{gc}(\lambda,T)} \times \frac{L_{gc}(\lambda,T)}{L_b(\lambda,T)} \tag{4.10}$$

where $L_{bc}(\lambda,T)$ is the radiance from the sample covered by the black-cup, $L_{gc}(\lambda,T)$ is the radiance from the sample covered by the gold-cup, and $L_b(\lambda,T)$ is the radiance from a blackbody furnace.

Equation (4.10) can be rewritten in emissivity form as

$$\varepsilon_s(\lambda,T) = \varepsilon_{dual}(\lambda,T) \times \varepsilon_{eff}(\lambda,T) \tag{4.11}$$

where $\varepsilon_{dual}(\lambda,T)$ is the measured emissivity, which is the ratio of radiant power from a sample covered by the black-cup to that covered by the gold-cup, and $\varepsilon_{eff}(\lambda,T)$ is the enhanced effective emissivity of the cavity formed by a sample and the gold-cup.

By applying the dual-cup method, the enhanced effective emissivity performs as a correction factor which is independent of the measurement temperature. The enhanced effective emissivity can be obtained by Equations (4.4) or (4.9), depending upon the surface reflection properties of the sample.

If a sample acts as a Lambertian surface, the emissivity can be calculated from Equations (4.4) and (4.11), as

$$\varepsilon_s(\lambda,T) = \frac{\varepsilon_{dual}(\lambda,T) + G\rho_{cup}(\lambda,T) - 1}{G\rho_{cup}(\lambda,T)} \tag{4.12}$$

If a sample acts as a specular surface, the emissivity can be obtained by solution of Equation (4.9) and (4.11). For the convenience of calculation, the result can be fitted by a fourth-order polynomial, as shown in Equation (4.13). The parameters and the residual fitting error, represented by RMSE, are shown in Table 4.3.

$$\varepsilon_s = P1 \times \varepsilon_{dual}^4 + P2 \times \varepsilon_{dual}^3 + P3 \times \varepsilon_{dual}^2 + P4 \times \varepsilon_{dual} + P5 \quad (4.13)$$

Parameter	Value
P1	1.4064
P2	−3.2416
P3	2.8000
P4	0.0374
P5	0.0000
RMSE	0.00479

Table 4.3 Parameters of fitting curve for dual-cup method (specular surface)

4.3.4 Measurement procedures

Five sets of samples were prepared and measured, including rough SS304, rough Al6082, polished SS304, polished Al6082, and HiE-Coat 840M paint on an Al6082 substrate. The samples were machined to be 50 mm in diameter by 10 mm in thickness. A 1.5 mm diameter hole was drilled 2 mm from the top surface of the sample for insertion of the thermocouple. The depth of the hole was 25 mm, enabling the thermocouple tip to reach the sample centre. Rough samples were ground by P240 sandpaper. Polished samples were ground by P240, P400, P800 sandpapers and polished to 3 μm by diamond suspensions. These samples were ultrasonically cleaned using isopropyl alcohol. The HiE-Coat 840M painted samples were ground by P240 sandpaper, cleaned by isopropyl alcohol and then brushed by the paint. The thickness of the paint was approximately 0.15 to 0.20 mm. All samples were fully dried and stored in a vacuum box prior to measuring.

The prepared sample was positioned on the centre of the hot plate. The distance between the top surface of the sample to the bottom surface of the cup was adjusted to approximately 1 mm. Once the sample was loaded to the correct position, a thermocouple was inserted into the sample, enabling the commencement of the emissivity measurement.

The hot plate was set to the first temperature point. After the sample had stabilised at the measurement temperature for 30 minutes, the gold-cup was slid to cover the sample to gather the first set of data. The black-cup was then quickly moved to cover the sample to gather the second set of data. The sample temperature was stored for both measurements. This process was repeated with the hot plate set at incremental temperature points until

the whole series of measurements was collected. Figure 4.8 shows a picture of the instrument for measuring emissivity at 300 °C.

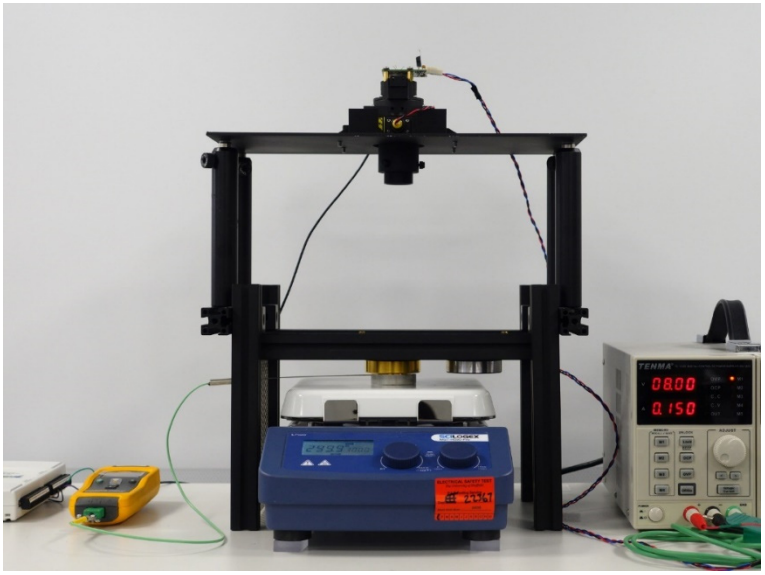

Figure 4.8 Photo of the instrument for the measurement of emissivity of an aluminium sample at 300 °C.

4.4 Instrumental uncertainty

The instrument was developed to carry out accurate and traceable emissivity measurements, which required an analysis of the instrumental uncertainties. The uncertainties of the instrument derive from four main sources: the radiance temperature error, background radiation interference, electronic noise, and systematic errors [9]. Systematic errors are due to the size of source effect (SSE) of the radiation thermometer, geometrical imperfection of cups, position change of samples for each measurement, and curve fitting error. Each emissivity measurement method utilised by the instrument has its own associated uncertainty components, which should be analysed separately. By studying the combined standard uncertainty and relative uncertainty, the most suitable emissivity measurement range of each method can be specified quantitatively.

In this work, the methodology for general uncertainty analysis has been discussed in Section 8.1. The uncertainty corresponding to this instrument will be analysed thoroughly. The combined uncertainty $u_c(x)$ is expressed by Equation (4.14) [10]. The

expanded uncertainty is expressed at approximately the 95% confidence level using a coverage factor of k = 2 [11]:

$$u_c(x) = \sqrt{\sum_{i=1}^{N} [u(x_i)]^2} \tag{4.14}$$

where $u(x_i)$ is a standard uncertainty component.

4.4.1 Blackbody radiance temperature

The radiation thermometer was pre-calibrated by the blackbody furnace to provide reference values for both the black-cup and gold-cup methods. The radiance temperature uncertainty of the blackbody furnace for 200 to 450 °C was lower than ± 0.2 K. The uncertainty (k = 2), $u_1(T_b)$, due to the blackbody radiance temperature error ranged from 0.006 to 0.003 over the measurement temperature range, as shown in Table 4.6.

4.4.2 Sample radiance temperature

The sample temperature was monitored by a type K class 1 thermocouple embedded within the sample. As mentioned previously in Section 4.3.3, the sample exhibited a vertical thermal gradient distribution due to the heating process, which resulted in the uncertainty in measuring the sample surface temperature. There were two components to this uncertainty: the thermocouple uncertainty and the vertical temperature difference between the thermocouple position and the sample top surface.

The thermocouple used in the instrument can measure temperature within an error range of ±1.5 °C over the temperature range of 0 to 375 °C and ±0.4% °C over the temperature range of 375 to 1000 °C. The uncertainty (k = 2), $u_2(T_s)$, due to the thermocouple was from 0.048 to 0.025 between 200 °C and 450 °C.

The thermal properties of the samples, such as heat capacity, thermal conductivity and surface condition, contribute to the vertical temperature difference. This difference was analysed using Ansys Icepak for common materials. The maximum temperature difference (2.10 °C) occurred in SS304 at 450 °C, as shown in Table 4.4. Therefore, the maximum radiance temperature difference was estimated to be 2.5 °C. The uncertainty

(k = 2), $u_3(T_s)$, due to the temperature difference between the sample surface and the thermocouple readout ranged from 0.023 to 0.029, as shown in Table 4.6.

Material	Temperature variation (°C)			
	200 °C	**300 °C**	**400 °C**	**450 °C**
Al6802	−0.12	−0.21	−0.30	−0.35
SS304	−0.75	−1.29	−1.83	−2.10
Inconel	−0.69	−0.76	−0.83	−0.86
Copper	−0.05	−0.08	−0.12	−0.14
HiE-Coat 840M (painted on Al6082)	−0.66	−1.14	−1.62	−1.86
Estimated temperature difference	−0.83	−1.50	−2.17	−2.50

Table 4.4 Simulated temperature difference between the position of the thermocouple and centre of the sample surface

(Note: The temperatures of 200, 300, 400, and 450 °C are the reference temperatures of the position of the thermocouple. The temperature variation indicates that the surface temperature of a sample is lower than the reference temperature.)

4.4.3 Background radiation interference

For each measurement, a sample was heated to the measurement temperature and stabilised for 30 minutes before data acquisition started. During this period, the black-cup and the gold-cup were also exposed to the heating area of the hot plate, emitting background radiation to the sample after covering it. The radiation was reflected by the sample surface, leading to the enhancement of the measured radiant power. The temperature increase of the black-cup and the gold-cup was simulated by Ansys Icepak across the entire measurement temperature range. The result is shown in Table 4.5, and the uncertainty (k = 2), $u_4(S_{gc})$ and $u_5(S_{bc})$, due to the background radiation interference is shown in Table 4.6.

Cup	Simulated temperature (°C)			
	200 °C	**300 °C**	**400 °C**	**450 °C**
Gold-cup	50.14	70.80	94.33	107.07
Black-cup	41.30	55.52	71.27	79.78

Table 4.5 Simulated temperature of gold-cup and black-cup

4.4.4 Electronic noise

The radiation thermometer output fluctuated over the course of the measurement due to the electronic noise of photodiode-amplifier circuit, adding additional uncertainty to the measurement. This uncertainty increased at the lower end of the temperature range, due to the reduced signal-to-noise ratio of the measurement. The uncertainty (k = 2), $u_6(S)$, due to thermometer noise ranged from 0.028 to 0.001 between 200 °C and 450 °C, as shown in Table 4.6.

4.4.5 Size of source effect

Size of source effect describes the phenomenon that a radiation thermometer measures radiation from the region outside of its nominal measurement area [12]. In this work, SSE was measured using the direct method [13], which can be expressed by Equation (2.93). The SSE for the radiation thermometer, measured at a furnace temperature of 450 °C, is shown in Figure 4.9. The actual measurement area was smaller than 2 mm in diameter which agreed with the design specification. The maximum uncertainty, $u_7(L_{SSE})$, caused by SSE was estimated to be 0.006 (k = 2).

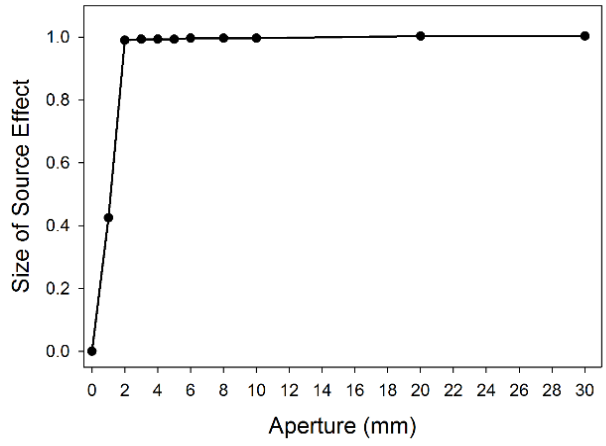

Figure 4.9 SSE of the radiometer measured at 450 °C with a working distance of 150 mm. SSE was close to 1.0 when the aperture was greater than 2 mm in diameter.

4.4.6 Geometrical imperfection

Geometrical imperfections within the shape of the cups can have a direct impact upon the measurement of the emissivity, particularly when using the gold cup. This

imperfection was due to tolerances within the manufacturing process of the cups. For this instrument, the internal surface of the cups was required to be polished to 20 ± 0.02 mm in semi-diameter, whilst the hole at the top of the cups was required to be machined to between 2.00 and 2.05 mm in diameter. The maximum uncertainty (k = 2), $u_8(L_{Geo})$, due to the geometrical imperfection was estimated to be 0.001.

4.4.7 Positioning

Working distance variations between the design specification and the actual working condition, leading to a measurement area change, contributed an additional measurement uncertainty. The positional uncertainty of the working distance variation was estimated to be ± 1 mm, with a maximum uncertainty (k = 2), $u_9(L_p)$, estimated to be 0.015.

4.4.8 Curve fitting error

The use of polynomial equations to fit the relationship between the enhanced effective emissivity and the sample emissivity introduced a residual curve fitting error uncertainty. As analysed in Table 4.2 and Table 4.3, the maximum uncertainty, $u_{10}(\varepsilon_{eff})$, was 0.011 for the gold-cup method (k = 2). The maximum uncertainty, $u_{11}(\varepsilon_{eff})$, was 0.005 for the dual-cup method (k = 2).

4.4.9 Expanded uncertainty

For all the uncertainty components discussed above, the overall uncertainty of the measurements can be calculated using Equation (4.14). The expanded uncertainty (k = 2) was lower than 0.058 at 200 °C, reducing to lower than 0.030 at 450 °C, as shown in Table 4.6. The result for the gold-cup method only represents the uncertainty analysis for enhanced effective emissivity, which should be converted to relative uncertainty for a direct comparison with the other two methods.

Description	Quantity	Black-cup method Temperature (°C)				Dual-cup method Temperature (°C)			
		200	300	400	450	200	300	400	450
Blackbody radiance temperature	$u_1(T_b)$	0.006	0.004	0.003	0.003	N/A	N/A	N/A	N/A
Sample thermocouple	$u_2(T_s)$	0.048	0.033	0.025	0.025	0.048	0.033	0.025	0.025
Sample temperature deviation	$u_3(T_s)$	0.023	0.028	0.029	0.029	N/A	N/A	N/A	N/A
Background radiation (Gold-cup)	$u_4(S_{ac})$	N/A	N/A	N/A	N/A	1.0×10-04	3.2×10-05	2.0×10-05	1.9×10-05
Background radiation (Black-cup)	$u_5(S_{bc})$	1.5×10^{-03}	3.5×10^{-04}	1.7×10^{-04}	1.3×10^{-04}	1.5×10-03	3.5×10-04	1.7×10-04	1.3×10-04
Electronic Noise	$u_5(S)$	0.028	0.003	0.001	0.001	0.028	0.003	0.001	0.001
SSE	$u_7(L_{SSE})$	0.006	0.006	0.006	0.006	0.006	0.006	0.006	0.006
Geometrical imperfection	$u_8(L_{Geo})$	0.001	0.001	0.001	0.001	0.001	0.001	0.001	0.001
Positioning	$u_9(L_p)$	0.015	0.015	0.015	0.015	0.015	0.015	0.015	0.015
Curve fitting I	$u_{10}(\varepsilon_{eff})$	N/A	N/A	N/A	N/A	N/A	N/A	N/A	N/A
Curve fitting II	$u_{11}(\varepsilon_{eff})$	N/A	N/A	N/A	N/A	0.005	0.005	0.005	0.005
Expanded uncertainty	U	**0.062**	**0.046**	**0.042**	**0.042**	**0.058**	**0.037**	**0.031**	**0.030**

Description	Quantity	Gold-cup method Specular surface, Temperature (°C)				Lambertian surface, Temperature (°C)			
		200	300	400	450	200	300	400	450
Blackbody radiance temperature	$u_1(T_b)$	0.006	0.004	0.003	0.003	0.006	0.004	0.003	0.003
Sample thermocouple	$u_2(T_s)$	0.048	0.033	0.025	0.025	0.048	0.033	0.025	0.025
Sample temperature deviation	$u_3(T_s)$	0.023	0.028	0.029	0.029	0.023	0.028	0.029	0.029
Background radiation (Gold-cup)	$u_4(S_{ac})$	1.0×10^{-04}	3.2×10^{-05}	2.0×10^{-05}	1.9×10^{-05}	1.0×10-04	3.2×10-05	2.0×10-05	1.9×10-05
Background radiation (Black-cup)	$u_5(S_{bc})$	N/A	N/A	N/A	N/A	N/A	N/A	N/A	N/A
Electronic Noise	$u_5(S)$	0.028	0.003	0.001	0.001	0.028	0.003	0.001	0.001
SSE	$u_7(L_{SSE})$	0.006	0.006	0.006	0.006	0.006	0.006	0.006	0.006
Geometrical imperfection	$u_8(L_{Geo})$	0.001	0.001	0.001	0.001	0.001	0.001	0.001	0.001
Positioning	$u_9(L_p)$	0.015	0.015	0.015	0.015	0.015	0.015	0.015	0.015
Curve fitting I	$u_{10}(\varepsilon_{eff})$	0.011	0.011	0.011	0.011	N/A	N/A	N/A	N/A
Curve fitting II	$u_{11}(\varepsilon_{eff})$	N/A	N/A	N/A	N/A	N/A	N/A	N/A	N/A
Expanded uncertainty	U	**0.063**	**0.048**	**0.044**	**0.043**	**0.062**	**0.046**	**0.042**	**0.042**

Table 4.6 Expanded uncertainty (k = 2)

(Note: The expanded uncertainty of gold-cup method is evaluated as the form of enhanced effective emissivity.)

4.4.10 Relative expanded uncertainty

The relative expanded uncertainty (k = 2) at 200 °C and 450 °C are shown in Figure 4.10 and Figure 4.11, respectively. Compared to the black-cup method, the dual-cup method consistently demonstrated the lower uncertainty. For materials with a Lambertian surface, which can represent the common surface property in various typical samples, each method had a distinct suitable emissivity measurement range. The gold-cup method was more suitable for the emissivity range of up to 0.22 at 200 °C, and up to 0.18 at

450 °C. The other two methods were found to be less uncertain under the other emissivity range. The lowest relative expanded uncertainty achieved by the gold-cup method was 23.08% at 200 °C and 15.39% at 450 °C, which was equivalent to the expanded uncertainty of 0.021 and 0.0142 (k = 2). The lowest relative expanded uncertainty achieved by the dual-cup method was 5.80% at 200 °C and 3.01% at 450 °C (k = 2). With careful selection of the most appropriate emissivity measurement method, the instrument can achieve the measurement uncertainty lower than 0.058 (k = 2) over the emissivity range of 0.05 to 1.

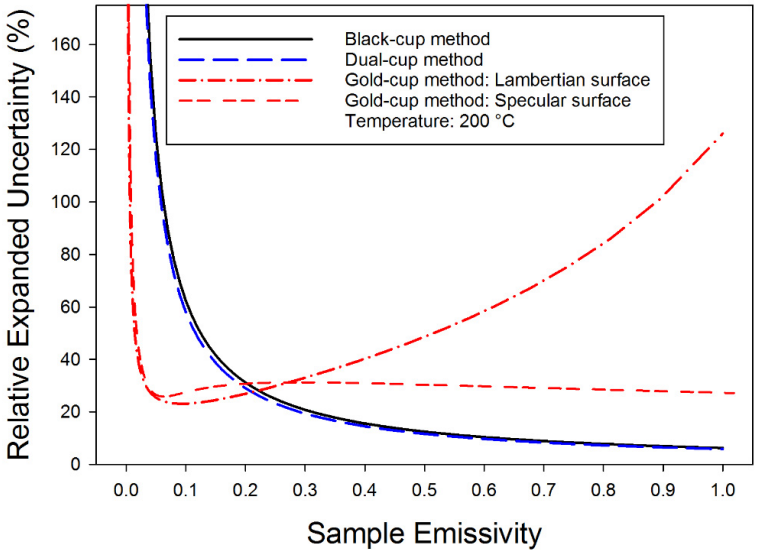

Figure 4.10 Relative expanded uncertainty at 200 °C (k = 2).

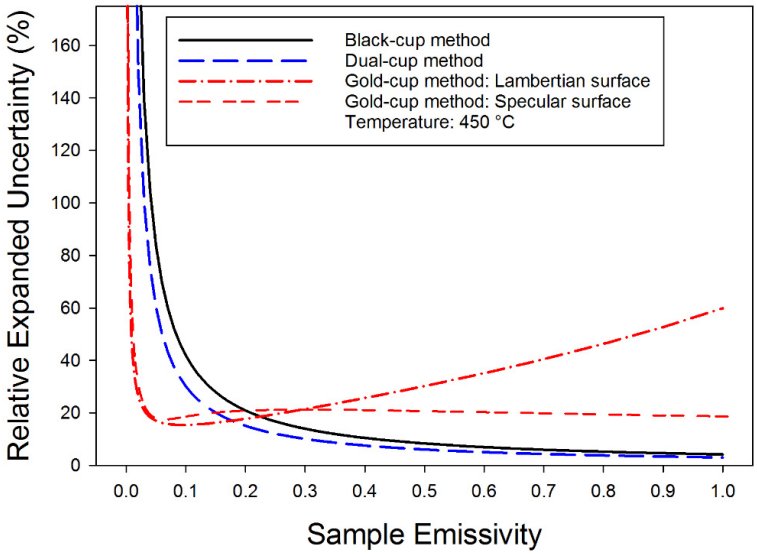

Figure 4.11 Relative expanded uncertainty at 450 °C (k = 2).

4.5 Results and discussion

4.5.1 Results of emissivity measurements on SS304, Al6082, and HiE-Coat 840M

To evaluate the performance of the instrument, five sets of samples were measured, including rough SS304, rough Al6082, polished SS304, polished Al6082, and HiE-Coat 840M paint on an Al6082 substrate. These samples can represent materials that range from low emissivity to high emissivity over the spectral range of 2.1 to 2.5 μm, according to previously published studies [6, 14, 15]. Samples were heated to the measurement temperatures, ranging from 200 to 450 °C, in sequential steps of 50 °C. All samples were exposed to air during measurements, leading to the measured emissivity being accompanied by surface oxidation. Figure 4.12 shows the samples before and after the measurement. The colour of the SS304 samples changed from light grey to light brown, whereas the colour of the other samples remained the same.

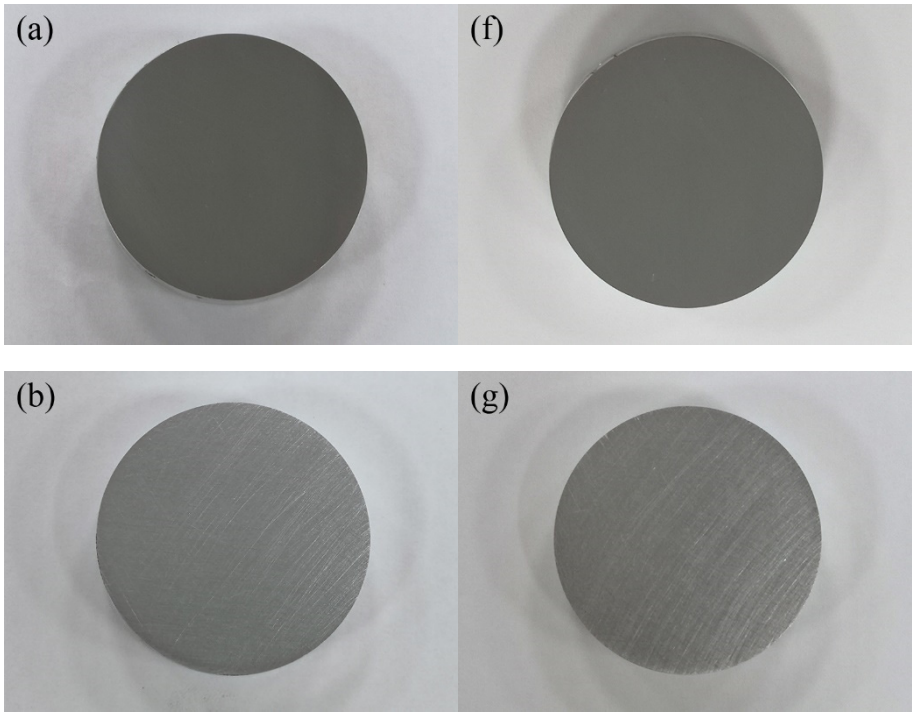

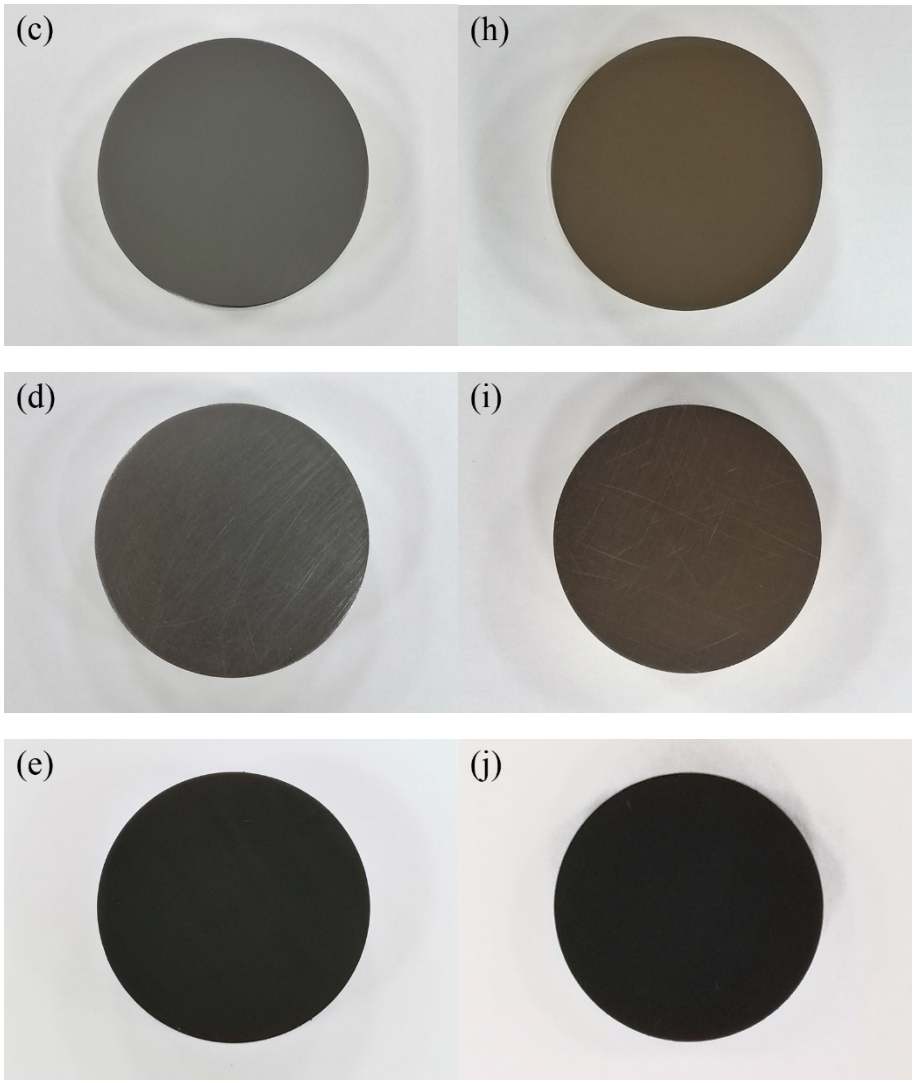

Figure 4.12 Photos of samples before and after the emissivity measurement: (a) to (e) are samples before the measurement and (f) to (j) are samples after the measurement; (a) and (f) are polished Al6082; (b) and (g) are rough Al6082; (c) and (h) are polished SS304; (d) and (i) are rough SS304; (e) and (j) are HiE-Coat 840M painted on Al6082.

Figure 4.13 shows the emissivity of polished Al6082 from 200 to 450 °C. The three measurement methods produced different results. The emissivity measured by the gold-cup method increased from 0.108 at 200 °C to 0.169 at 350 °C, before stabilising to approximately 0.160 from 350 °C to 450 °C. The emissivity measured by the black-cup method increased from 0.090 at 200 °C to 0.135 at 350 °C and then decreased to 0.112 at 450 °C. The emissivity measured by the dual-cup method increased from 0.078 to 0.114 at 350 °C and then decreased to 0.009 at 450 °C.

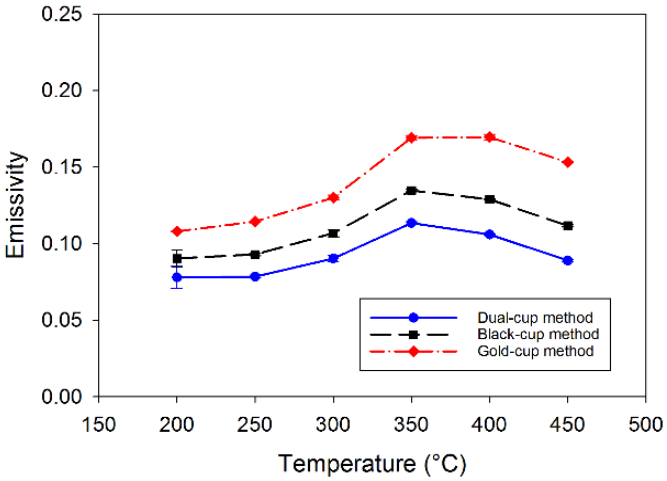

Figure 4.13 Emissivity of polished Al6082. Error bars represent the repeatability of measurements.

Figure 4.14 shows the emissivity of rough Al6082 between 200 °C and 450 °C. The gold-cup method showed an increase in emissivity from 0.142 at 200 °C to 0.182 at 450 °C. Both the black-cup and dual-cup methods indicated that emissivity values were stable at approximately 0.150 over the entire measurement temperature range.

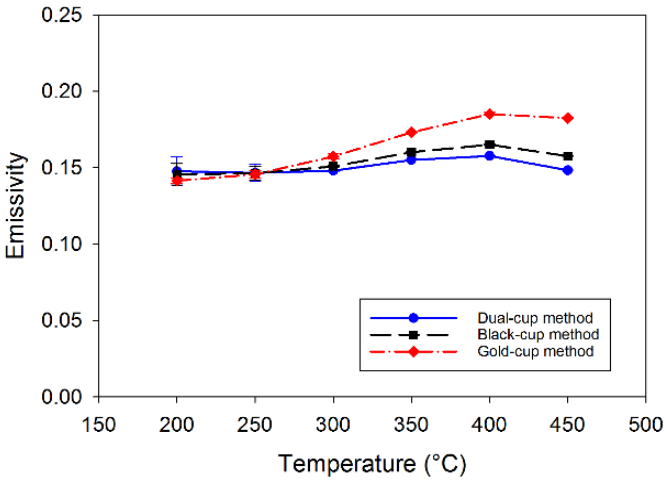

Figure 4.14 Emissivity of rough Al6082. Error bars represent the repeatability of measurements.

Figure 4.15 shows the emissivity of polished SS304 between 200 °C and 450 °C. Similar to the result of polished Al6082, the three methods showed different emissivity performances. The gold-cup method indicated that emissivity increased continuously from 0.265 at 200 °C to 0.316 at 450 °C. The black-cup method measured the emissivity

to be stable at approximately 0.220 over the measurement temperature range, whilst the dual-cup method indicated that emissivity was stable at approximately 0.200.

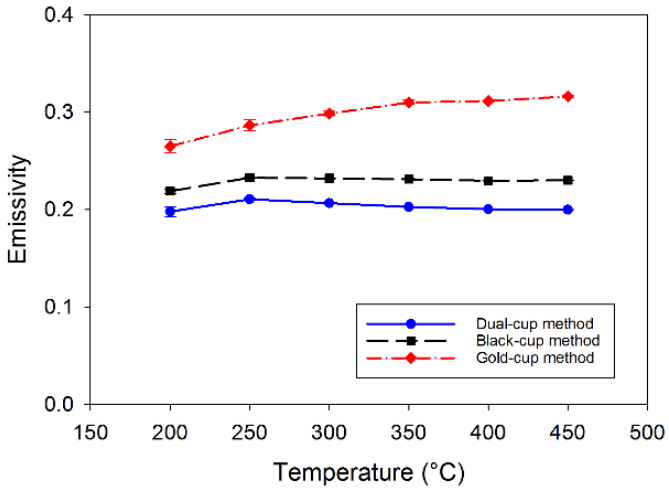

Figure 4.15 Emissivity of polished SS304. Error bars represent the repeatability of measurements.

Figure 4.16 shows the emissivity of rough SS304 from 200 to 450 °C. The three methods showed a similar trend of emissivity value over the measurement temperature range: emissivity was stable at approximately 0.300 from 200 to 300 °C and then increased to approximately 0.380 at 450 °C.

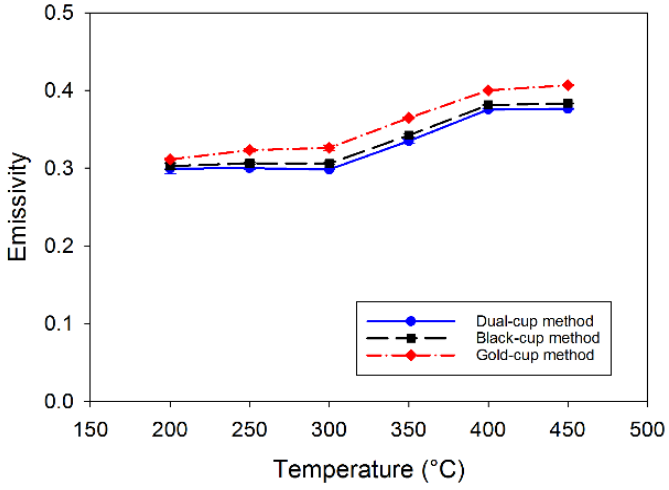

Figure 4.16 Emissivity of rough SS304. Error bars represent the repeatability of measurements.

Figure 4.17 shows the emissivity of HiE-Coat 840M paint from 200 to 450 °C. The results of the gold-cup method were not valid due to the inherent methodology and, therefore, not included in the figure. Both the black-cup and dual-cup methods showed a

similar trend in emissivity, with decreased emissivity from approximately 0.920 to 0.900 from 200 to 450 °C.

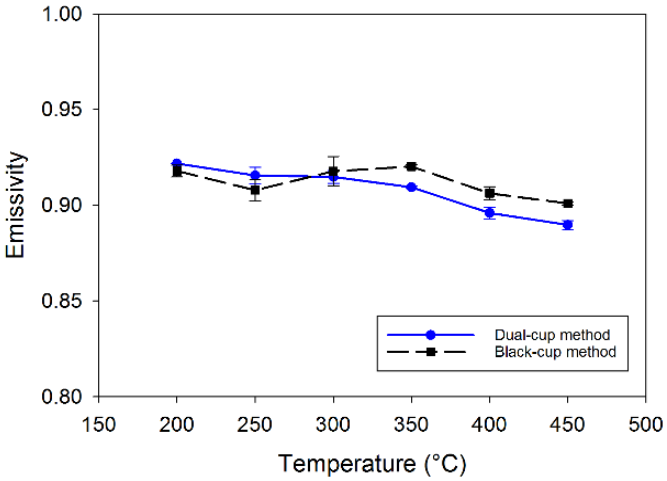

Figure 4.17 Emissivity of HiE-Coat 840M paint. Error bars represent the repeatability of measurements.

4.5.2 Discussion

The samples which have been measured (SS304, Al6082, and HiE Coat 840M) cover a wide range of emissivities; observation of these materials enabled us to evaluate the performance of our instrument. The emissivity of polished Al6082 was within the range of 0.07 to 0.17 over the entire temperature range using all three methods. Similarly, the emissivity of rough Al6082 was consistently measured to be within the range of 0.14 to 0.20. The emissivity of polished SS304 ranged from 0.19 to 0.35 across the measurement methods, whilst the emissivity of rough SS304 ranged from 0.30 to 0.45. For HiE-Coat 840M painted Al6082, the emissivity ranged from 0.90 to 0.92 across the temperature range for both methods assessed. The error bars in Figure 4.13 to Figure 4.17 represent the repeatability of measurements, which are smaller than the overall expanded uncertainty of each measurement method. The emissivity measurements of these materials agree with published measurements of stainless steel, aluminium alloy, and HiE-Coat 840M within the literature [6, 14, 15]. This, therefore, validates the results and instrument approach to emissivity measurements.

Each measurement method has its own most suitable emissivity measurement range, as discussed in Section 4.3.4. Figure 4.13, Figure 4.14 and Figure 4.15 show that the

radiative properties of low emissivity materials, such as the polished Al6082, polished SS304 and rough Al6082, were different between the gold-cup method and the other two methods. The gold-cup method indicated that the emissivity value of these samples increased with rise in temperature, whereas the other two methods did not observe this emissivity change. After performing the measurement, samples were cooled to 200 °C and their emissivities were re-measured. It was found that the measured emissivities did not return to their original values, indicating that surface oxidation of the samples played a dominant role in the emissivity increase. This is consistent with previous studies which also observed a relationship between the surface oxidation and increase in emissivity for stainless steel and aluminium alloys after a long heating period [16, 17]. This kind of emissivity increase was only observed in the gold-cup method, which supported the argument that the gold-cup method can offer a better measurement approach than the other two methods for low emissivity materials.

For middle and high emissivity materials, such as the rough SS304 and HiE-Coat 840M paint, the emissivity measured by the black-cup and dual-cup methods agreed with each other, as shown in Figure 4.16 and Figure 4.17. The increase in the emissivity of rough SS304 was observed using all three methods. Similarly, the measured emissivity values following the cooling phase did not return to the originally measured values at 200 °C. This again indicated that surface oxidation impacted emissivity measurements. These results demonstrated that both the black-cup and dual-cup methods can offer a lower uncertainty for measuring the measurement of middle and high emissivity materials.

For the metal samples, Al6082 and SS304, measured in this work, the surface conditions of these samples changed during the measurement such as the surface chemical composition and surface roughness. Oxidation is a common phenomenon occurring to metal samples, which depends on many factors such as the temperature, oxidation period, humidity, and air flow speed. Thus, emissivity may be affected by the surface condition changes as the result obtained in this work, which requires further studies on emissivity measurements with controlled atmosphere.

4.6 Conclusion

This chapter introduced an instrument for emissivity measurements between temperatures of 200 to 450 °C over a spectral range of 2.1 to 2.5 μm using three different methods. The expanded uncertainty of the instrument is lower than 0.058 at 200 °C and 0.030 at 450 °C (k = 2). This work firstly achieved Monte Carlo simulation of the ray tracing of a gold-cup which has not been done before. Based on the gold-cup and black-cup methods, the dual-cup method, which is a new emissivity measurement method, has been proposed in this work. By thoroughly analysing the various sources of uncertainty, the most suitable measurement range of each method has been quantitatively assessed and determined. The gold-cup method is better for the measurement of low emissivity materials, whereas the black-cup and dual-cup methods are suitable for all other emissivity ranges.

With careful selection of the most appropriate measurement method for a specific application, this instrument can achieve very low relative uncertainty. During the measurements, samples were heated under ambient atmosphere, which may lead to the variation of surface conditions, such as the surface oxidation. These changes may generate impacts on emissivity measurements which requires further analysis.

References

[1] L. Cai *et al.*, “Warming up human body by nanoporous metallized polyethylene textile,” *Nat Commun,* vol. 8, no. 1, pp. 496, Sep 19, 2017.

[2] N. Boone *et al.*, “Thermal near infrared monitoring system for electron beam melting with emissivity tracking,” *Addit. Manuf.,* vol. 22, pp. 601-605, 2018.

[3] J. Martinek *et al.*, “Large area scanning thermal microscopy and infrared imaging system,” *Meas. Sci. Technol.,* vol. 30, no. 3, pp. 035010, 2019.

[4] R. P. Madding, “Emissivity measurement and temperature correction accuracy considerations,” in *Thermosense XXI*, 1999, pp. 393-401.

[5] A. Araújo, “Multi-spectral pyrometry—a review,” *Meas. Sci. Technol.,* vol. 28, no. 8, pp. 082002, 2017.

[6] L. M. Hanssen, S. N. Mekhontsev, and V. B. Khromchenko, “Infrared spectral emissivity characterization facility at NIST,” in *Thermosense XXVI*, 2004, pp. 1-12.

[7] C. Monte *et al.*, “Radiation Thermometry and Emissivity Measurements Under Vacuum at the PTB,” *Int. J. Thermophys.,* vol. 30, no. 1, pp. 203-219, 2008.

[8] R. B. Pérez-Sáez, L. d. Campo, and M. J. Tello, “Analysis of the Accuracy of Methods for the Direct Measurement of Emissivity,” *Int. J. Thermophys.,* vol. 29, no. 3, pp. 1141-1155, 2008.

[9] P. Honnerová *et al.*, “New experimental device for high-temperature normal spectral emissivity measurements of coatings,” *Meas. Sci. Technol.,* vol. 25, no. 9, pp. 095501, 2014.

[10] O. Riou *et al.*, “Accurate methods for single-band apparent emissivity measurement of opaque materials,” *Measurement,* vol. 89, pp. 239-251, 2016.

[11] T. Králík *et al.*, “Method for measurement of emissivity and absorptivity of highly reflective surfaces from 20 K to room temperatures,” *Metrologia,* vol. 53, no. 2, pp. 743-753, 2016.

[12] P. Honnerova *et al.*, “Method for emissivity measurement of semitransparent coatings at ambient temperature,” *Sci. Rep.,* vol. 7, no. 1, pp. 1386, May 3, 2017.

[13] I. Vishnevetsky *et al.*, “Method for accurate measurement of infrared emissivity for opaque low-reflectance materials,” *Appl. Opt.,* vol. 58, no. 17, pp. 4599-4609, Jun 10, 2019.

[14] Z. M. Zhang, B. K. Tsai, and G. Machin, *Radiometric Temperature Measurements: II. Applications*, Cambridge, MA: Academic Press, 2009.

[15] L. P. Wang, S. Basu, and Z. M. Zhang, “Direct and Indirect Methods for Calculating Thermal Emission From Layered Structures With Nonuniform Temperatures,” *J. Heat Transfer,* vol. 133, no. 7, pp. 072701, 2011.

[16] C.-D. Wen, and I. Mudawar, “Mathematical determination of emissivity and surface temperature of aluminum alloys using multispectral radiation thermometry,” *Int. Commun. Heat Mass Transfer,* vol. 33, no. 9, pp. 1063-1070, 2006.

[17] G. Goett *et al.*, “Emissivity and temperature determination on steel above the melting point,” *Weld. World,* vol. 57, no. 4, pp. 595-602, 2013.

[18] P. Wang *et al.*, "A new experimental apparatus for emissivity measurements of steel and the application of multi-wavelength thermometry to continuous casting billets," *Rev. Sci. Instrum.,* vol. 89, no. 5, pp. 054903, 2018.

[19] International Organisation for Standardisation, *Guide to the Expression of Uncertainty in Measurement (GUM)*, Geneva: International Organisation for Standardisation, 1995.

[20] J. R. Howell, and R. Siegel, *Thermal radiation heat transfer*, 3rd ed., New York: Hemisphere Publishing Co., 1992.

[21] M. D. Drury, K. P. Perry, and T. Land, "Pyrometers for surface-temperature measurement," *J. Iron Steel Inst.,* vol. 169, no. 3, pp. 245-250, 1951.

[22] Edmund Optics Ltd, "Metallic Mirror Coatings. Nether Poppleton, UK," [Online]. Available: https://www.edmundoptics.eu/resources/application-notes/optics/metallic-mirror-coatings/, 2019.

[23] J. Fischer *et al.*, "Uncertainty budgets for realisation of scales by radiation thermometry," [Online]. Available: https://www.bipm.org/cc/CCT/Allowed/22/CCT03-03.pdf, 2003.

[24] L. del Campo *et al.*, "Combined standard uncertainty in direct emissivity measurements," *J. Appl. Phys.,* vol. 107, no. 11, pp. 113510, 2010.

[25] H. W. Yoon, D. W. Allen, and R. D. Saunders, "Methods to reduce the size-of-source effect in radiometers," *Metrologia,* vol. 42, no. 2, pp. 89-96, 2005.

[26] P. Saunders, and H. Edgar, "On the characterization and correction of the size-of-source effect in radiation thermometers," *Metrologia,* vol. 46, no. 1, pp. 62-74, 2009.

[27] R. K. Maynard *et al.*, "Total Hemispherical Emissivity of Potential Structural Materials for Very High Temperature Reactor Systems: Hastelloy X," *Nucl. Technol.,* vol. 172, no. 1, pp. 88-100, 2017.

[28] Aremco Products Inc., "High Temperature Specialty Coatings. Valley Cottage, N.Y.," [Online]. Available: www.aremco.com/wp-content/uploads/2015/06/TechNote-840-M.pdf, 2015.

[29] C.-D. Wen, and I. Mudawar, "Emissivity characteristics of polished aluminum alloy surfaces and assessment of multispectral radiation thermometry (MRT) emissivity models," *Int. J. Heat Mass Transfer,* vol. 48, no. 7, pp. 1316-1329, 2005.

[30] D. Shi *et al.*, "Effect of surface oxidization on the spectral emissivity of steel 304 at the elevated temperature in air," *Infrared Phys. Technol.,* vol. 66, pp. 6-12, 2014.

Chapter 5. Analysis of impacts on emissivity behaviours due to surface oxidation

5.1 Introduction

The emissivity of a sample heated under ambient atmosphere demonstrates a permanent change before and after measurements, as discussed in Chapter 4. Emissivity is dependent upon surface conditions, including the surface roughness, chemical composition and micro-scale structures besides the temperature, wavelength, and viewing condition. [1]. The process of oxidisation, or chemical erosion, changes the surface conditions dramatically, especially under high temperature conditions, leading to the change of emissivity [2, 3]. The oxidisation process is affected by many factors such as humidity, gas flow speed, heating duration, and heating rate. Therefore, it is necessary to understand the fundamental mechanism of emissivity of oxidised samples, with repeatable levels of surface oxidisation processes.

This chapter introduces the development of an instrument to study the relationship between temperature, emissivity and oxidising conditions. The instrument was designed for measuring normal emissivity of opaque materials under a controlled atmosphere, based on the direct emissivity measurement method. The measurement temperature was from 973 to 1423 K and the spectral range was from 0.85 to 1.1 μm. The expanded uncertainty (k = 2) was lower than 0.059 over the whole measurement temperature. Polished stainless steel 304 (SS304) was selected for undertaking the study. The surface condition of SS304 samples were analysed by scanning electron microscopy (SEM) and energy-dispersive X-ray spectroscopy (EDX). The connection between emissivity and the surface composition changes of SS304 was observed and discussed during the oxidisation process.

At high temperature range, emissivity measurements are mostly undertaken by direct methods with a separate blackbody furnace and sample heater, as introduced in Chapter 3. Samples can be heated by using the methods of furnace heating [4], induction heating [5], or laser heating [6]. However, the blackbody cavity and the sample cannot be heated to the identical temperature due to the separation of the heating equipment. The thermal difference between the blackbody and sample introduces unwanted uncertainty [7]. In this work, a custom sample-blackbody component was developed to eliminate this uncertainty, which will be discussed in detail in this chapter.

5.2 Experimental setup and measurement procedures

5.2.1 Emissivity measurement instrument

The emissivity measurement instrument was composed of a split furnace, two radiometers, a radiation shield, a sample-blackbody component and the gas system. The schematic diagram of the instrument construction is shown in Figure 5.1. The radiation shield and sample-blackbody component were placed inside the furnace ceramic tube, as shown in Figure 5.2.

A commercial split tube furnace (Carbolite HST 12/400) was positioned upon an optical table. The sample-blackbody housing was placed in the middle of the furnace tube. A sample was mounted within the sample recess, opposite the blackbody cavity, and fixed tightly by a sample locking ring. Two type K thermocouples (TC Direct 405-038-Class 1) were embedded within the sample assembly, to monitor the temperature of the cavity and the sample but not to take part in the emissivity measurement itself. One of these was inserted into a hole adjacent to the cavity and the other was embedded adjacent to the sample. The sample, blackbody and thermocouple were designed to achieve good thermal equilibrium by means of machining the assembly from a single piece of Inconel 625. Inconel 625 is a nickel-chromium-based alloy that can form a stable passivating oxide layer protecting the surface from further oxidation under the high temperature environment, which is the ideal material for making the sample-blackbody housing [8].

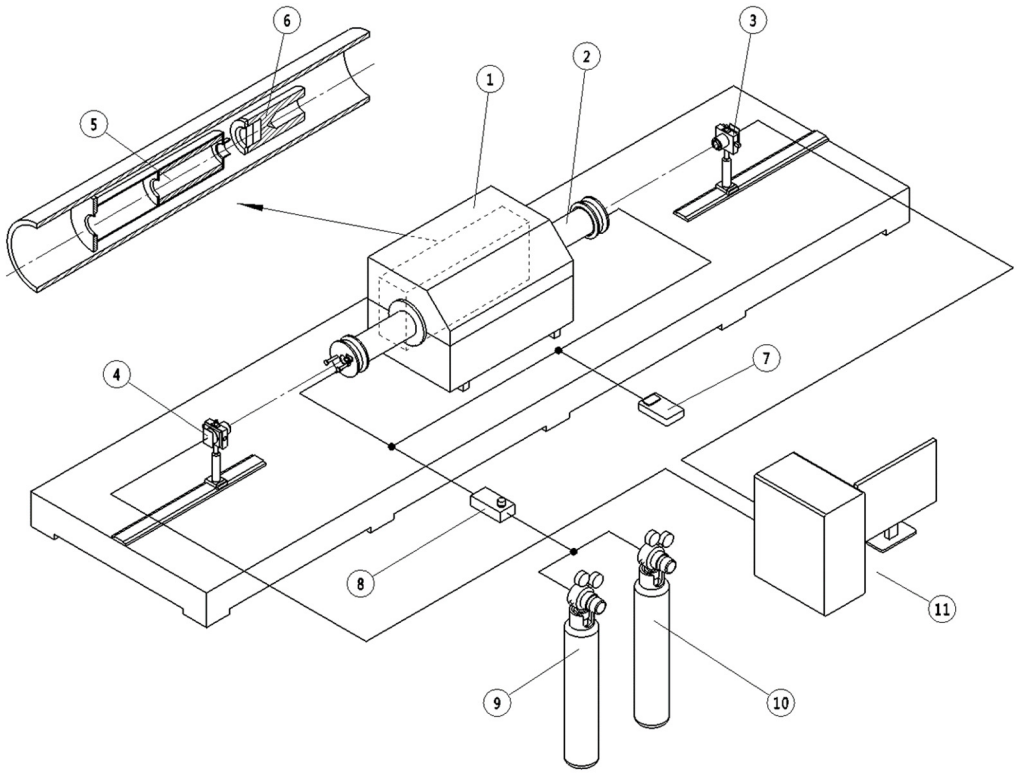

Figure 5.1 Schematic diagram of the emissivity measurement instrument construction. Split furnace (1); ceramic tube (2); radiometer I at the blackbody side (3); radiometer II at the sample side (4); radiation shield (5); sample-blackbody component (6); oxygen meter (7); flow meter (8); nitrogen cylinder (9); compressed air cylinder (10); data acquisition system (11).

Inside the tube, a movable radiation shield was placed over the sample for a very brief period during the measurement, to prevent background radiation from reaching the radiometer. Outside the tube, an optical switch was fixed on the tube end at the sample side, to indicate the start of valid data recorded when the radiation shield achieved its correct position for the measurement. Two custom fabricated radiometers were placed at the blackbody side and the sample side, identified as radiometer I and radiometer II respectively. They were aligned and fixed upon the optical table before each measurement.

A methodology was devised and used to control the atmosphere surrounding the sample, within the furnace tube. Compressed air and nitrogen were input into the sealed tube in ratios determined by a valve mechanism. Compressed air was input to grow oxide layers upon the sample in a controlled fashion, whilst nitrogen was added to protect the sample from oxidising. The gas flow rate was adjusted and monitored by a flow meter with a

scale that ranged from 0.1 to 0.5 litres per minute (lpm). The oxygen level inside the tube was monitored by an oxygen meter that was connected to the gas line.

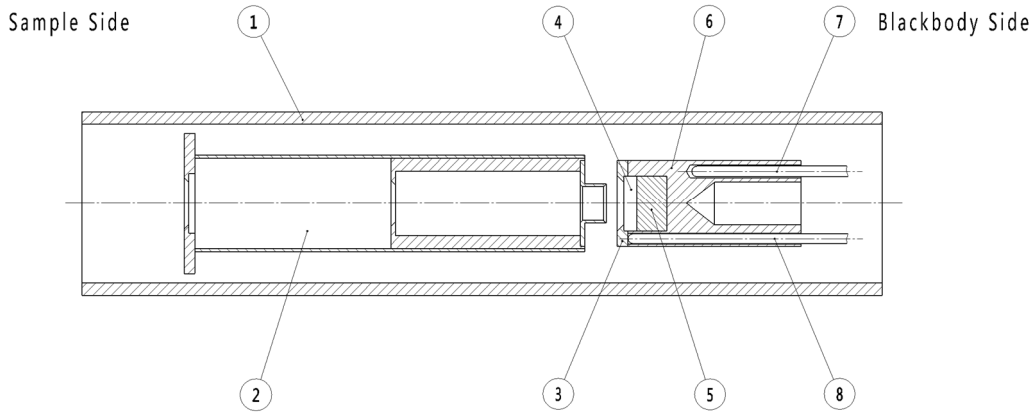

Figure 5.2 Cross-section diagram of the furnace ceramic tube (top view). Ceramic tube (1); radiation shield (2); sample locking ring (3); sample (4); adjusting block (5); sample-blackbody housing (6); cavity thermocouple (7); sample thermocouple (8).

5.2.1.1 Radiometers

Two radiometers were custom fabricated and calibrated to achieve measurements that were identical: within the ability to measure differences between them. The radiometer was designed as a common-path optical system with a red laser (650 nm) and a silicon (Si) photodiode. The laser was used as a sight alignment tool for measurements. The schematic diagram of a radiometer is shown in Figure 5.3. The lens selected for the radiometer was a commercial 60 mm focal length singlet (Edmund optics 45-127). The detector module consisted of an RG850 filter (Edmund optics 66-107), a 0.2 mm diameter field stop and a Si photodiode (Hamamatsu S1133-01). The spectral responsivity of the radiometer is determined by the detector spectral responsivity and RG850 transmissivity, which are shown in Figure 5.4. The real responsivities of two radiometers are not identical, which requires the further responsivity correction to eliminate this deviation. The parameters of the radiometer are listed in Table 5.1.

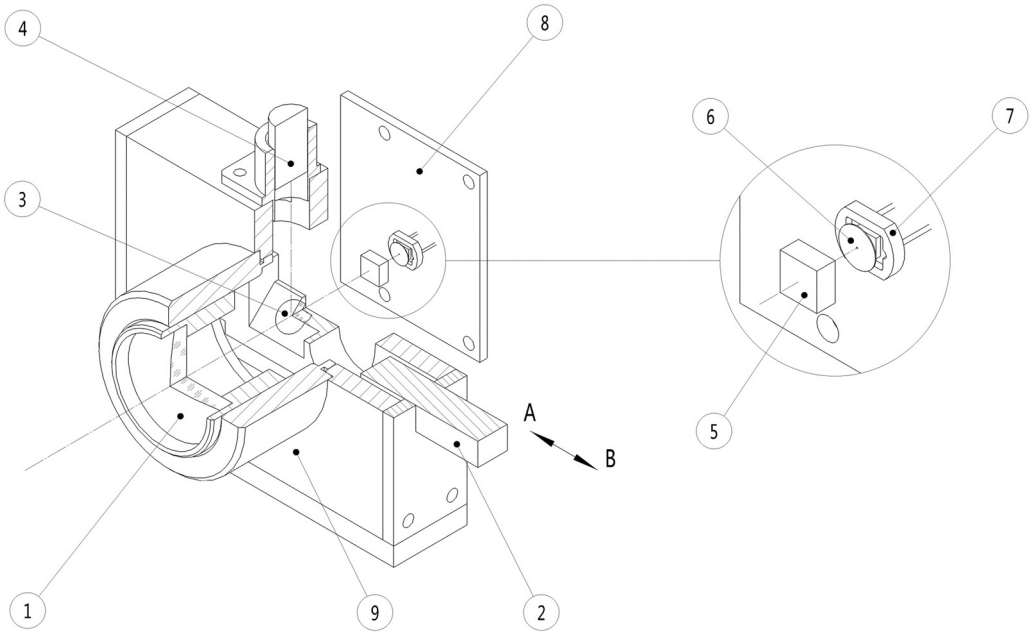

Figure 5.3 Schematic diagram of the radiometer. Singlet lens (1); slide block (2); mirror (3); laser module (4); RG850 filter (5); 0.2 mm diameter field stop (6); Si photodiode (7); PCB (8); radiometer brackets (9). The slide block, which was designed with a mirror and a hole, was used to switch optical paths between the red laser and Si photodiode, either at position A or B.

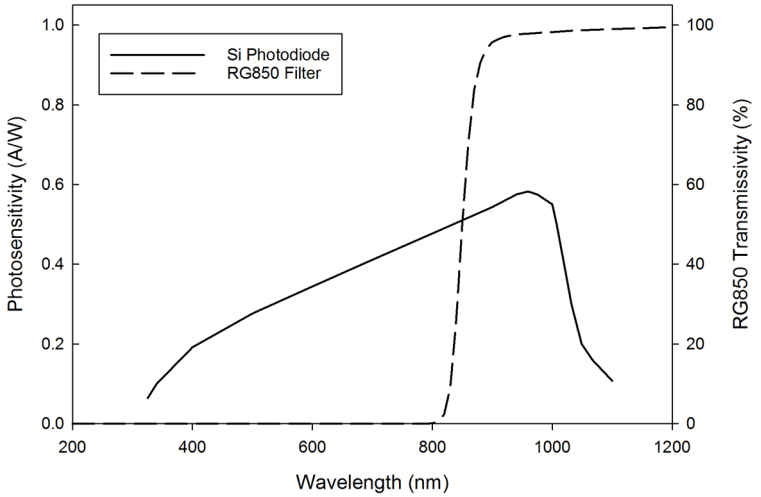

Figure 5.4 Spectral responsivity of the radiometers. The right axis represents the photosensitivity of the Si photodiode. The left axis represents the internal transmissivity of a 3 mm thick RG850 filter.

Parameter	Result
Wavelength	0.85 to 1.1 μm
Focal length	60 mm
F-number	3.0
NA	0.167
Working distance	1.00 m
Field stop	0.2 mm in diameter
Field-of-view/DTR (Design)	80:1
Spot size at working distance (Design)	12.5 mm in diameter

Table 5.1 Parameters of the radiometers

5.2.1.2 Sample-blackbody housing

The cross-section diagram of the sample-blackbody housing is shown in Figure 5.5. A sample recess and a cavity were machined on each side of the housing. The cavity wall was turned with threads and painted with high emissivity material, HiE-Coat 840-MX, to increase the effective emissivity, which was above 0.996 according to Gouffe's theory [9]. The sample-blackbody housing was designed for two specific benefits. Firstly, both the sample and the blackbody cavity were heated in the thermal equilibrium area of a furnace and, therefore, their temperatures can be considered to be identical. Secondly, the blackbody cavity was designed to match the measurement area of the radiometers, leading to a low uncertainty even in the presence of the size of source effect (SSE) [10].

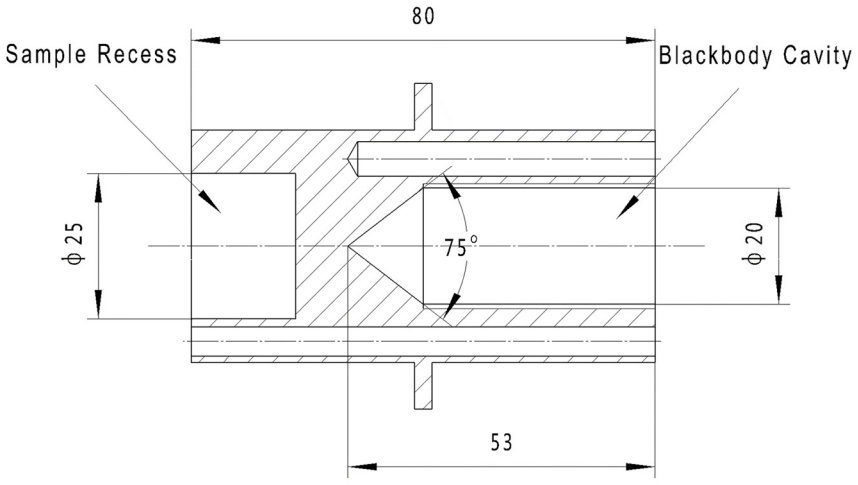

Figure 5.5 Cross-section diagram of the sample-blackbody housing. The dimension of the sample recess was 25 mm in diameter by 6 mm thick. The dimension of the blackbody cavity was 20 mm in diameter. The bottom of blackbody cavity was machined with a 75° cone.

5.2.1.3 Radiation shield

A radiation shield was used to eliminate the radiation received by the sample from the hot tube wall. The shield was composed of a stainless steel housing and three optical baffles placed along the housing as shown in Figure 5.6. In addition, the internal shield surface was coated with HiE-Coat 840-MX to absorb stray radiation. The external shield surface was kept as the brushed stainless steel finishes to reduce the heat radiated from the furnace tube to the shield. Two rows of SiC balls were mounted at the bottom of the shield, which enabled it to be moved from the tube end to the centre within 2 seconds to minimise thermal disruption to the furnace.

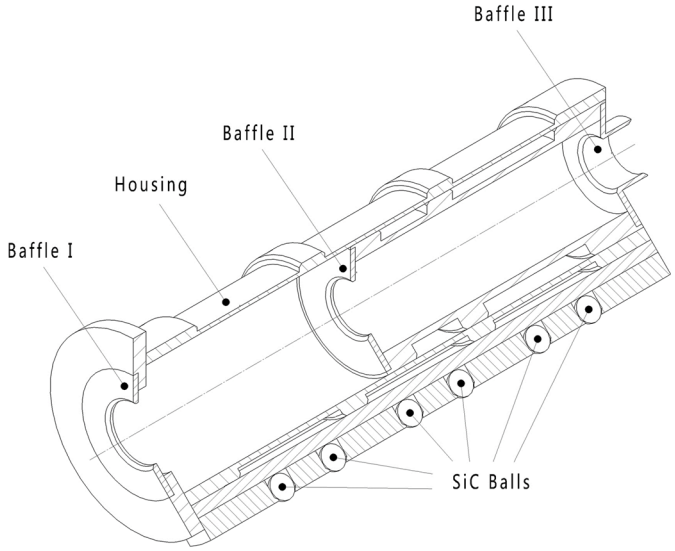

Figure 5.6 Cross-section diagram of the radiation shield.

5.2.2 Measurement procedures

The first step in the emissivity measurements was to mount the sample inside the sample-blackbody housing. The housing was then pushed to the centre of the furnace tube. The two radiometers were aligned and focused on the conical section of the blackbody cavity and the sample centre, respectively. With the furnace stabilised at the set target temperature, the data acquisition system started to log the measured output from the radiometers. Whilst recording the measured sample radiation, the radiation shield was pushed into the tube to cover the sample. As soon as the shield was in position, the optical switch was triggered to indicate the start of valid data. Following completion of data

acquisition, the shield was then retracted and the furnace was set to the next temperature point, allowed to stabilise in temperature and a new measurement was taken. Figure 5.7 shows a photograph of the instrument during emissivity measurements at 1423 K.

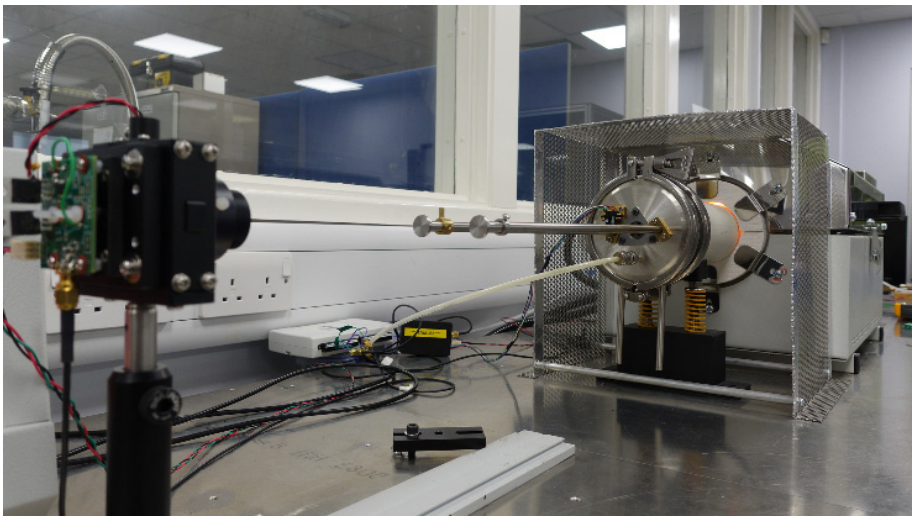

Figure 5.7 Photograph of the instrument when measuring emissivity at a sample temperature of 1423 K. The photograph was taken from the sample side; the radiation shield pusher rod can be seen projecting from the furnace. One of the two radiometers can be seen to the left-hand-side of the figure.

5.2.3 Sample preparation

Commercial grade type 304 stainless steel samples were prepared for the emissivity measurement. The emissivity of this material has been studied by several researchers using various temperature conditions and wavelengths previously [11, 12]. Although emissivity of SS304 between 0.85 and 1.1 μm has not been published, the data from previous studies can be considered as reference results to evaluate the performance of the emissivity measurement instrument.

Samples were cut to 25 mm in diameter by 6 mm thick from a SS304 rod. The top flat surface was ground by P240, P400, P800 grinding papers and polished to 3 μm by diamond suspensions. Samples were ultrasonically cleaned using isopropyl alcohol, fully dried and stored in a vacuum box prior to the measurements.

5.2.4 Measurement strategy

Samples were divided into two sets for different measurement methods. The first set was free from deliberate oxidation, to enable a comparison with previous work. This set of samples was measured within a nitrogen atmosphere at five temperatures: 973, 1073, 1173, 1273 and 1423 K. The second set was oxidised, with the aim of measuring emissivity trends under different oxidising conditions. This set was processed as follows. At first, a sample was heated within a nitrogen atmosphere to 973 K. After the furnace had stabilised for 30 minutes, air was input into the furnace tube at a flow rate of 0.5 lpm, to displace the nitrogen, for oxidising the sample. Emissivity was measured every ten minutes during the whole oxidising period. Other samples were measured with the same oxidising procedure at 1073, 1173, 1273 and 1423 K.

5.3 Methodology

In radiometry, spectral normal emissivity, $\varepsilon(\lambda, T)$, can be derived from Equation (2.18)

$$\varepsilon(\lambda, T) = \frac{L_s(\lambda, T)}{L_b(\lambda, T)} \tag{5.1}$$

where λ is the wavelength, T is the temperature, $L_s(\lambda, T)$ is the radiance from a body, and $L_b(\lambda, T)$ is the radiance from a blackbody. The spectral radiance of a blackbody, $L_b(\lambda, T)$, can be obtained by Equation (2.10).

For emissivity measurements, optical detectors simultaneously receive radiant power emitting from a sample and a blackbody, S_s and S_b, and convert them to electrical signals, as derived from Equation (2.91).

$$S_s(\lambda, T_s) = \Omega_s A_s \tau_{air} \int_{\lambda_1}^{\lambda_2} \varepsilon_s(\lambda, T_s) L_b(\lambda, T_s) R_s(\lambda) \tau_s(\lambda)\, d\lambda \tag{5.2}$$

$$S_b(\lambda, T_b) = \Omega_b A_b \tau_{air} \int_{\lambda_1}^{\lambda_2} L_b(\lambda, T_b) R_b(\lambda) \tau_b(\lambda)\, d\lambda \tag{5.3}$$

where subscript "b" denotes blackbody, "s" denotes sample, Ω is the solid angle, A is the measurement area upon the target, τ_{air} is the propagation coefficient of the atmosphere, $R(\lambda)$ is the relative spectral responsivity of detectors, and $\tau(\lambda)$ is the total transmissivity of the optical path.

The spectral responsivity of a detector and total transmissivity of the optical path of a radiometer are functions of wavelength. If a narrow band pass filter is used in the system, these two factors can be regarded as independent of wavelength [13]. The solid angle, measurement area and spectral responsivity difference between two identical radiometers can be reduced to an acceptable level if they are calibrated and corrected carefully, which implies $\Omega_s \approx \Omega_b$, $A_s \approx A_b$ and $R_s(\lambda) \approx R_b(\lambda)$. When radiometers are placed within a stable environment, the transmissivity of the optical paths of the sample and the blackbody are similar, leading to the elimination of $\tau_s(\lambda)$ and $\tau_b(\lambda)$. The spectral normal emissivity of a sample then can be expressed as

$$\varepsilon_s(\lambda, T) \approx \frac{S_s(\lambda, T_s)}{S_b(\lambda, T_b)} \tag{5.4}$$

In actual working conditions, a radiometer receives radiant power not only from a sample but also from its surroundings: by background-radiation, reflection, and scattering. This leads to an apparent, unwanted, increase in emissivity. The total radiant power measured by a radiometer can be expressed as

$$\begin{aligned} &S_{s,meas}(\lambda, T) = \\ &S_s(\lambda, T) + S_{sur,rfl}(\lambda, T) + S_{sur}(\lambda, T) + S_{s,rfl}(\lambda, T) + S_{mult-rfl}(\lambda, T) \end{aligned} \tag{5.5}$$

where $S_s(\lambda, T)$ is the measured radiant power from a sample, $S_{sur,rfl}(\lambda, T)$ is the measured radiant power from surroundings reflected by a sample, $S_{sur}(\lambda, T)$ is the measured radiant power from surroundings, $S_{s,rfl}(\lambda, T)$ is the measured radiant power from a sample reflected by surroundings, and $S_{mult-rfl}(\lambda, T)$ is the measured radiant power from a sample or surroundings reflected multiple times.

For an opaque object, reflectivity and emissivity can be described by Kirchhoff's law, as expressed by Equation (2.47). If the measurement area is strictly limited within the sample surface, radiation from outside the measurement area can only be received

following scattering. In Equation (5.5), $S_{sur}(\lambda,T)$, $S_{s,rfl}(\lambda,T)$, and $S_{mult-rfl}(\lambda,T)$ are small quantities compared to the first two terms, which can be omitted. Therefore, the measured radiant power of a radiometer can be simplified to

$$S_{s,meas}(\lambda,T) = \Omega_s A_s \tau_{air} \int_{\lambda_1}^{\lambda_2} \varepsilon_s(\lambda,T_s) L_b(\lambda,T_s) R_s(\lambda) \tau_s(\lambda)\, d\lambda + \left(1-\varepsilon_s(\lambda,T_s)\right)\Omega_s A_s \tau_{air} \int_{\lambda_1}^{\lambda_2} \varepsilon_{sur}(\lambda,T_{sur}) L_b(\lambda,T_{sur}) R_s(\lambda) \tau_s(\lambda)\, d\lambda \tag{5.6}$$

where T_s is the temperature of sample, $\varepsilon_{sur}(\lambda,T_{sur})$ is the emissivity of surroundings and T_{sur} is the temperature of the surroundings.

In this work, a cold, high emissivity, radiation shield, as introduced in Section 5.2.1.3, is applied to block the background radiation from the furnace tube during measurements, which represents $\varepsilon_{sur} \approx 1 \; and \; T_{sur} \ll T_s$. So the emissivity measured can be expressed as

$$\varepsilon_s(\lambda,T) \approx \frac{S_{s,meas}(\lambda,T_s)}{S_b(\lambda,T_b)} \tag{5.7}$$

5.4 Instrumental uncertainty

The uncertainties in the measurement can be categorised into three main sources: the approximate nature of the cavity blackbody, characteristics of the radiometers, and the operational procedures. The radiant power measured by the radiometers was affected by the size of source effect [10], responsivity correction, and electronic noise. Furthermore, operational procedures also introduced uncertainties, such as the misalignment and the perturbation that was due to the radiation shield. In this work, the methodology for general uncertainty analysis has been discussed in Section 8.1. The uncertainty corresponding to this instrument will be analysed thoroughly. Equation (5.4) can be rewritten to Equation (5.8) for analysing uncertainties quantitatively.

$$\varepsilon_s(\lambda, T_s) = \frac{S_s(\lambda, T_s)}{S_b(\lambda, T_b)} \cdot \frac{\Omega_b A_b R_b(\lambda) \tau_b(\lambda) \varepsilon_{eff,b}(\lambda, T_b) L_b(\lambda, T_b)}{\Omega_s A_s R_s(\lambda) \tau_s(\lambda) L_b(\lambda, T_s)} \tag{5.8}$$

where $L_b(\lambda, T_s)$ is the spectral radiance of an ideal blackbody, $\varepsilon_{eff,b}(\lambda, T_b)$ is the effective emissivity of an actual blackbody source, and $L_b(\lambda, T_b)$ is the spectral radiance of an ideal blackbody.

The combined standard uncertainty $u_c(x)$ is expressed by Equation (5.9) [14]. The expanded uncertainty is expressed at approximately the 95% confidence level using a coverage factor of k = 2 [15].

$$u_c(x) = \sqrt{\sum_{i=1}^{N} [u_i(x)]^2} \tag{5.9}$$

where $u(x_i)$ is a standard uncertainty component.

5.4.1 Blackbody emissivity, isothermal

The custom designed cavity blackbody applied in this work is not an ideal blackbody, whose effective emissivity can be determined by the wall emissivity, geometry factors, and machining imperfections under isothermal conditions [16, 17]. The geometry of the blackbody cavity may have deviated from the design due to manufacturing errors, leading to the imperfections in the cavity shape. Assuming the cavity was machined to the required mechanical tolerances, the geometry was maintained to ± 0.2 mm in length and ± 0.5° in angle. The maximum uncertainty (k = 2), $u_1(\varepsilon_{eff,b})$, was estimated to 0.014 over the whole temperature range.

5.4.2 Blackbody emissivity, non-isothermal

The effective emissivity of a cavity blackbody decreases under non-isothermal conditions, due to non-uniform thermal distributions along the cavity. This distribution is affected by two factors: the thermally uniform length of the furnace and the heat exchanged between the cavity and its surroundings. The maximum uncertainty (k = 2), $u_2(\varepsilon_{eff,b})$, was estimated to 0.008.

5.4.3 Blackbody cavity radiance temperature

To assess the radiance temperature of the approximate blackbody cavity, a class-1 thermocouple was inserted alongside the cavity and in thermal contact with it. The tolerance of the thermocouple (±1.5 °C or ±T × 0.004 °C) was used to compute the uncertainty in radiance temperature of the blackbody, $u_3(T_b)$, which ranges from 0.038 to 0.048 (k = 2).

5.4.4 Size of source effect

The SSE of each radiometer was measured, to calculate the area over which the measurement area impinged upon the blackbody cavity and the sample. SSE arises as a consequence of optical aberrations, diffractions, reflections and scattering between lens interfaces [10]. In this work, the direct method was applied to measure the SSE, expressed as Equation (2.98) [18]. The background radiation was assumed to be neglected for measurements above 200 °C [19].

The SSE for the radiometers measured at 1073 K and 1273 K are shown in Figure 5.8. The nominal design measurement of 14 mm in diameter was used as the reference measurement area, which was smaller than 25 mm diameter samples. The uncertainties of two radiometers due to SSE, $u_4(L_{SSE})$ and $u_5(L_{SSE})$, are listed in Table 5.4.

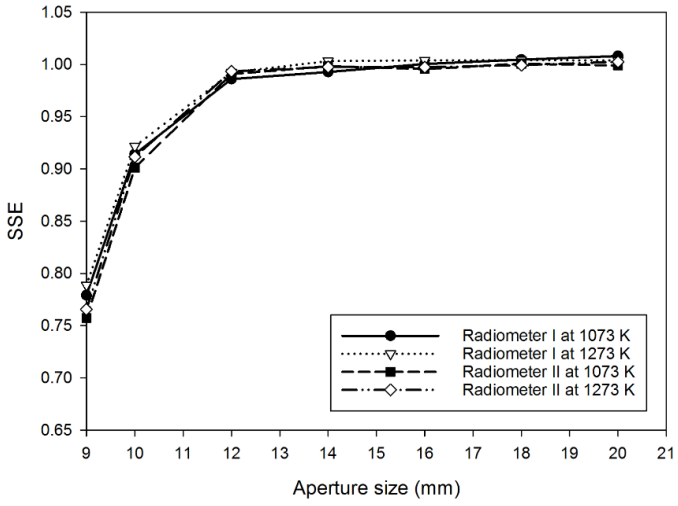

Figure 5.8 SSE of the radiometers measured at 1073 K and 1273 K. When the aperture was greater than 14 mm in diameter, SSE of each radiometer was close to 1. The slight fluctuations were caused by the electronic noise of the radiometers or the temperature drift of the furnace.

5.4.5 Responsivity correction

Emissivity was computed by taking the ratio of the signals from two identical (by design) radiometers. There were slight differences in responsivity of these radiometers, due to the variation in spectral response of photodiodes and the transmissivity of optical elements. In this work, both radiometers were corrected against a calibrated blackbody furnace, LANDCAL R1500 T. The responsivity of radiometer II was corrected to match that of radiometer I by applying least square fitting [20]. The correction is shown in Figure 5.9, with the maximum uncertainty (k = 2), $u_6(R)$, calculated to be 0.003.

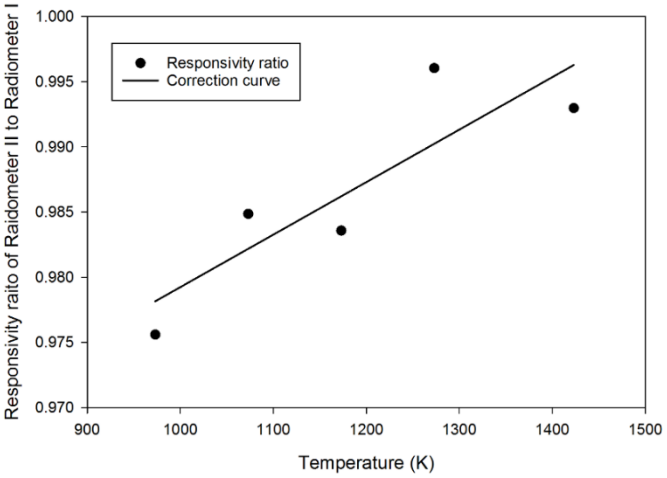

Figure 5.9 Spectral responsivity correction of the radiometers.

5.4.6 Electronic noise

The radiometer output fluctuated during the course of the measurement, adding additional uncertainty due to electronic noise within the radiometers. This uncertainty increased at the lower end of the temperature range, due to the lower signal-to-noise ratio, as a result of the reduced power from the target. Between 973 K and 1423 K, the uncertainties (k = 2) due to radiometer noise of radiometers I, $u_7(S)$, ranged from 0.014 to 0.0002; uncertainties (k = 2) due to radiometer noise of radiometers II, $u_8(S)$, ranged from 0.016 to 0.0003.

5.4.7 Temperature fluctuation of the sample and the radiation shield

A measurement time of 1 second was required to record valid data. With the radiation shield in place during this period, the temperature of the sample decreased, whilst that of the shield increased. A numerical model was built in Ansys Icepak to analyse their thermal conditions dynamically. The temperature change of the radiation shield and the sample are shown in Figure 5.10 and Figure 5.11. The radiance changes are listed in Table 5.2 and Table 5.3. The thermally induced radiance increase of the radiation shield was close to zero in experiments; according to Planck's law, the wavelength of the increased radiance was outside the responsivity spectrum of the radiometers [21].

The temperature of samples was monitored by a thermocouple during emissivity measurements. The measured temperature decrease was found to be lower than the simulation result if the time for sliding the radiation shield into place was no more than 2 seconds. Therefore, the simulation result was in the calculation of uncertainty. The uncertainty (k = 2) due to the temperature decrease of a sample, $u_9(T_s)$, ranged from 0.019 to 0.034. The uncertainty (k = 2) due to the background radiation from the shield, $u_{10}(T_{BC})$, were ignored.

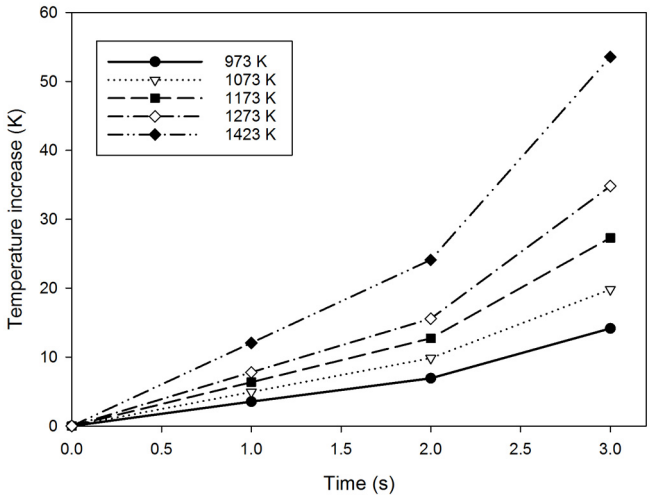

Figure 5.10 Temperature increase of the radiation shield.

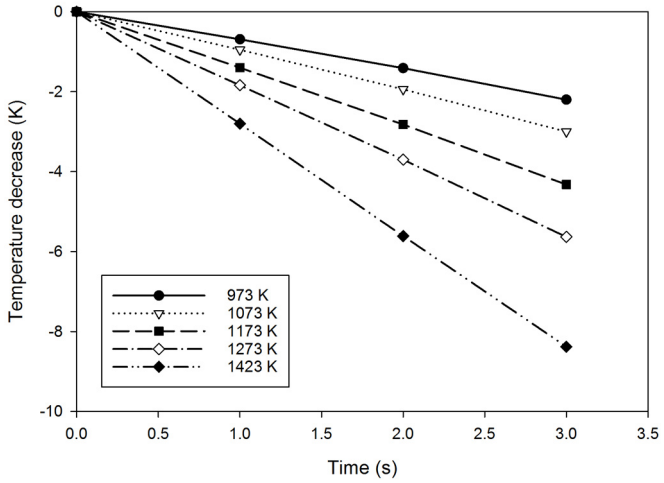

Figure 5.11 Temperature decrease of the sample.

Time (s)	Relative radiance increase (0.85 to 1.1 μm)				
	430.5 K	**454.0 K**	**485.5 K**	**517.0 K**	**580.0 K**
0.00	0.0000	0.0000	0.0000	0.0000	0.000
1.00	5.67E-09	9.58E-09	2.47E-08	5.72E-08	3.97E-07
2.00	1.25E-08	2.24E-08	5.90E-08	1.39E-07	1.01E-06
3.00	3.34E-08	6.30E-08	1.95E-07	5.10E-07	4.09E-06

Table 5.2 Radiance increase of the radiation shield

Time (s)	Relative radiance decrease (0.85 to 1.1 μm)				
	973.0 K	**1073.0 K**	**1173.0 K**	**1273.0 K**	**1423.0 K**
0.00	0.0000	0.0000	0.0000	0.0000	0.0000
1.00	-0.6878	-0.9520	-1.3955	-1.8390	-2.8000
2.00	-1.4122	-1.9420	-2.8233	-3.7047	-5.6133
3.00	-2.1973	-2.9983	-4.3153	-5.6323	-8.3833

Table 5.3 Radiance change of a sample

5.4.8 Temperature deviation between the sample and the blackbody cavity

The sample and the blackbody cavity were placed in approximate thermal equilibrium by design. The actual temperature difference was measured using two thermocouples over the range of 973 to 1423 K. The recorded difference ranged within ±1 K, which equated to the uncertainties (k = 2), $u_{11}(T_{Dev})$, from 0.001 to 0.005.

5.4.9 Positioning

Measurement uncertainty was introduced during sample loading, due to the working distance variations between measurements. Other components were permanently located on the optical table and, therefore, did not contribute to this uncertainty. The positioning error of the housing was estimated to be ± 1 mm, with a maximum uncertainty (k = 2), $u_{12}(L_p)$, estimated to be 0.008.

5.4.10 Expanded uncertainty

For all factors discussed above, the uncertainty of measurements can be calculated by Equation (5.9). From 973 to 1423 K, the maximum expanded uncertainty was 0.0590 (k = 2), as shown in Table 5.4.

	Description	Quantity	973 K	1073 K	1173 K	1273 K	1423 K
Blackbody	Blackbody emissivity, Isothermal	$u_1(\varepsilon_{eff,b})$			0.014		
	Blackbody emissivity, Non-isothermal	$u_2(\varepsilon_{eff,b})$			0.008		
	Blackbody radiance temperature	$u_3(T_b)$	0.048	0.046	0.043	0.041	0.038
Radiometer	SSE for radiometer I	$u_4(L_{SSE})$	0.001*	0.001	0.003*	0.001	0.001*
	SSE for radiometer II	$u_5(L_{SSE})$	0.003*	0.002	0.001*	0.001	2.5×10^{-4}*
	Responsivity correction	$u_6(R)$			0.003		
	Noise for radiometer I	$u_7(S)$	0.014	0.005	0.002	8.0×10^{-4}	2.1×10^{-4}
	Noise for radiometer II	$u_8(S)$	0.016	0.004	0.002	9.0×10^{-4}	3.2×10^{-4}
Radiation shield	Temperature decrease of the sample	$u_9(T_s)$	0.019	0.021	0.025	0.028	0.034
	Temperature increase of the radiation shield	$u_{10}(T_{BC})$	-	-	-	-	-
In-use	Temperature deviation between a sample and a blackbody	$u_{11}(T_{Dev})$	0.003	0.001	0.004	0.005	0.004
	Positioning	$u_{12}(L_p)$			0.008		
	Expanded uncertainty	***U***	**0.059**	**0.054**	**0.054**	**0.053**	**0.054**

Table 5.4 Expanded uncertainty of the instrument (k = 2)

(Note: "*" indicates interpolated data.)

5.5 Results and discussion

5.5.1 Emissivity of SS304

Figure 5.12 shows the emissivity data for SS304 samples from 973 to 1423 K. The lines represent the emissivity of samples without deliberate oxidation and samples oxidised for 60, 120, and 180 minutes. Emissivity of all samples was measured to lie between 0.511 and 0.625 at 937 K and then converged to around 0.800 at 1423 K. The curves show a similar trend for each sample: emissivity increased from 937 to 1073 K, reduced from 1073 to 1173 K, and increased again from 1173 to 1423 K.

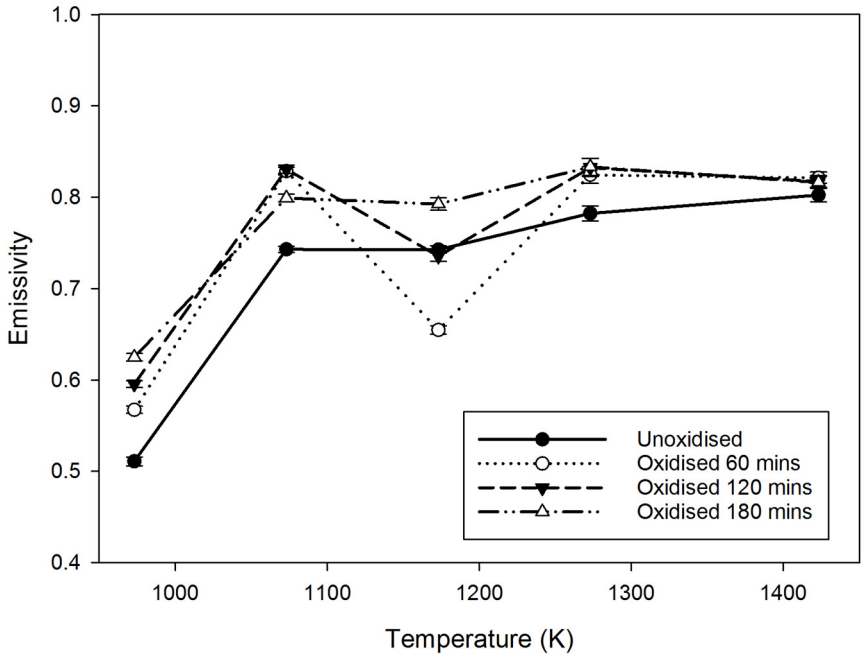

Figure 5.12 Data for emissivity as a function of temperature of SS304. Error bars represent the repeatability of measurements.

Figure 5.13 shows the emissivity data for samples oxidised by different procedures. The symbols represent emissivity measured at 10 minute intervals. Curves were fitted by fifth order polynomial equations for each set of data.

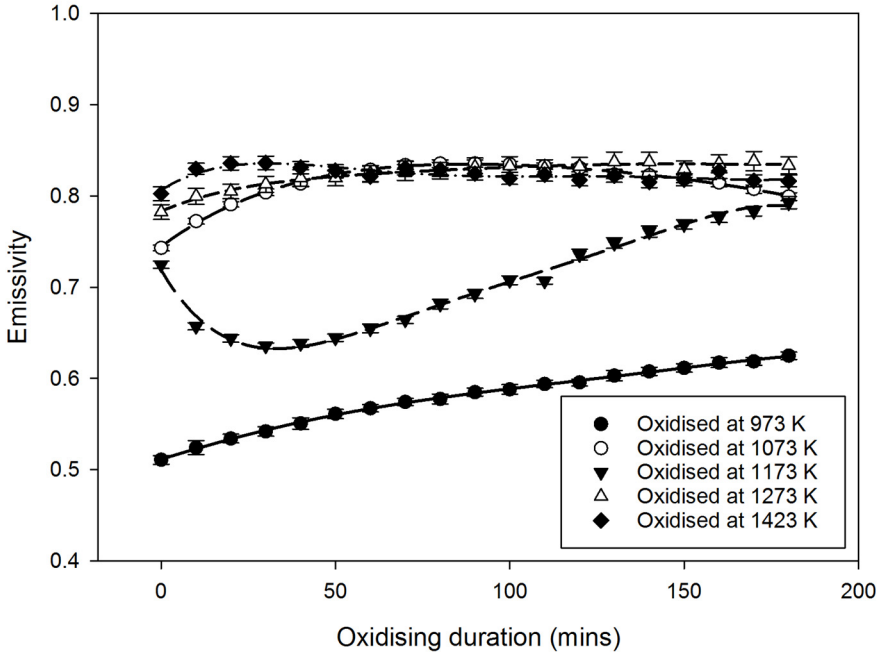

Figure 5.13 Emissivity as a function of oxidising duration for SS304. Error bars represent the repeatability of measurements.

For the sample oxidised at 973 K, emissivity increased from 0.511 to 0.625 continuously; at 1073 K, emissivity increased in the first 80 minutes and then decreased to 0.800 after 180 minutes; at 1173 K, emissivity decreased to 0.636 in the first 30 minutes, and then increased to 0.793; at 1273 K, emissivity increased rapidly to 0.820 in the first 40 minutes and stabilised at around 0.800; at 1423 K, emissivity increased to 0.836 in the first 20 minutes and then fluctuated in the region of 0.800. The error bars in Figure 5.12 and Figure 5.13 represent the repeatability of measurements, which are smaller than the overall expanded uncertainty of the instrument. Each curve shows a unique trend, which suggests a complex emissivity behaviour under different oxidising procedures. Table 5.5 shows the normal emissivity of SS304 under each oxidisation procedure.

At each measured temperature, the variation in emissivity may represent the variation of surface conditions. The surface of a sample oxidised at 1173 K changed dramatically during the measurement. On the other hand, the surface of a sample oxidised a 1423 K was more stable than samples oxidised at other temperatures.

Oxidisation duration (minutes)		0	10	20	30	40	50	60	70	80	90
Oxidisation temperature	973 K	0.511	0.524	0.534	0.542	0.551	0.561	0.567	0.574	0.577	0.585
	1073 K	0.743	0.772	0.791	0.804	0.814	0.824	0.829	0.834	0.835	0.835
	1173 K	0.725	0.657	0.644	0.636	0.638	0.645	0.655	0.664	0.682	0.693
	1273 K	0.782	0.800	0.805	0.813	0.820	0.820	0.825	0.826	0.828	0.832
	1423 K	0.803	0.830	0.836	0.836	0.831	0.828	0.821	0.831	0.829	0.825
Oxidisation duration (minutes)		100	110	120	130	140	150	160	170	180	
Oxidisation temperature	973 K	0.588	0.594	0.595	0.603	0.608	0.612	0.617	0.619	0.625	
	1073 K	0.835	0.833	0.831	0.823	0.823	0.819	0.815	0.808	0.799	
	1173 K	0.708	0.707	0.736	0.748	0.761	0.769	0.777	0.783	0.793	
	1273 K	0.833	0.830	0.832	0.837	0.837	0.829	0.835	0.838	0.833	
	1423 K	0.819	0.823	0.817	0.822	0.815	0.818	0.827	0.817	0.816	

Table 5.5 Normal emissivity of SS304

5.5.2 SEM and EDX results of SS304

Figure 5.14 shows the surface SEM images of SS304 samples used in emissivity measurements. These samples were observed after oxidising for 180 minutes by different procedures. SEM images were taken from areas within the emissivity measurement area. As shown in Figure 5.14 (a), iron oxide islands (as determined by EDX, with area average compositions summarised in Table 5.6) can be observed to grow on top of a Cr and CrMn (white areas) oxide layer; in Figure 5.14 (b), the top oxide layer is continuous and is dominated by Fe oxide that contains a small number of particulates; in Figure 5.14 (c), Fe-rich particles are randomly distributed on an otherwise continuous appearing Cr oxide layer with a number a small particles (pointed out by arrows); in Figure 5.14 (d), iron oxide islands occupy much of the surface, in nickel-enriched or manganese-enriched forms; in Figure 5.14 (e), iron oxide islands grow much bigger, some of them are larger than the SEM image shows, and occupy most of the surface. Separations of some islands can be observed on the top surface.

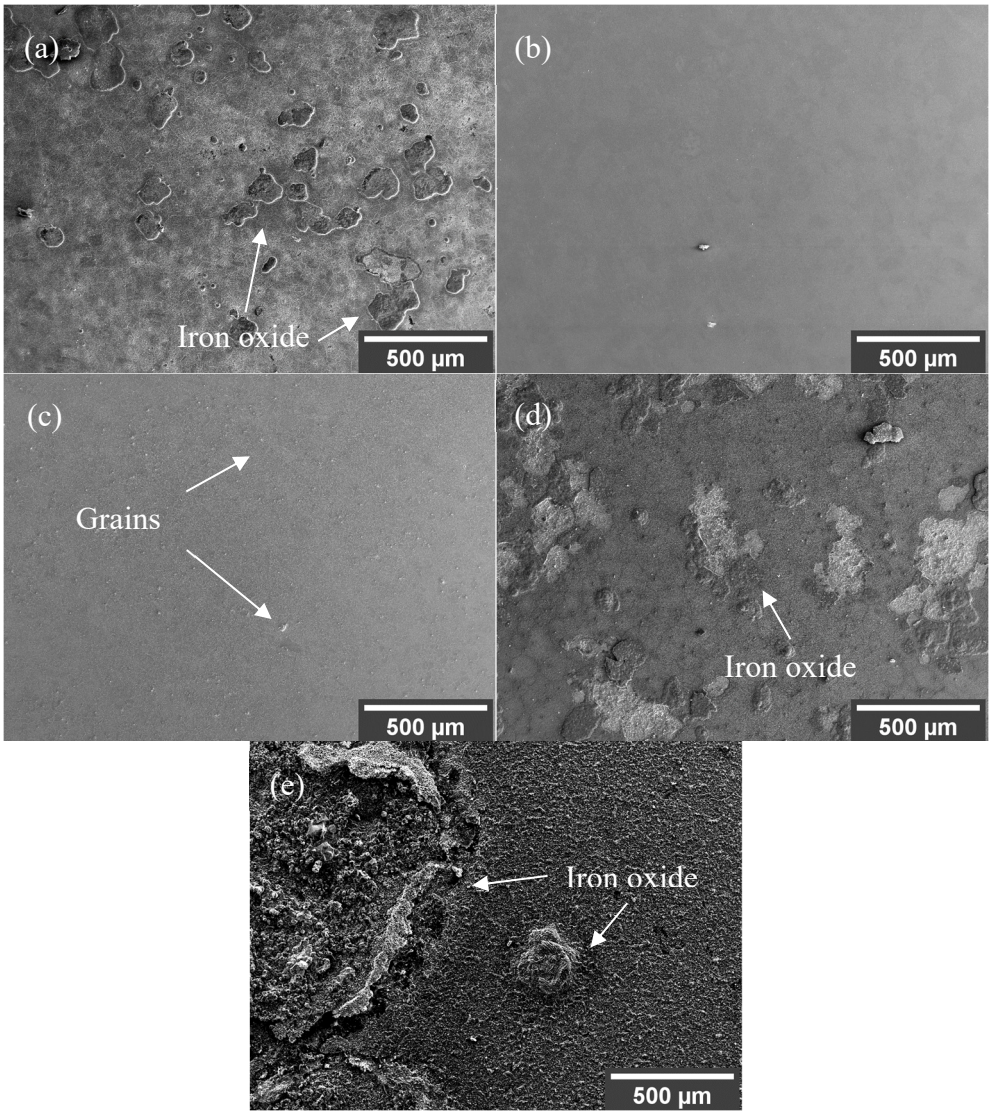

Figure 5.14 Surface SEM images of samples oxidised by different strategies: (a) 973 K, (b) 1073 K, (c) 1173 K, (d) 1273 K, (e) 1423 K.

Sample oxidisation temperature (K)	Atomic weight (%)			
	O	Cr	Fe	Mn
973	45.7	23.1	10.1	7.2
1073	25.3	16.0	39.1	3.0
1173	42.8	21.2	16.7	6.1
1273	49.7	25.4	14.8	7.3
1423	48.3	18.6	13.4	11.9

Table 5.6 EDX results of SS304 samples oxidised under different procedures

5.5.3 Discussions

The emissivity of SS304 measured in this work can be compared with previous measurements published by D. Shi et al. [12] and Y. Liu et al. [22]. At 973 K, emissivity

of measured samples without deliberate oxidation was around 0.510, which is lower than the result of 0.600 measured by Shi. At 1073 K, emissivity without oxidation, measured by the instrument, was around 0.740, which is equivalent to the result of Shi (approximately 0.750). At 973 K, the emissivity of samples oxidised for 180 minutes, measured in this work, was around 0.620, which was slightly lower than the results obtained by Shi (approximately 0.725) and Liu (approximately 0.705). At 1073 K, the emissivity of samples oxidised for 180 minutes was around 0.800, which is equivalent to the result of Shi (approximately 0.790). Considering the results published by Shi and Liu were measured at 1.5 μm, and their samples had a different surface finish and experienced different oxide growth conditions, the measurements obtained by the instrument can be considered to be in agreement with these previously published results.

The emissivity of SS304, as shown in Figure 5.12 and Figure 5.13, was proportional to the oxidising duration at 973 K only. SEM images indicate that increased size of iron oxide islands with increased oxidation time may cause the steady emissivity increase. In contrast for 1273 K for both unoxidised and oxidised samples, their emissivities were measured to be around 0.800 above 1273 K, reaching a stable value after approximately 50 minutes which indicates that their surface conditions became stable quickly at this temperature range. However, the emissivity behaviour was much more complex at 1073 K and 1173 K. At 1073 K, emissivity reached the highest value after 90 minutes and then reduced to around 0.800 after 180 minutes. At 1173 K, emissivity decreased quickly in the first 30 minutes and then increased to 0.780 by the end of the measurement. Notably, the final emissivity values (after oxidation for 180 minutes) at both 1073 K and 1173 K are identical, while the chemical composition (see Table 5.6) is not. What is very similar, however, for both these surfaces is the presence of continuous and fairly smooth oxide layers. Hence, the surface condition of the samples changed dramatically under different oxidising procedures and the observed emissivity changes are likely to reflect changes in oxidation stages/mechanisms, e.g. effects such as island versus continuous coverage, which can be reliably detected with the instrument.

Previous research indicates that the emissivity variation of steel can be associated with the surface oxide condition dynamically [23]. From the measured results, the emissivity of oxidised samples also strongly depends upon oxide processes, including the oxide temperature, duration and rate. The aforementioned analysis, using SEM images and EDX spectra, shows that SS304 oxidises slowly when heated in dry air below 1173 K,

which has an oxide composition of Cr_2O_3 and iron oxide (FeO or Fe_3O_4) [24]. From 1173 to 1273 K, the oxide layer grows at a parabolic rate, with two stages. At the first stage, Cr_2O_3 forms and covers the substrate tightly; at the second stage, iron starts to penetrate the Cr_2O_3 layer from grain boundaries and forms iron oxide particles at a higher oxidisation rate [25]. Above 1273 K, the iron oxide grows quickly and occupies the majority of the top surface, after 20 minutes [26]. At the same time, the enrichment of manganese continuously occurs at high temperatures [27].

The emissivity measurements of SS304 samples in this work, oxidised with each of the aforementioned processes, are in accordance with the oxide behaviour from 973 to 1423 K. This result can support the hypothesis on the relationship between emissivity variations and surface oxidations developed in this work. At 973 K, the increase of emissivity may imply the growth of a Cr_2O_3 layer and the emergence of iron islands. At 1073 K, the decrease of emissivity may imply that iron started to penetrate to the surface after the Cr_2O_3 layer reached its maximum thickness. At 1173 K, the rapid decrease in emissivity may imply that iron penetrated quickly, and then formed iron oxides, leading to increased emissivity. At 1273 K, iron oxides grew fast and then became stable under this condition. At 1423 K, iron oxides grew much bigger and started to separate from the substrate.

In this work, the initial surface condition of the samples could also have had an effect upon the measurements, including the surface roughness and surface damage that may have been introduced during the polishing process. The samples were polished to 3 μm by diamond suspension, though the fluctuation of the surface was greater than the measurement wavelengths of 0.85 to 1.1 μm. In this roughness range, emissivity is highly sensitive to the surface geometry, especially on the surface slope at the micro scale [28]. Meanwhile, the preparation method can also damage the surface grain boundary of the material and change the grain size. Surface damage, such as this, can accelerate the iron oxidisation rate at higher temperatures, leading to the emissivity change [29]. These two factors may introduce new uncertainties for the emissivity measurements of SS304 and should be investigated in more detail in future.

5.6 Conclusion

This chapter introduced the development of an instrument for the measurement of normal emissivity of target samples over a temperature range of 973 to 1423 K under a controlled atmospheric environment. The emissivity of SS304 was measured in oxidised conditions and with samples polished to 3 μm finish. For oxidised samples, their surface topography was measured by SEM and chemical composition was analysed by EDX. The connection between the emissivity change and oxidisation process of SS304 has been discussed thoroughly. During the process of oxidisation of SS304, different oxide islands emerged on the surface of samples at the first beginning, grew to cover the whole surface and started to separate at last, which is accompanied by the variation of emissivity performances.

For the radiation thermometer used in this work, the viewing direction was set to perpendicular to a sample. The measurement area was 14 mm in diameter which was larger than the surface oxide features. Thereby, the measured emissivity can be regarded as the mean value over the whole measurement area. In this case, the result was dependent upon the selection of measurement positions. This impact introduces new uncertainty for measurements, raises the difficulty in tracing emissivity variations within small areas, and leads to the error in further measurements, particularly in temperature controlling processes. It is necessary to develop an instrument to produce the emissivity map of samples to quantify their emissivity performances.

References

[1] J. R. Howell, and R. Siegel, *Thermal radiation heat transfer*, 3rd ed., New York: Hemisphere Publishing Co., 1992.

[2] G. Cao *et al.*, "Spectral emissivity measurements of candidate materials for very high temperature reactors," *Nucl. Eng. Des.,* vol. 251, pp. 78-83, 2012.

[3] J. Huang *et al.*, "Enhanced spectral emissivity of CeO2 coating with cauliflower-like microstructure," *Appl. Surf. Sci.,* vol. 259, pp. 301-305, 2012.

[4] P. Coppa, and A. Consorti, "Normal emissivity of samples surrounded by surfaces at diverse temperatures," *Measurement,* vol. 38, no. 2, pp. 124-131, 2005.

[5] R. Brandt, C. Bird, and G. Neuer, "Emissivity reference paints for high temperature applications," *Measurement,* vol. 41, no. 7, pp. 731-736, 2008.

[6] S. Krenek *et al.*, "A Dynamic Method to Measure Emissivity at High Temperatures," *Int. J. Thermophys.,* vol. 36, no. 8, pp. 1713-1725, 2015.

[7] P. Wang *et al.*, "A new experimental apparatus for emissivity measurements of steel and the application of multi-wavelength thermometry to continuous casting billets," *Rev. Sci. Instrum.,* vol. 89, no. 5, pp. 054903, 2018.

[8] S. Mekhontsev *et al.*, "IR spectral characterization of customer blackbody sources: first calibration results," in *Porc. SPIE Thermosense XXVIII*, 2006, pp. 620503.

[9] A. Gouffé, "Temperature Correction of Artificial Blackbodies, Taking Multiple Internal Diffusion into Consideration," *Optical Review,* vol. 24, pp. 1, 1945.

[10] H. W. Yoon, D. W. Allen, and R. D. Saunders, "Methods to reduce the size-of-source effect in radiometers," *Metrologia,* vol. 42, no. 2, pp. 89-96, 2005.

[11] C.-D. Wen, and I. Mudawar, "Emissivity characteristics of roughened aluminum alloy surfaces and assessment of multispectral radiation thermometry (MRT) emissivity models," *Int. J. Heat Mass Transfer,* vol. 47, no. 17-18, pp. 3591-3605, 2004.

[12] D. Shi *et al.*, "Effect of surface oxidization on the spectral emissivity of steel 304 at the elevated temperature in air," *Infrared Phys. Techn.,* vol. 66, pp. 6-12, 2014.

[13] M. F. Modest, *Radiative heat transfer*: Academic press, 2013.

[14] International Organisation for Standardisation, *Guide to the Expression of Uncertainty in Measurement (GUM)*, Geneva: International Organisation for Standardisation, 1995.

[15] L. del Campo *et al.*, "Combined standard uncertainty in direct emissivity measurements," *Journal of Applied Physics,* vol. 107, no. 11, pp. 113510, 2010.

[16] J. Fischer *et al.*, *Uncertainty budgets for realisation of scales by radiation thermometry*: International Bureau of Weights and Measures (Bureau International des Poids et Mesures), 2003.

[17] P. Saunders *et al.*, "Uncertainty Budgets for Calibration of Radiation Thermometers below the Silver Point," *International Journal of Thermophysics,* vol. 29, no. 3, pp. 1066-1083, 2008.

[18] P. Saunders, and H. Edgar, "On the characterization and correction of the size-of-source effect in radiation thermometers," *Metrologia,* vol. 46, no. 1, pp. 62-74, 2009.

[19] M. Graham, and I. Mohamed, "Size of source effect and temperature uncertainty: II. Low temperature systems," in *Proc. TEMPMEKO*, 1999, pp. 687-692.

[20] J. G. Harris, and Y.-M. Chiang, "Nonuniformity Correction of Infrared Image Sequences Using the Constant-Statistics Constraint," *IEEE Trans. Image Process.,* vol. 8, no. 8, pp. 1148-1151, 1999.

[21] P. Saunders, *Radiation thermometry: fundamentals and applications in the petrochemical industry*: SPIE press, 2007.

[22] Y. F. Liu *et al.*, "Experimental Investigation of Emissivity of Steel," *Int. J. Thermophys.,* vol. 34, no. 3, pp. 496-506, 2013.

[23] S. H. Ham *et al.*, "Relation between emissivity evolution during annealing and selective oxidation of TRIP steel," *Corros. Sci.,* vol. 132, pp. 185-193, 2018.

[24] J. C. Langevoort *et al.*, "On the oxide formation on stainless steels AISI 304 and incoloy 800H investigated with XPS," *Appl. Surf. Sci.,* vol. 28, no. 2, pp. 167-179, 1987.

[25] A. M. Huntz *et al.*, "Oxidation of AISI 304 and AISI 439 stainless steels," *Mater. Sci. Eng., A,* vol. 447, no. 1-2, pp. 266-276, 2007.

[26] I. Saeki *et al.*, "Growth process of protective oxides formed on type 304 and 430 stainless steels at 1273 k," *Corros. Sci.,* vol. 40, no. 8, pp. 1295-1302, 1998.

[27] R. Guillamet *et al.*, "Oxidation of stainless steels (AISI 304 and 316) at high temperature. Influence on the metallic substratum," *Le Journal de Physique IV,* vol. 03, no. C9, pp. C9-349-C9-356, 1993.

[28] C.-D. Wen, and I. Mudawar, "Modeling the effects of surface roughness on the emissivity of aluminum alloys," *Int. J. Heat Mass Transfer,* vol. 49, no. 23-24, pp. 4279-4289, 2006.

[29] J.-H. Kim *et al.*, "Grain-Size Effects on the High-Temperature Oxidation of Modified 304 Austenitic Stainless Steel," *Oxid. Met.,* vol. 79, no. 3-4, pp. 239-247, 2012.

Chapter 6. Design and realisation of an instrument for producing emissivity map

6.1 Introduction

A single-point radiation thermometer only can acquire the emissivity of a selected observation position for each measurement. For an object that has a complex surface condition, such as a piece of heavily oxidised metal sample studied in Chapter 5, the measurement result also depends on the selection of the observation position. In this case, a 2-dimensional emissivity map is required to indicate the emissivity variation across the whole object surface. If a single-point radiation thermometer is used, measurements must be repeated at different locations, and the data must be assembled into a map of the measured positions, which introduces additional uncertainties. Hence, it is necessary to develop a new instrument for producing emissivity maps directly.

An infrared scanning imager, equipped with a Micro-electromechanical systems (MEMS) mirror (Mirrocle Technologies Inc.) and a single-point detector (SPD), is another possible method to produce the emissivity map. This system does not have the problem of the non-uniformity of spectral responsivity and cross-talk due to use of the SPD. The SSE can be calibrated and corrected accurately for each field-of-view (FOV). To develop an infrared scanning imager, based on a MEMS mirror, challenges fall on the design of an optical scanning system.

This chapter introduces the design and realisation of a MEMS mirror based scanning imager, equipped with a Silicon (Si) avalanche photodiode (APD). The instrument was designed for temperature measurements from 500 to 1100 °C. After a careful calibration against the blackbody source, this instrument can be used to produce emissivity maps directly within that temperature range. The FOV of the system was ± 30°, the focal length was 18 mm, and the F-number was 16. At the laboratory testing phase, a sample with

checkerboard pattern was prepared, and its surface emissivity map was produced for proving the instrumental function at the sample surface temperature of 400 °C.

6.2 Methodology

The optical system of a radiation thermometer determines its capability to capture the radiation emitting from an object. As analysed in Chapter 2, a well-designed optical system can bring out a scanning instrument with the high resolution and low SSE. To develop a high-performance instrument, based on a MEMS mirror, the first challenge falls on the design of a good image quality optical system, with full use of the MEMS mirror size and scanning angle. The schematic design of the instrument consisted of two groups of lenses, a MEMS mirror and a Si APD, as shown in Figure 6.1. Rays emitted from a measurand are collected by the first group, folded by the MEMS mirror and focused by the second group, onto the Si APD. The MEMS mirror was 5 mm in diameter, with a maximum scanning angle of ± 5°. The Si APD active area was 0.2 mm in diameter. The FOV was ± 30° by design.

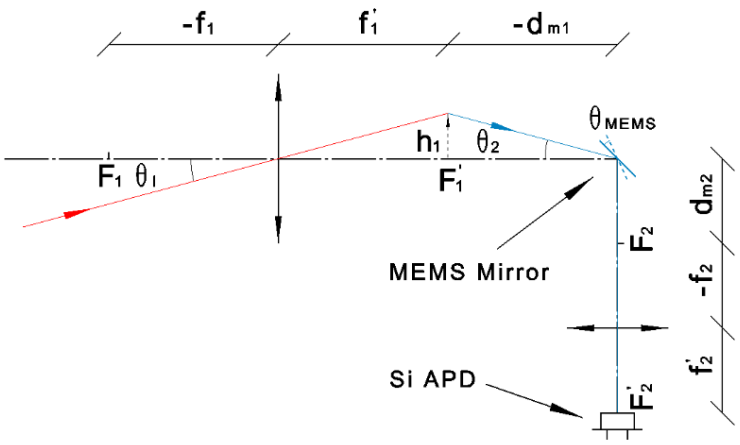

Figure 6.1 Schematic layout of the optical system. The red line represents the chief ray entering the optical system. The blue line represents the ray that leaves the edge of the intermediate image and hits the centre of the MEMS mirror. f_1 is the focal length of the first group of lenses, f_2 is the focal length of the second group of lenses, h_1 is the intermediate image height, d_{m1} is the distance between the MEMS mirror centre to the first focal point in image space, d_{m2} is the distance between the MEMS mirror centre to the second focal point in object space, θ_1 is the incident angle of the chief ray at maximum FOV, θ_2 is the incident angle of the blue ray, and θ_{MEMS} is the half maximum scanning angle of the MEMS mirror.

Distance to target ratio (DTR) (known as field-of-view in radiation thermometer terminology) allows the simple calculation of the area over which any particular radiation thermometer measures. It also quantifies the capability of an instrument to distinguish the thermal features across an object. It is the ratio of the measurement distance to the measurement area upon the measurand, as shown in Equation (6.1). Radiation thermometers are often sensitive to small fractions of radiant power from considerable distances outside their field-of-views and so DTR must be measured for a fraction of the total power. The fraction of enclosed radiant power, by percent (α_E), was defined for our optical system as 90%, giving a DTR of 100:1; which is typical for an industrial radiation thermometer [1]. This led to a focal length for the system of 18 mm.

$$DTR = \frac{f'}{(\alpha_E D_{APD})} : 1 \tag{6.1}$$

where f' is the focal length, α_E is the fraction of enclosed radiant power percent of the measurement area and D_{APD} is the diameter of the APD active area.

Signal-to-noise ratio (SNR) is an important parameter for radiation thermometers, which increases with measurand temperature and ultimately limits the minimum resolvable emissivity [2]. A maximised numerical aperture (low F-number), within design constraints, is desirable so that the system receives a maximum of radiant power from the measurand, achieving highest SNR for any given measurand temperature. The F-number is determined by the smallest optical element, which is the MEMS mirror in the design. The problem posed during the system design process focused on designing a scanning system, with the lowest F-number, whilst meeting the requirements of FOV and DTR. The F-number of the system can be expressed as

$$F - number = \frac{f'}{(f_1'/d_{m1}) \times (D_{MEMS} \times cos\,45°)} \tag{6.2}$$

where D_{MEMS} is the dimension of the MEMS mirror.

The relationship between the effective focal length of a system and each group of lenses, can be expressed as

$$f' = \frac{f_1' f_2'}{d_{m1} + d_{m2}} \tag{6.3}$$

Figure 6.2 shows the relationship between F-number, f_1' and d_{m1} with the consideration of initial conditions of the system, listed from Equations (6.4) to (6.6). The smallest F-number of the system is 16.67 under the paraxial approximation. The system, with this F-number, is practicable for high temperature measurements, when used with the high sensitivity Si APD [3]. To achieve this F-number, f_1' and D_{MEMS} should be selected along the lowest blue edge in the diagram. When the focal length of the first group tends to infinity, the system becomes the combination of a telescope and an objective, which can be adopted as the initial structure for further optimisation.

$$f' = 18\ mm \tag{6.4}$$

$$D_{MEMS} = 5\ mm \tag{6.5}$$

$$\theta_{MEMS} \leq 5° \tag{6.6}$$

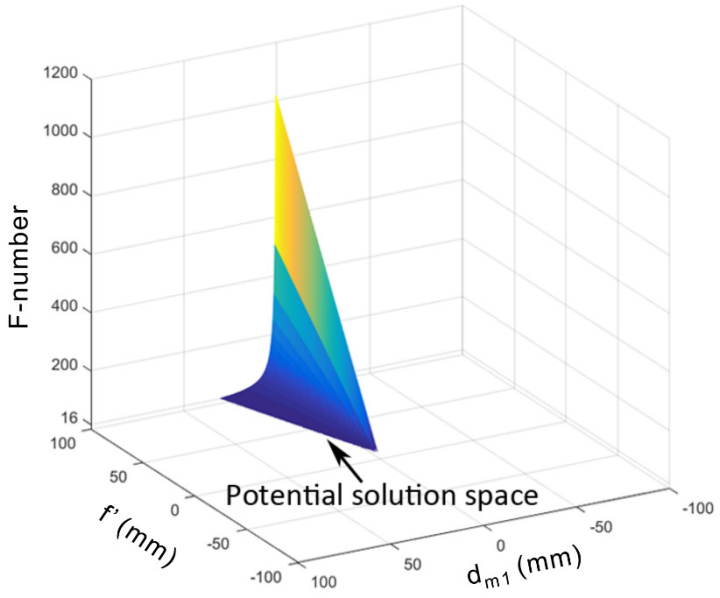

Figure 6.2 Relationship between F-number, f_1', and d_{m1}. The diagram shows the potential solutions of F-number with various f_1' and d_{m1} (within ± 100 mm range). The blue area represents the system with a relatively small F-number, while the yellow area represents the system with a large F-number.

6.3 Optical Design

The instrument was developed for realising two-dimensional scanning, capable of measuring emissivity over the range 500 to 1100 ºC, across the optical waveband from 0.85 μm to 1.05 μm. The design specifications of the optical system are shown in Table 2.1. The design wavelengths were selected as 0.85 μm, 0.95 μm, and 1.05 μm to match the spectral responsivity of the Si APD. The spatial frequency was determined to be 18 cycles per mm, due to the Si APD active area. The incident angle of the chief ray at the MEMS mirror surface was set to 10°, to make use of its full scanning angle of ± 5°. The distance between the mirror and each adjacent element was arranged to be larger than 15 mm, to avoid mechanical interference between those components.

Item	Specification
Field-of-view	± 30°
Focal length	18 mm
F-number	16.67
MEMS mirror scanning angle	± 5°
Total system length	<150 mm
Clear aperture	<30 mm
Wavelength	0.85 μm to 1.05 μm
Frame size	160 × 120 pixels
Frame rate	> 2 frames/second

Table 6.1 Design specifications of the system

The design flow of this system was different from a typical lens design, as shown in Figure 6.3. Firstly, the system was optimised from the initial structure, derived from the aforementioned combination of a telescope and a converging lens. The MEMS mirror was replaced by a virtual intermediate plane. Secondly, the system was reversed and the virtual plane was changed to the MEMS mirror. The system was then, once again, optimised under the multi-configuration mode. Five configurations were set to 0, ±0.707, ± 1.00 of FOV, associated with the scanning angle of the MEMS mirror, respectively. Finally, tolerances were analysed to elucidate the expected system performance, following manufacturing and assembly. Once the system met the requirements at all phases, the design was regarded as ready for fabrication.

The data of the system is shown in Table 6.2. The schematic cross-section view is shown in Figure 6.4. The system was composed of two lens groups, with five elements. The first group ranged from the first surface to the sixth surface. The second group ranged from

the ninth surface to the twelfth surface. The seventh surface was the reflecting surface of the MEMS mirror. The eighth surface was the stop aperture of the lens system. The first group would, alone, perform as a telescope and in the final design is transformed into a converging lens, to balance aberrations under the wide field-of-view.

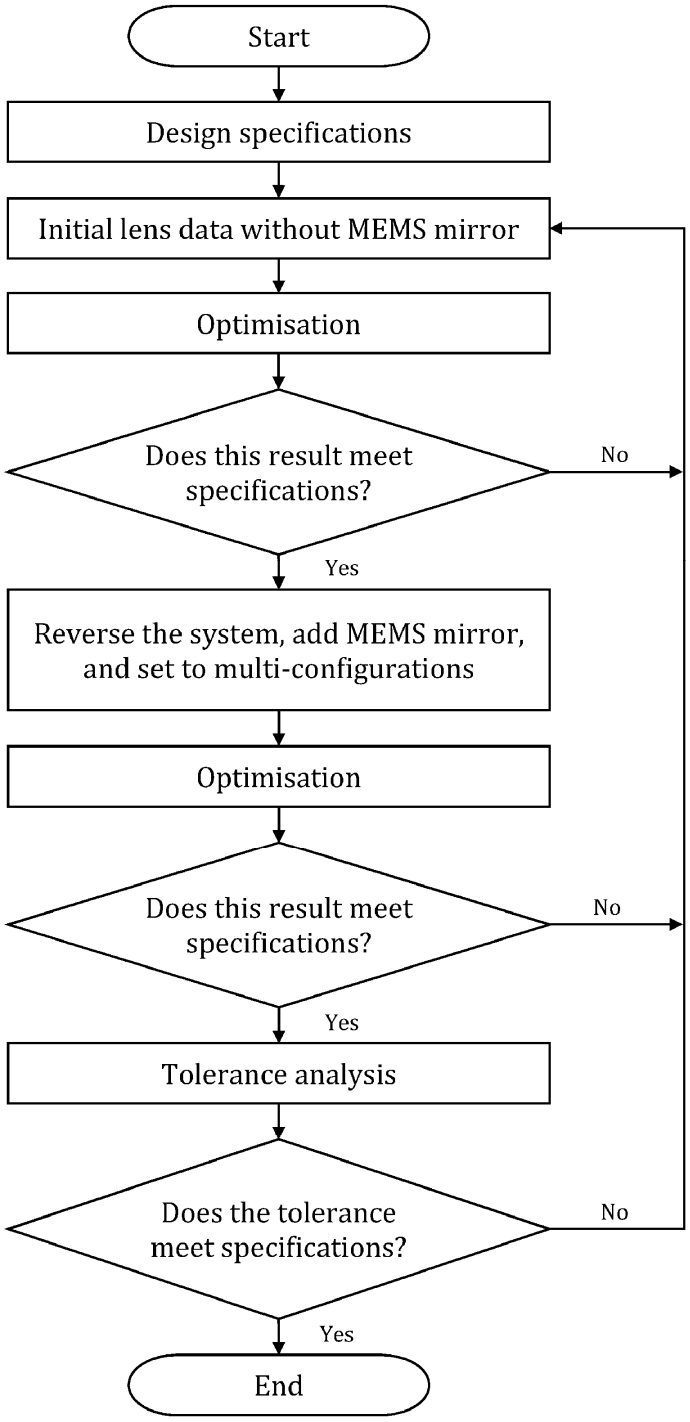

Figure 6.3 Flow chat of the scanning system design.

Surface number	Radius of Curvature (mm)	Surface Separation (mm)	Glass	Semi-Diameter (mm)
1	160.000	3.000	N-LAK9	12.0
2	13.835	25.000		9.0
3	-18.313	4.000	N-SF11	8.0
4	-17.986	25.000		10.0
5	518.418	4.000	N-BAK4	7.5
6	-42.641	21.257		7.5
7	Infinity	24.823	MEMS Mirror	2.5
8	Infinity	3.000	Aperture	1.6
9	9.353	3.000	N-BAK4	5.0
10	25.530	12.000		3.5
11	-5.605	3.000	N-SF11	3.5
12	-13.200	13.766		5.0
13	Infinity	-	Image Plane	0.1

Table 6.2 Data of the system

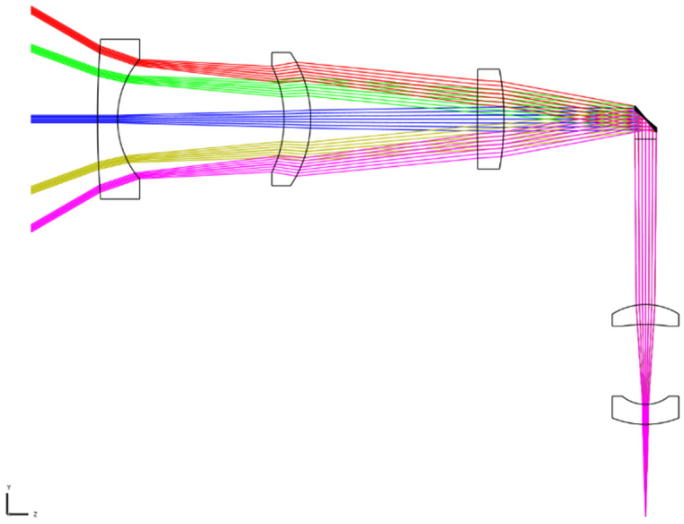

Figure 6.4 Schematic cross-section view of the system.

6.4 Optical System Development

The image quality was analysed for the optical system: included the MTF diagram, spot diagrams, ray fan plots, lateral chromatic aberration, distortion, relative illumination and SSE. Among these analyses, distortion was studied, to understand the relationship between FOV and scanning angle of the MEMS mirror. Relative illumination was

undertaken to reveal the radiant power throughput variation from the centre of the image to its corner. SSE was simulated to estimate the measurement area on a target.

The tolerance sensitivity of the system was analysed before manufacturing. In practice, the image quality of an optical system usually changes after the fabrication, due to manufacturing and assembly errors. These errors mainly arise from three sources: surface deviations, positional changes, and material variations. If lenses are sensitive to these errors, manufacturing tolerances should be specified to a tighter level, leading to increased total cost. If the required tolerances are tighter than is practicable, given the available machine precision, the lens design is impractical and should be optimised again.

The lenses of the system were manufactured and anti-reflection (AR) coated. The entire infrared scanning system was integrated at this phase, including the work of assembling and aligning. This was followed by a laboratory testing phase.

6.4.1 Image quality

Figure 6.5 shows the MTF diagram of the system for FOV of 0°, 20° and 30°. The diffraction limit is shown as a solid black line. The tangential MTF curves are drawn in solid lines, while the sagittal curves are drawn in dash lines. At the spatial frequency of 18 cycles per mm, the MTF value is reduced to 50% for the FOV of 30° in the sagittal direction. MTF values for other FOVs are all larger than 0.5610 at that spatial frequency.

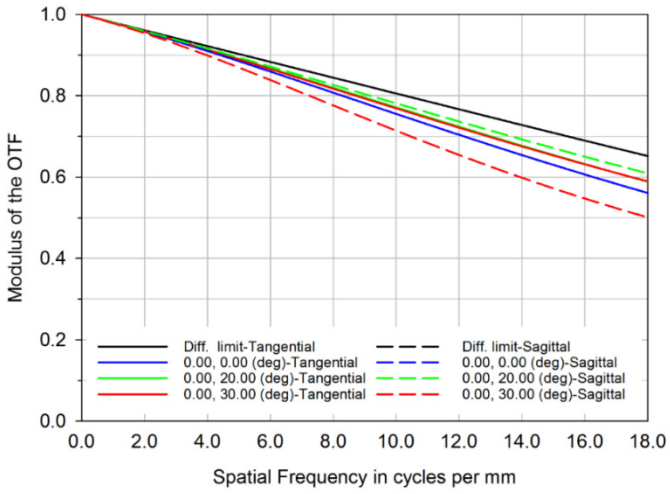

Figure 6.5 MTF diagram of the system. The working distance was set to infinity.

Figure 6.6 shows the spot diagrams of the system, on the image surface. The scale bar of the diagram is 100 µm × 100 µm. The Airy disk is drawn as a solid circle in each graph. The root mean square (RMS) radii for FOV of 0°, 20°, and 30° are 11.074 µm, 7.877 µm, and 10.875 µm, respectively. The geometric (GEO) spot radii are 22.723 µm, 20.417 µm and 24.893 µm, respectively. All spots are similar in extent to the Airy disk, which is 16.52 µm in radius.

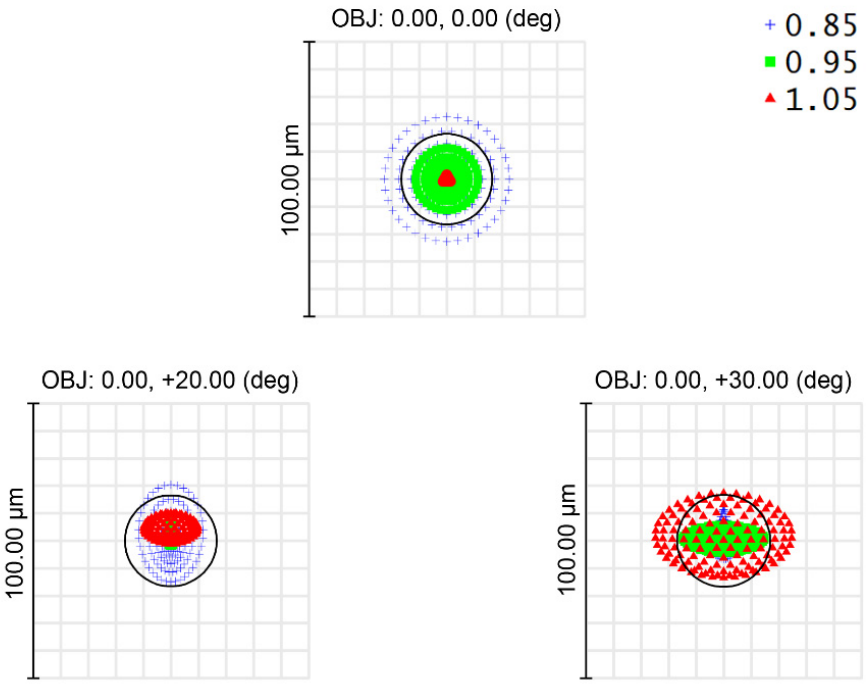

Figure 6.6 Spot diagrams of the system. The working distance was set to infinity.

Figure 6.7 shows the ray fan plots of the system for FOV of 0°, 20° and 30°. The horizontal axis represents the relative pupil height and vertical axis represents the transverse ray aberrations. The scale bar of the plot is 100 µm × 100 µm. The meridional ray aberration plot is shown in left while the sagittal ray aberration plot is shown in right. Slight chromatic spherical aberrations and astigmatisms can be observed in these plots. Aberrations, in general, are less than 30 µm for each FOV.

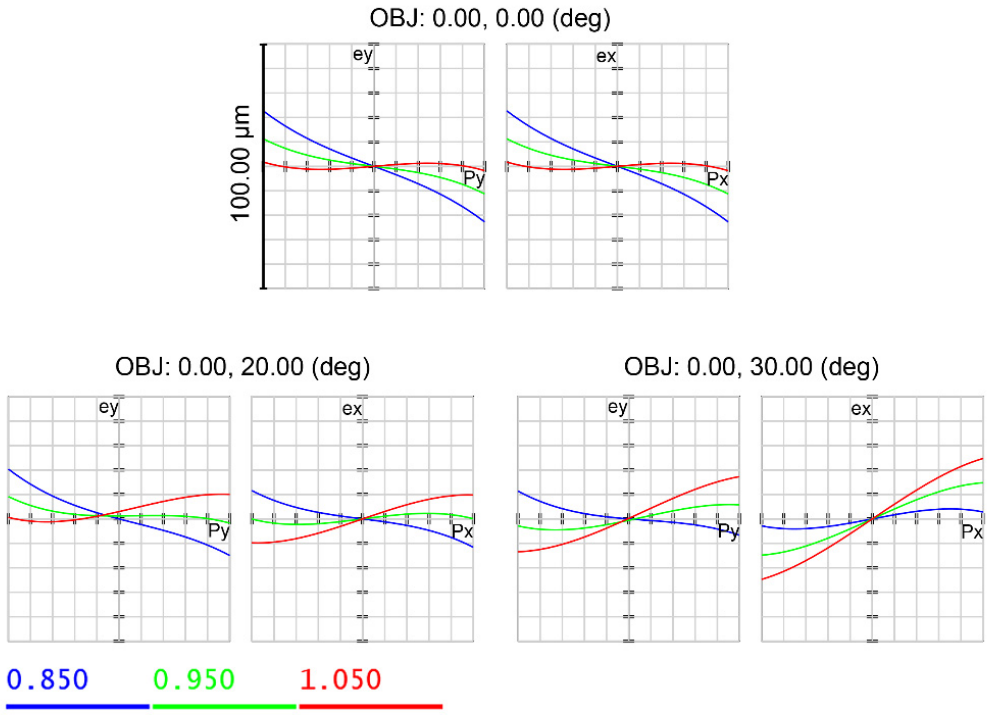

Figure 6.7 Ray fan plots of the system. The working distance was set to infinity.

Figure 6.8 shows the lateral chromatic aberration of the system. The middle wavelength (0.95 µm) was selected as the reference that is drawn in the green curve. The short wavelength (0.85 µm) is drawn in blue, and the long wavelength (1.05 µm) is drawn in red. The largest lateral chromatic aberration occurs at the FOV of 30° for both short and long wavelengths, with the value of 13.879 µm and 14.783 µm, respectively.

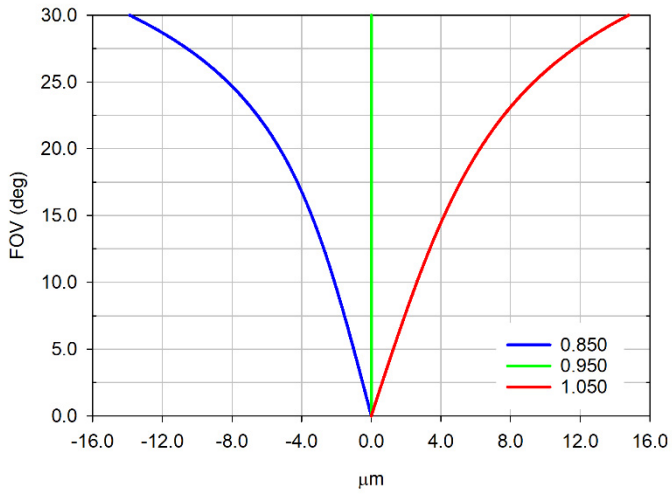

Figure 6.8 Lateral chromatic aberration of the system. The working distance was set to infinity.

Figure 6.9 shows the optical distortion of the system, where the horizontal axis represents the distortion, and the vertical axis represents the FOV from 0° to 30°. For this system, the distortion is defined by the base of the scanning angle of the MEMS mirror, as shown in Equation (6.7). The maximum value is 1.73% which occurs at the FOV of 18°. Previous research indicated that the scanning angle of a MEMS mirror was not linear, and was dependent upon the scanning speed and bias voltage [4]. Considering these factors, the system must be correctly calibrated for the combined distortion, with consideration to both the MEMS mirror non-linearity and optical distortion.

$$Distortion = \frac{FOV_{actl} - FOV_{noml}}{|HFOV|} \tag{6.7}$$

where FOV_{actl} is the actual FOV at each scanning step, FOV_{noml} is the nominal FOV at each scanning step and HFOV is the half field-of-view.

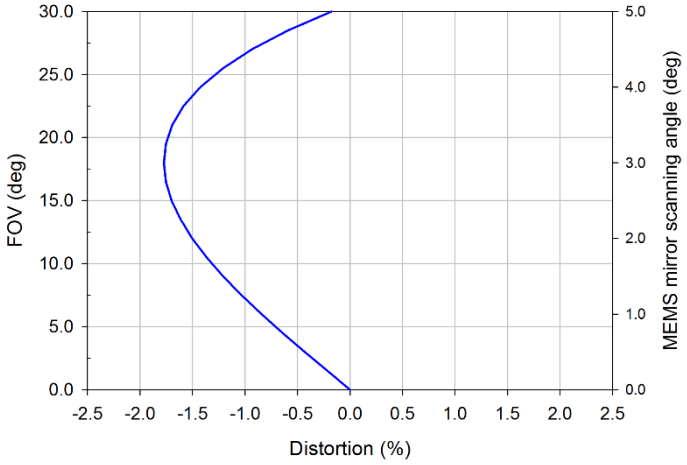

Figure 6.9 Optical distortion of the system. The working distance was set to infinity. The left axis represents the FOV of the system. The right axis represents the scanning angle of the MEMS mirror.

Figure 6.10 shows the relative illumination of the system, where the horizontal axis represents the FOV from 0° to 30°, and the vertical axis represents the relative illumination (%). The relative illumination decreases to 79.2% for FOV of 30°. The decrease will cause non-uniformity in the signal intensity across the image and introduce uncertainties within the measurements. The non-uniformity can be reduced to an acceptable level under the full FOV, with careful calibration and correction.

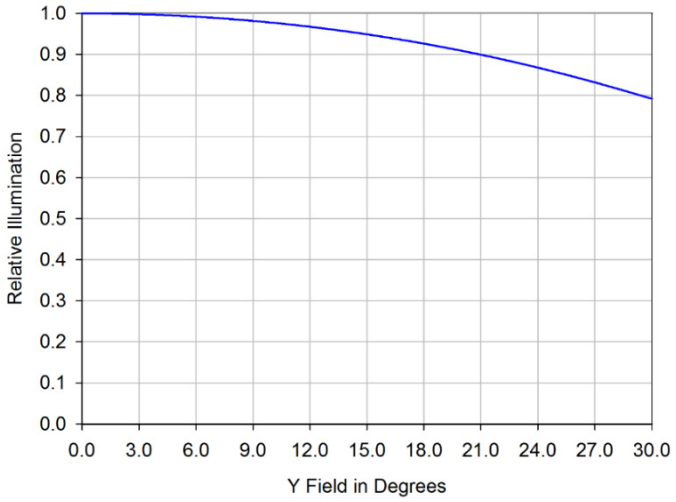

Figure 6.10 Relative illumination of the system. The working distance was set to infinity.

Figure 6.11 shows the simulated SSE, by Zemax OpticStudio, for the FOV of 0° and 30°, based on the direct measurement method [5]. Starting from the design in Figure 6.4, the Si APD was replaced with a circular light source of 0.2 mm in diameter. The working distance was set to 5 meters. The image quality, at this position, can be regarded as being very close to that which would be observed at infinity. Figure 6.11 (a) shows the simulated energy of the measurement area across the Y direction, upon the target. Figure 6.11 (b) shows that the measurement area is smaller than 51 mm in diameter, for FOV of 0° and 30°. The DTR is approximate 98:1, which conforms to the design.

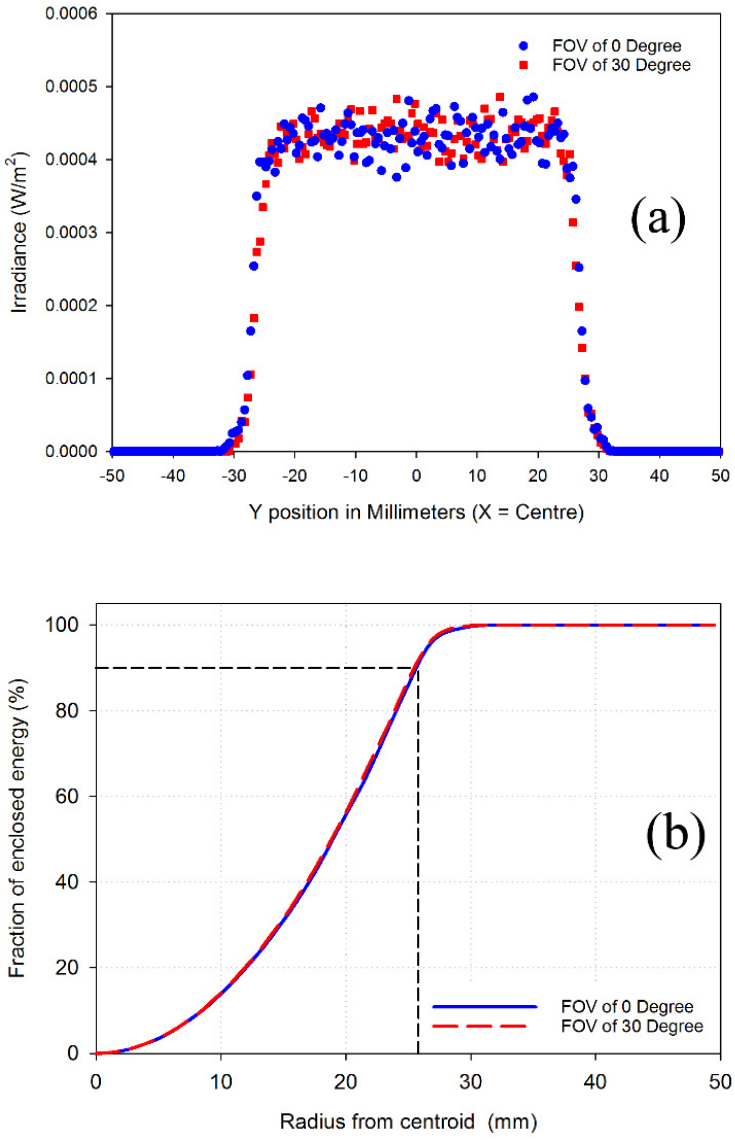

Figure 6.11 Analysis of measurement areas on the target: (a) measurement area extents are shown for FOV of 0° and 30°, (b) SSE is shown for FOV of 0° and 30°. The working distance was set to 5 meters. The total input power was 1 W.

6.4.2 Tolerance analysis

In this work, tolerance analysis was performed by Zemax OpticStudio, in sensitivity mode. A test wavelength of 0.95 μm was selected. The analysis was performed by the Monte Carlo method, with 100 simulations, under criterions of the RMS spot size and average diffraction MTF. Table 6.3 lists the detailed range of tolerance parameters. The MEMS mirror was offered as an off-the-shelf item, without the possibility of re-engineering if for our application. Its curvature radius tolerance was assumed to 0, while

the surface irregularity tolerance was assumed to ± 0.5 fringes. The remaining lenses were assumed with both curvature radius deviation and surface irregularity. All tolerances were specified, based on the achievable machine precision, according to manufacturing experience.

Item	Specification
Radii of curvature of surfaces(fringes)	± 4.0
Irregularity of lens surfaces(fringes)	± 1.0
Irregularity of MEMS mirror surface (fringes)	± 0.5
Centre thickness (mm)	± 0.1
Decentration X of surfaces (mm)	± 0.02
Decentration Y of surfaces (mm)	± 0.02
Tilt X of surfaces (degree)	± 0.02
Tilt Y of surfaces (degree)	± 0.02
Decentration X of elements (mm)	± 0.02
Decentration Y of elements (mm)	± 0.02
Tilt X of elements (degree)	± 0.02
Tilt Y of elements (degree)	± 0.02
Refractive index	± 0.001
Abbe number (%)	± 1.0

Table 6.3 Tolerance parameter ranges (at 0.95 μm)

Table 6.4 shows the results of tolerance analysis for FOVs of 0°, 20°, and 30° at 0.95 μm. The standard deviation (SD) of each subject, computed for 100 times, ranges from 0.001 to 0.032. The deviation between the mean and the design RMS spot size ranges from 2.74% (at FOV of 30°) to 10.63% (at FOV of 20°). The decrease between the mean and the design value of average MTF at 18 cycles per mm ranged from 0.52% (at FOV of 0°) to 3.56% (at FOV of 20°).

FOV (deg)	RMS spot size (μm)			Average MTF (at 18 cycles per mm)		
	Design	Mean/(SD)	Worst	Design	Mean/(SD)	Worst
0	9.347	9.650/ (0.002)	14.743	0.5754	0.5724/ (0.023)	0.4919
20	6.897	7.630/ (0.001)	11.354	0.6035	0.5820/ (0.016)	0.5360
30	10.854	11.151/ (0.002)	16.118	0.5375	0.5327/ (0.032)	0.4232

Table 6.4 Tolerance analysis (at 0.95 μm)

Figure 6.12 shows the RMS spot diagrams for all wavelengths under the worst condition found by the Monte Carlo simulation. The RMS spot size for FOV of 0°, 20°, and 30°

are 17.142 µm, 13.547 µm and 17.366 µm, respectively. Figure 6.13 shows the MTF diagrams for all wavelengths under the worst condition. The minimum MTF value is 0.4114 for FOV of 30° in the tangential direction. The fabricated system can achieve the performance, on average, close to the design specification. The tolerance analysis shows that even under the worst condition, which will occur with a very low probability, the system maintains good image quality.

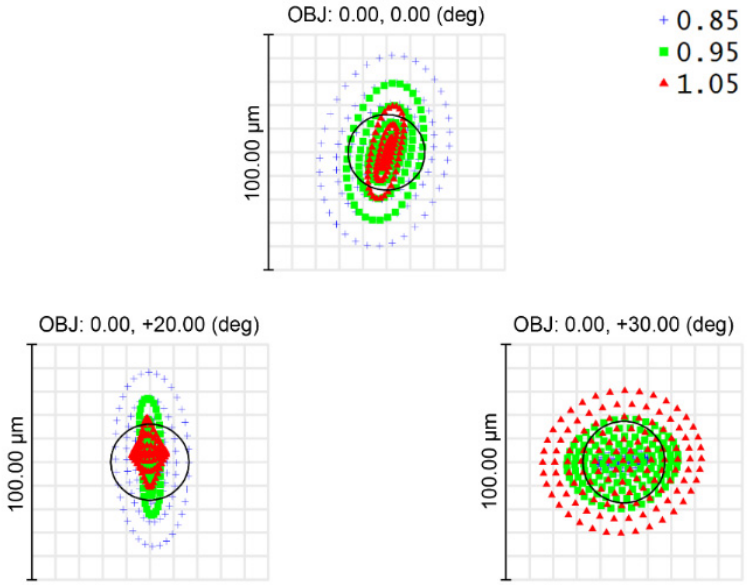

Figure 6.12 The matrix of spot diagrams under the worst condition found during tolerance simulations. The working distance was set to infinity.

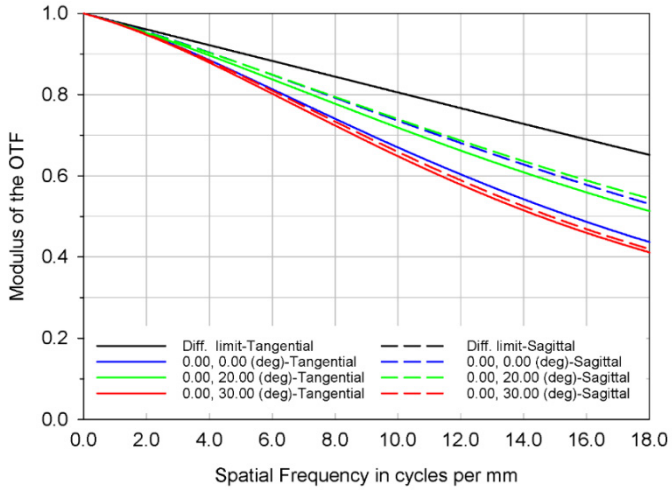

Figure 6.13 The MTF diagram under the worst condition found during tolerance simulations. The working distance was set to infinity.

6.4.3 Optical system realisation

Figure 6.14 shows the cross-section diagram of the MEMS unit. The optical lenses were manufactured by Zhenjiang Acos Optoelectronics Technology Co., Ltd (China). The mechanical parts were machined by Shanghai Gangqun Industrial Co., Ltd. (China). Two groups of lenses were fixed in the lens housing beside the MEMS mirror, which was screwed onto a bracket. The Si APD was mounted on a three-dimension translation stage (not drawn in the diagram). All metal parts were made from aluminium alloy and anodised in black. All optical elements, including the MEMS mirror window, were coated with antireflection coating, effective from 0.85 μm to 1.05 μm. The MEMS mirror was adjusted to match its centre to the optical axis. Although the system was designed with an infinity working distance, it could be focused closer, by changing the distance between the lens and the APD.

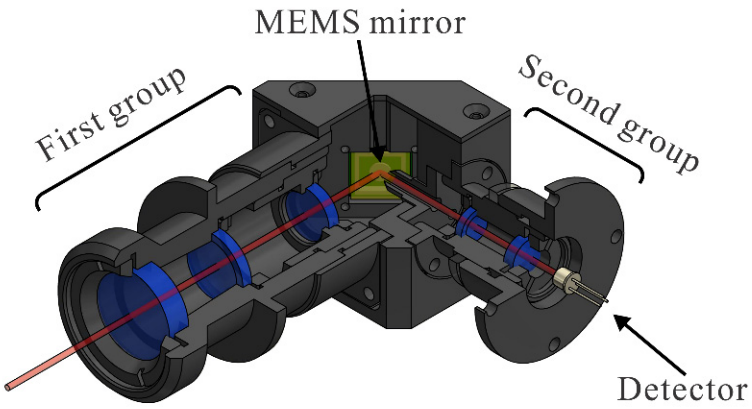

Figure 6.14 Cross-section diagram of MEMS unit. The red line indicates the optical axis.

6.5 Experiment on Emissivity Mapping

At the laboratory testing phase, the instrument was used to produce the emissivity maps of samples heated by a hotplate. The results will help to understand the basic function of the instrument and determine the practical measurement procedures.

6.5.1 Experimental setup for mapping emissivity

Figure 6.15 shows the schematic diagram of the emissivity mapping instrument under the first testing stage. A prepared sample was placed at the centre area of a hotplate (SCILOGEX MS7-H550-Pro, 550 °C Max.). A thermocouple (TC Direct 408-053 Class-1) was inserted into the sample. The distance between the sample surface and thermocouple position was approximately 2 mm. The signal from the thermocouple was interpreted by a thermocouple readout module (Fluke T3000 FC) to indicate the sample surface temperature. The MEMS unit was mounted on an optical breadboard above the hotplate, looking at the sample vertically. The working distance between the sample surface and the MEMS unit was adjusted to 100 mm. A 18 mm in diameter aperture was fixed between the sample and the MEMS unit to block the background radiation emitted from the heating area of the hotplate. The photodiode, with its readout circuits PCB, was mounted on a translation stage (Thorlabs XR25C), allowing a quick focus of the system. The data acquisition system was used to record the electrical signals produced by the circuit at the measurement temperature.

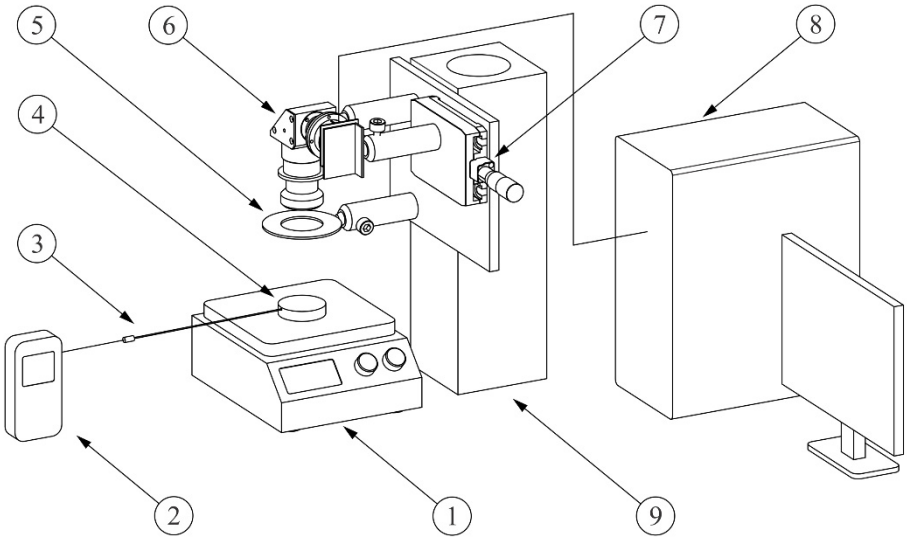

Figure 6.15 Schematic diagram of emissivity mapping apparatus: hotplate (1); thermometer readout module (2); thermocouple (3); sample (4); aperture (5); MEMS unit (6); one-axis translation stage (7); data acquisition system (8); optical post (9).

When the hotplate was set to 525 °C to heat an Aluminium sample, the thermocouple indicated that the sample surface temperature was approximately 400 °C. The temperature drop was due to the heat resistance occurring on the interface between the hotplate and the sample and the heat transfer from the sample to its surroundings. To offer a better signal-to-noise ratio at the interested temperature, the Si APD was replaced by an extended indium gallium arsenide (Ex-InGaAs) photodiode (Hamamatsu G12183-010K), with spectral responsivity of 0.9 to 2.6 μm. The mismatch between the spectral responsivity of the Ex-InGaAs photodiode and the transmissivity of the lens AR coating may increase the SSE, which should be measured and transferred to the uncertainty. In general, the usage of Ex-InGaAs photodiode can simplify the heating apparatus and offer a reliable emissivity measurement to verify the function of the instrument, which will benefit the further measurements at higher temperatures. The active area of the photodiode was limited to 0.35 mm in diameter by using a field stop. The instrument was calibrated by a blackbody furnace at 400 °C. The signal output by the instrument was recorded as the reference value for computing emissivity.

6.5.2 Sample preparation and measurement procedure

To evaluate the capability of the instrument for distinguishing emissivity variations across the measurement area, a sample with checkerboard pattern was prepared, as shown in Figure 6.16. The substrate of the sample was Aluminium alloy 6082. The dimension of the substrate was machined to 50 mm in diameter by 10 mm in depth. A 1.5 mm diameter hole was drilled 2 mm from the top surface of the sample for insertion of the thermocouple. The depth of the hole was 25 mm to allow the thermocouple tip to reach the sample centre. The top surface of the substrate was ground by P240 sandpaper and brushed by HiE-Coat 840M paint. After that, the surface was engraved by laser to remove the unwanted paint to form the checkerboard pattern. The black square was covered by the HiE-Coat 840M pant whilst the grey square was engraved. The dimension of each black square was 4.5 × 4.5 mm.

Figure 6.16 Picture of the sample with checkerboard pattern. The black area was covered by HiE-Coat 840M paint whilst the grey area was the engraved area.

Before starting the measurement, the prepared sample was positioned on the centre of the hot plate. The working distance between the sample top surface to the first lens surface of the MEMS unit was adjusted to approximately 100 mm. The thermocouple was inserted into the sample once the sample was loaded to the correct position. The hot plate was set to 525 °C whilst the thermocouple indicated the sample surface temperature was approximately 400 °C. After the sample had stabilised at the measurement temperature for 30 minutes, the system was powered on and the MEMS mirror was operated to complete the scanning process. The data was recorded by the data acquisition system. The emissivity map was produced after comparing the signals of the sample and the blackbody, which was recorded in the calibration phase. Figure 6.17 shows the photo of the experimental instrument for mapping emissivity at the sample surface temperature of 400 °C.

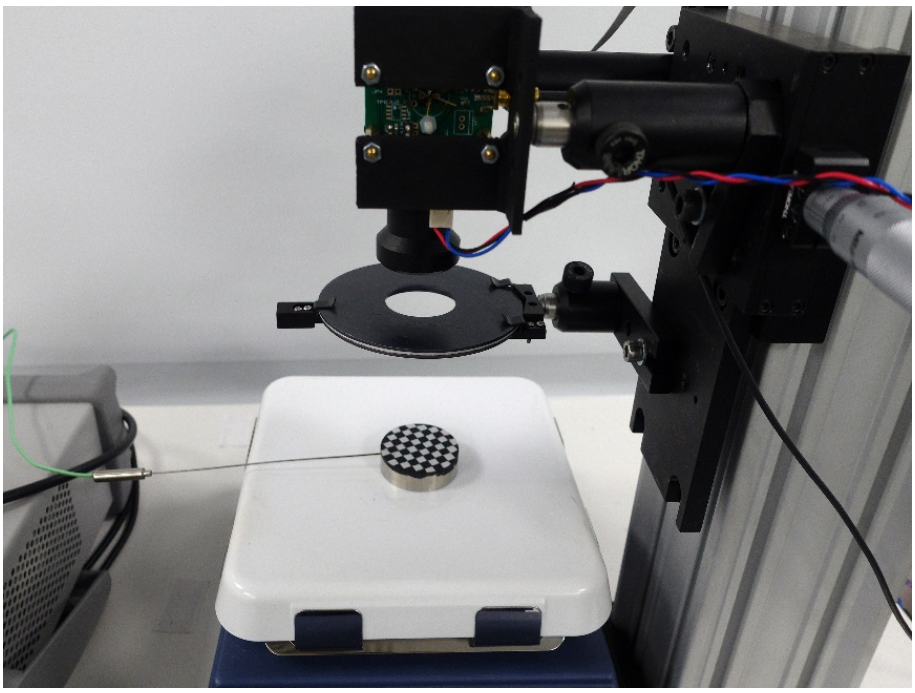

Figure 6.17 Picture of the experimental instrument for mapping emissivity.

6.6 Results and Discussion

6.6.1 Emissivity map of the prepared sample

Figure 6.18 shows the emissivity map of the prepared sample at 400 °C with spectral range of 0.9 to 2.6 μm. The figure was rotated and cropped to the frame of 120 × 100 pixel, which equalled the scanning angle of 39.6° × 33.0°. The emissivity ranges from 0 to 1 which was represented by the colour from purple to red, respectively. The red area indicates the places covered by HiE-Coat 840M paint whilst green indicates the places engraved for removing the paint. Figure 6.19 shows the emissivity distribution of the sample with contour outlines.

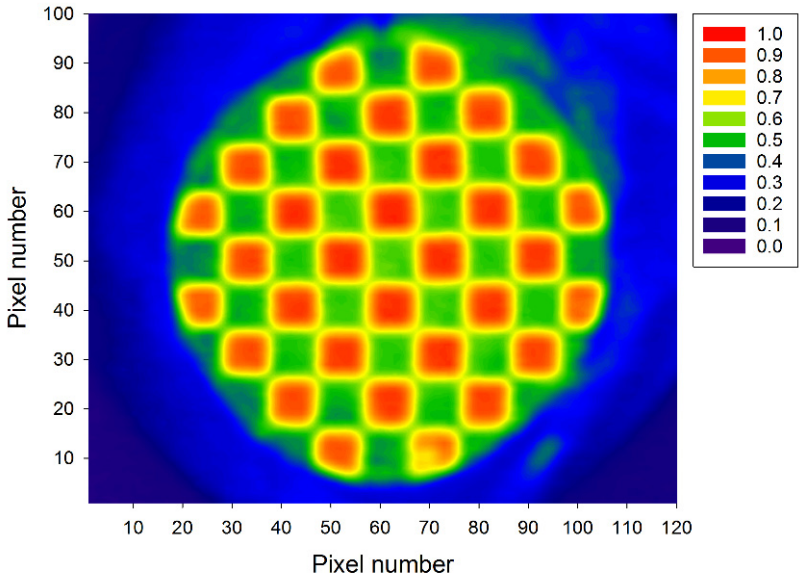

Figure 6.18 Emissivity map of the prepared sample with checkerboard pattern. The figure represented the scanning angle of 39.6° × 33.0°. Red area represents the high emissivity range whilst blue area represents the low emissivity range.

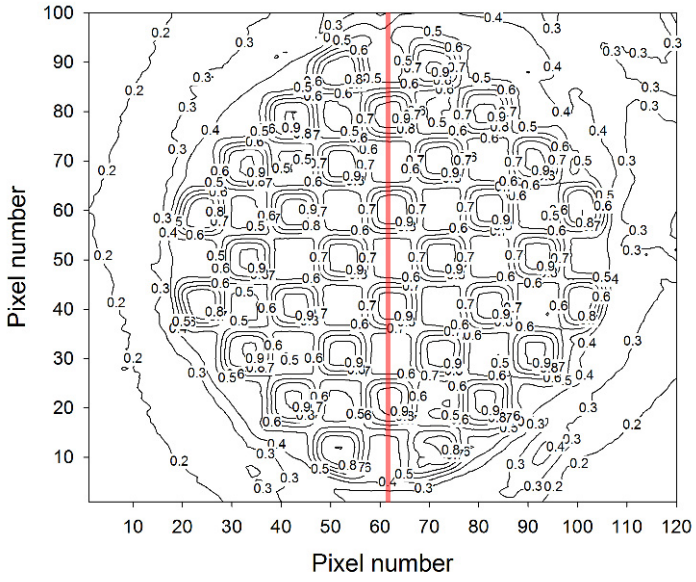

Figure 6.19 Emissivity map of the prepared sample with contour outlines. The figure represented the scanning angle of 39.6° × 33.0°. The red line indicates the centre line (column 61 in the figure) of the sample.

Each pixel of the map can be regarded as an independent emissivity measurement undertaken by a single-point radiometer. Therefore, the measurement error can be traced and compared. Figure 6.20 shows the emissivity fluctuation of the whole observation

scene between two measurements. The largest deviation is 0.027 which is shown in the red area in the figure. The fluctuation of most of observation area were lower than 0.015 during measurements, showing as the blue to purple area.

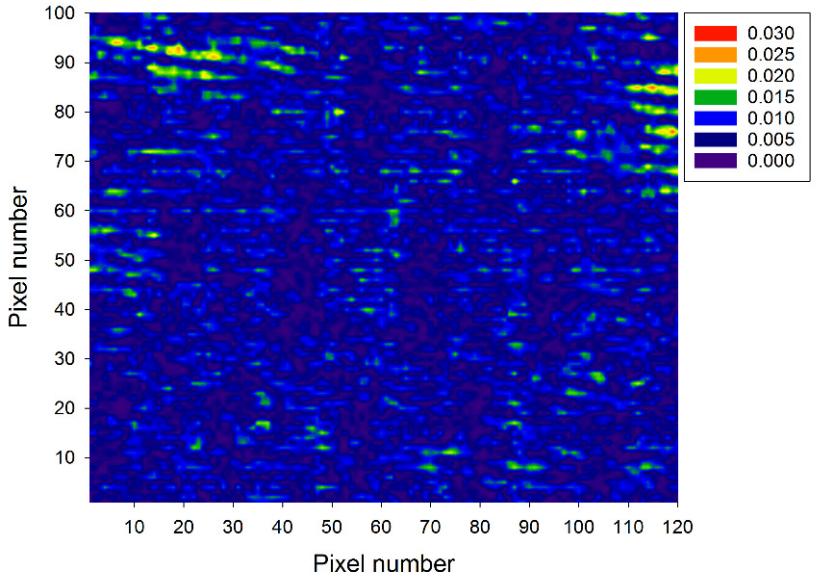

Figure 6.20 Emissivity fluctuation of the observation scene at 400 °C between two measurements. The figure represented the scanning angle of 39.6° × 33.0°.

Figure 6.21 shows the cross-section emissivity distribution of the centre line of the sample (column 61), indicated by the red line in Figure 6.19. The black solid line represents the mean emissivity value between two measurements whilst the red and blue lines represents the upper and lower emissivity range, respectively. Four peaks of the curve indicate the high emissivity area of the sample, where it is covered by HiE-Coat 840M paint. The highest emissivity value is 0.962, indicated by the pixel of (61, 63). The emissivity of the rest peaks ranges from approximate 0.920 to 0.960. Three valleys of the curve indicate the emissivity of the engraved area on the sample. The emissivity of these valleys falls with the range of 0.500 to 0.600.

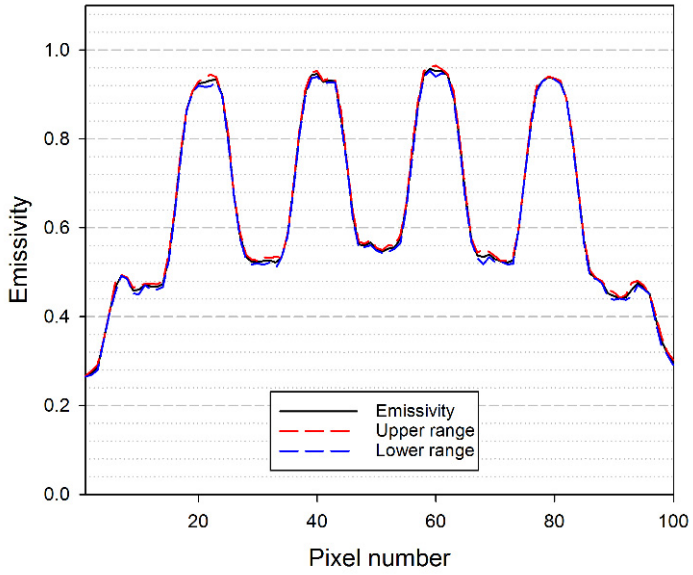

Figure 6.21 Cross-section emissivity distribution of the centre of the prepared sample.

6.6.2 Uncertainty analysis

The uncertainties of the experimental instrument derive from four sources: the radiance temperature error, size of source effect, the electronic noise, and drift. The combined standard uncertainty $u_c(x)$ is expressed by Equation (6.8). The expanded uncertainty is expressed at approximately the 95% confidence level using a coverage factor of k = 2.

$$u_c(x) = \sqrt{\sum_{i=1}^{N} [u_i(x)]^2} \tag{6.8}$$

The instrument was pre-calibrated with a blackbody furnace, LANDCAL P550P. The radiance temperature error of the furnace at 400 °C is lower than ± 0.2 ºC, leading to the uncertainty, $u_1(T_b)$. On the other hand, the radiance temperature of the sample's surface was measured by a classic 1 thermocouple. The error range of the thermocouple at 400 °C is ± 1.6 °C, leading to the uncertainty, $u_2(T_s)$. The mismatch of radiance temperature between the sample surface and blackbody furnace introduces the uncertainty to measurements.

Size of source effect (SSE) describes the phenomenon that a radiation thermometer measures radiation from the region outside of its nominal measurement area. Therefore,

the radiation thermometer receives the radiant power beyond the nominal measurement area. For this MEMS unit, all lenses were deposited AR coating at the waveband of 0.85 to 1.05 μm, which generates a larger portion of reflection at a wider waveband of 0.9 to 2.6 μm, leading to the increase of SSE. At 400 °C, the 3 mm in diameter measurement area can enclose 90% radiant energy, and, thereby, the uncertainty, $u_3(L_{SSE})$, caused due to SSE was estimated to be 0.053 (k = 2), which can be regarded as the confidence resolution of 3 mm in dia.

The radiation thermometer output fluctuated over the course of the measurement due to the electronic noise and drift of the photodiode-amplifier circuit, adding additional uncertainty to the measurement. At 400 °C, the uncertainty (k = 2) due to electronic noise, $u_4(S)$, was 0.030 and due to drift, $u_5(S)$, was 0.077.

The overall uncertainty of the measurements can be calculated by using the Equation (6.8) with the consideration of all uncertainty components discussed above. The expanded uncertainty (k = 2) at 400 °C, with the spectral range of 0.9 to 2.6 μm, was estimated to be 0.101, as shown in Table 6.5.

Description	Quantity	Uncertainty (k = 2)
Blackbody radiance temperature	$u_1(T_b)$	0.003
Thermocouple	$u_2(T_s)$	0.026
Size of source effect	$u_3(L_{SSE})$	0.053
Electronic noise	$u_4(S)$	0.030
Drift	$u_5(S)$	0.077
Expanded uncertainty	$\boldsymbol{U}$	**0.101**

Table 6.5 Expanded uncertainty at 400 °C (k = 2)

6.6.3 Discussion

The prepared sample offers the checkerboard emissivity pattern to evaluate the function of the experimental instrument. The high emissivity area represents the HiE-Coat 840M painted squares, as shown in Figure 6.16. The emissivity of black squares distributed along the centre line of the sample ranges from approximate 0.92 to 0.96 at 400 °C. These results agree with the previous publications [6] and the measurements introduced in chapter 4. The emissivity of grey areas of the sample ranges from 0.500 to 0.600, which is higher than the emissivity of Al6082 measured in chapter 4. The emissivity

enhancement of engraved squares is due to the residual of HiE-Coat 840M paint on those areas. When the observation area of a scanning locates on the boundary of painted and engraved areas, the emissivity is in direct proportion to these two areas, showing as the blurred boundaries in Figure 6.18.

The results shown in Figure 6.18, Figure 6.19, and Figure 6.21 indicate that the emissivity at the centre area of the sample is slightly higher than that at the marginal area. This phenomenon may be caused by two reasons. On one hand, the surface temperature may decrease from centre to marginal area of the sample; on the other hand, the radiant power measured by the instrument may be modulated by the optical system, demonstrating a decrease from the centre to the marginal area, as shown in Figure 6.10. The second problem can be resolved by a careful non-uniform correction across the full FOV.

In Figure 6.18, the emissivity map of the sample is bent from the centre with approximate 2 pixels in vertical direction, which indicates existence of the non-symmetric distortion of the measurements. The non-symmetric distortion may be caused by the misalignment between the detector and the optical system. Meanwhile, the system may also exist the symmetric distortion over the whole FOV, as indicated by Figure 6.9. In general, the distortion can be corrected by a precise alignment and calibration based on the design result.

6.7 Conclusion

This chapter introduced the design and realisation of an emissivity mapping instrument, with the integration of a MEMS mirror device. The instrument was designed for measurements at the temperature from 500 to 1100 °C, at the wavelength from 0.85 μm to 1.05 μm. The optical system was designed to fully utilise the 5 mm diameter mirror and its ± 5° scanning angle, to achieve the FOV of ± 30° and the distance to target ratio of 100:1. At the testing phase, the instrument was used to map emissivity of a sample prepared with checkerboard pattern. The measurement uncertainties were measured and analysed thoroughly. The results indicate that the instrument is capable of producing reliable emissivity maps of objects, which will contribute to trace the emissivity variations, and thereafter, offer a better understanding of emissivity behaviour of objects with complex surface conditions.

References

[1] Land Instruments International, "SPOT Brochure-Specification and design," [Online]. Available: https://www.ametek-land.com/-/media/ameteklandinstruments/documentation/products/fixedspotnoncontactthermometers/spot/ametek_land_spot_brochure_marcom0355_rev_15.pdf, 2017.

[2] M. Vollmer, and K.-P. Möllmann, *Infrared thermal imaging: fundamentals, research and applications*: John Wiley & Sons, 2017.

[3] M. J. Hobbs *et al.*, "Quantitative thermal imaging using single-pixel Si APD and MEMS mirror," *Opt. Express,* vol. 26, no. 3, pp. 3188-3198, Feb 5, 2018.

[4] V. Milanovic, "Linearized gimbal-less two-axis MEMS mirrors," in *Optical Fiber Communication Conference*, 2009, pp. JThA19.

[5] H. W. Yoon, D. W. Allen, and R. D. Saunders, "Methods to reduce the size-of-source effect in radiometers," *Metrologia,* vol. 42, no. 2, pp. 89-96, 2005.

[6] Aremco Products Inc., "High Temperature Specialty Coatings. Valley Cottage," [Online]. Available: www.aremco.com/wp-content/uploads/2015/06/TechNote-840-M.pdf, 2015.

Chapter 7. Conclusion

Emissivity is an essential quantity representing the radiative properties of materials that must be prior measured precisely to undertake accurate and traceable measurements for radiation thermometry, including non-contact temperature measurements and surface property characterisations. This work has successfully presented the realisation and validation of three emissivity measurement instruments, developed with low measurement uncertainties according to the Guide to Uncertainty of Measurement (GUM) [1], to undertake continuous studies on emissivity in temperature from 200 to 1150 °C. The first instrument was developed to study the inherent advantages and drawbacks of the direct and indirect radiometric methods. The second instrument was developed with a controlled atmospheric system to study the impact on emissivity variations during the oxidation process. The third instrument was developed for producing emissivity maps over the scene of interest to quantify the localised emissivity distribution of measurands with complex surface conditions, such as a heavy oxidised surface. These instruments aim to offer accurate and traceable emissivity references for use in radiation thermometry, particularly the non-contact temperature measurements to the International Temperature Scale of 1990 (ITS-90).

To analyse the uncertainty of direct and indirect methods quantitatively, this work presented an emissivity measurement instrument equipped with a pair of cups coated by Vantablack® and gold respectively. The instrument can undertake the measurement of emissivity of opaque materials from 200 to 450 °C in the spectral range of 2.1 to 2.5 μm. Three different measurement methods were studied and compared by using this instrument, including black-cup (direct), gold-cup (indirect), and dual-cup (in-situ direct) methods. The performance of the instrument has been validated by studying the materials with the emissivity ranging from 0.05 to 1.0, including aluminium alloy 6082 (Al6082), stainless steel 304 (SS304), and HiE-Coat 840M paint. The uncertainties corresponding to each measurement method have been studied quantitatively. Based on this information, the most suitable measurement range of the direct and the indirect methods

has been determined. The gold-cup method is better for the measurement of low emissivity materials, whereas the black-cup and dual-cup methods are suitable for all other emissivity ranges. The analysis offers the knowledge in the selection of appropriate methods for offering the most suitable emissivity measurement range, with respect to prior properties of materials.

This work firstly achieved the Monte Carlo simulation on the ray tracing of a gold-cup. This method is a key technique for investigating the relation of emissivity enhancement and the geometric properties of a gold-cup, such as the shape, the opening hole size and the gap between the sample and the gold-cup. The related studies can be used for solving the problem on the optimisation of gold coated reflectors in temperature measurements which has existed since the invention of this method.

A new emissivity measurement method, dual-cup method, has been developed based on the studies of gold-cup and black-cup methods. The dual-cup method directly compared the radiant power from the same sample when it is covered by a black-cup and by a gold-cup. This method does not require a separate blackbody as the reference. Thus, the error due to the mismatch between the sample's surface temperature and the blackbody radiance temperature can be eliminated. The dual-cup method has a lower uncertainty than a conventional direct method for emissivity measurements.

The radiative properties of an object are directly affected by its surface conditions, including chemical composition and surface roughness. During the process of oxidation, the surface condition of an object continuously changes due to the variation of its environment, leading to the emissivity change respectively. An emissivity measurement instrument with a controlled atmosphere has been presented in this work to study the impact on emissivity performances due to the surface condition change. The instrument can undertake measurements across the temperature range from 700 to 1150 °C and spectral range from 0.85 to 1.1 μm; this range is matched to the majority of high temperature radiation thermometers. This instrument offers the capability for industry to measure the emissivity with the consideration of the actual atmosphere and to trace the emissivity change due to the oxidation process.

Another achievement in this work is the accurate emissivity measurements of various opaque materials (i.e. metals and paints) completed by three instruments. Particularly, the emissivity of SS304 has been measured with different oxidation procedures. The

surface topography of oxidised SS304 has been measured by SEM and the chemical composition was analysed by EDX. The observations in this work present the connection between emissivity variations and the surface composition changes of SS304 during the oxidation process. Measurements of SS304 indicated that the emissivity of oxidised samples showed complex behaviours determined by many factors. This rises the request to develop a system with fully controlled atmosphere to simulate the actual gas environment for achieving accurate measurements, particularly applied in precise temperature controlling processes.

A single-point radiation thermometer is not suitable to measure the emissivity distribution of an object with complex surface conditions. To overcome this difficulty, this work has demonstrated a scanning instrument for mapping emissivity across the whole scene of interest. Each pixel on the emissivity map represents an independent emissivity measurement with fully characterised uncertainty estimation. The instrument is designed for producing emissivity maps from 500 to 1100 °C, which is one of the temperature ranges for generating oxide layers. At the first test phase, the function of the instrument has been validated by measuring the emissivity of a unique sample prepared with the checkerboard pattern at 400 °C. This instrument has the potential capability to output live the video of emissivity maps, which will benefit industry to quantitatively trace the emissivity distribution over the whole scene, and, thereafter, to improve temperature measurements.

This work demonstrates the methods to develop high performance radiation thermometers on emissivity measurements. The uncertainty sources have been discussed and analysed thoroughly. The related knowledge, both in optics and radiation thermometry, will also benefit the development of radiation thermometers in temperature measurements in the future.

References

[1] International Organisation for Standardisation, Guide to the Expression of Uncertainty in Measurement (GUM), Geneva: International Organisation for Standardisation, 1995.

Chapter 8. Appendices

8.1 Uncertainty Analysis in Direct Emissivity Measurements

In radiometry, spectral normal emissivity, $\varepsilon(\lambda, T)$, is defined by the ratio of the sample radiance to the blackbody radiance at the same wavelength and temperature. When the spectral normal emissivity is measured by a direct method, it can be derived from Equation (2.17)

$$\varepsilon(\lambda, T) = \frac{L_s(\lambda, T)}{L_b(\lambda, T)} \tag{8.1}$$

where λ is the wavelength, T is the temperature, $L_s(\lambda, T)$ is the radiance from a body, and $L_b(\lambda, T)$ is the radiance from a blackbody. The spectral radiance of a blackbody, $L_b(\lambda, T)$, can be obtained by Equation (2.10).

If radiation thermometers are used to measure emissivity, optical detectors simultaneously receive radiance emitting from a sample and a blackbody and convert them to electrical signals, S_s and S_b. However, the signals detected from a sample and a blackbody are not equal to emitted radiance straightforwardly. The relation of the detected signal and the radiance can be derived from Equation (2.90).

$$S_s(\lambda, T_s) = \Omega_s A_s \tau_{air} \int_{\lambda_1}^{\lambda_2} \varepsilon_s(\lambda, T_s) L_b(\lambda, T_s) R_s(\lambda) \tau_s(\lambda)\, d\lambda \tag{8.2}$$

$$S_b(\lambda, T_b) = \Omega_b A_b \tau_{air} \int_{\lambda_1}^{\lambda_2} L_b(\lambda, T_b) R_b(\lambda) \tau_b(\lambda)\, d\lambda \tag{8.3}$$

where subscript "b" denotes blackbody, "s" denotes sample, Ω is the solid angle, A is the measurement area upon the target, τ_{air} is the propagation coefficient of the atmosphere, $R(\lambda)$ is the relative spectral responsivity of detectors, and $\tau(\lambda)$ is the total transmissivity of the optical path.

The spectral responsivity of a detector and total transmissivity of the optical path of a radiometer are functions of wavelength. If the spectral emissivity is wanted, these two factors can be regarded as independent of wavelength. The propagation coefficient of the atmosphere can be regarded as constant if a radiation thermometer is used to measure emissivity with the same working distance as it is calibrated by a blackbody furnace and under the same atmosphere. Equation (8.1) can be rewritten to

$$\varepsilon_s(\lambda, T_s) = \frac{S_s(\lambda, T_s)}{S_b(\lambda, T_b)} \cdot \frac{\Omega_b A_b R_b(\lambda) \tau_b(\lambda) \varepsilon_{eff,b}(\lambda, T_b) L_b(\lambda, T_b)}{\Omega_s A_s R_s(\lambda) \tau_s(\lambda) L_b(\lambda, T_s)} \tag{8.4}$$

where $L_b(\lambda, T_s)$ is the spectral radiance of an ideal blackbody, $\varepsilon_{eff,b}(\lambda, T_b)$ is the effective emissivity of an approximate blackbody source, and $L_b(\lambda, T_b)$ is the spectral radiance of an ideal blackbody.

Emissivity measurement errors derive from many sources, such as the approximate nature of the blackbody source, characteristics of the radiometers, and the operational procedures. All these errors will change the magnitude, x, in Equation (5.8) and lead to the uncertainty of measurements. Particularly, the uncertainty in emissivity measurements can dominate the overall accuracy of non-contact temperature measurements. The instrumental uncertainty should be analysed comprehensively to provide accurate and traceable emissivity measurements. Otherwise the emissivity uncertainty can lead to unacceptable and unknown overall temperature measurement errors. The individual uncertainty component, $u_i(x)$, can be computed by the derivative of Equation (5.8) with respect of each magnitude

$$u_i(x) = \left|\frac{\partial \varepsilon_s}{\partial x}\right| \cdot \frac{\Delta x}{m} \tag{8.5}$$

where Δx is the error due to the magnitude and m is the divisor with respect of the probability distribution.

The combined standard uncertainty $u_c(x)$ can be given by

$$u_c(x) = \sqrt{\sum_{i=1}^{N} [u_i(x)]^2} \tag{8.6}$$

The expanded uncertainty U can be given by

$$U = ku_c(x) \tag{8.7}$$

where k is the coverage factor.

8.1.1 Effective emissivity of a blackbody source

The effective emissivity of a real blackbody source is always lower than 1. For a calibrated blackbody source, its effective emissivity can be given by the supplier. The effective emissivity is usually given by

$$\varepsilon_{eff,b}(\lambda, T_b) = 1 - \Delta\varepsilon(\lambda, T_b) \tag{8.8}$$

where $\Delta\varepsilon$ is emissivity deviation between a real blackbody source and an ideal blackbody. Assuming $\Delta\varepsilon$ follows the rectangular distribution, the standard uncertainty due to the effective emissivity deviation can be given by

$$u_1(\varepsilon_{eff,b}) = \left|\frac{\partial\varepsilon_s}{\partial\varepsilon_{eff,b}}\right| \cdot \frac{\Delta\varepsilon}{\sqrt{3}} \tag{8.9}$$

If a custom blackbody source is used, its effective emissivity is composed of two main error sources: emissivity deviation under isothermal condition and non-isothermal condition.

8.1.1.1 Effective emissivity of a blackbody source, isothermal

A custom designed blackbody source is not an ideal blackbody, whose effective emissivity can be determined by the wall emissivity, geometry factors, and machining imperfections under isothermal conditions [1, 2]. The geometry of the blackbody cavity may have deviated from the design due to manufacturing errors, leading to the imperfections in the cavity shape. The emissivity deviation, $\Delta\varepsilon_{iso}$, can be measured by a national laboratory or estimated by following the instruction of CCT/03-03 [1]. Assuming $\Delta\varepsilon_{iso}$ follows the rectangular distribution, the standard uncertainty can be computed by

$$u_I(\varepsilon_{eff,b}) = \left|\frac{\partial\varepsilon_s}{\partial\varepsilon_{eff,b}}\right| \cdot \frac{\Delta\varepsilon_{iso}}{\sqrt{3}} \tag{8.10}$$

8.1.1.2 Effective emissivity of a blackbody source, non-isothermal

The effective emissivity of a cavity blackbody decreases under non-isothermal conditions, due to non-uniform thermal distributions along the cavity. This distribution is affected by two factors: the thermally uniform length of the furnace and the heat exchanged between the cavity and its surroundings. The emissivity deviation, $\Delta\varepsilon_{n-iso}$, can be measured by a national laboratory or estimated by following the instruction of CCT/03-03 [1]. Assuming $\Delta\varepsilon_{n-iso}$ follows the rectangular distribution, the standard uncertainty can be computed by

$$u_{II}\left(\varepsilon_{eff,b}\right) = \left|\frac{\partial\varepsilon_s}{\partial\varepsilon_{eff,b}}\right| \cdot \frac{\Delta\varepsilon_{n-iso}}{\sqrt{3}} \tag{8.11}$$

Once the standard uncertainties due to the emissivity deviation under the isothermal and non-isothermal condition are known, the standard uncertainty due to the effective emissivity deviation can be computed by

$$u_1\left(\varepsilon_{eff,b}\right) = \sqrt{u_I^2\left(\varepsilon_{eff,b}\right) + u_{II}^2\left(\varepsilon_{eff,b}\right)} \tag{8.12}$$

8.1.2 Blackbody radiance temperature

Variable temperature blackbodies are commonly used in laboratory calibrations due to their flexibility in emitting radiation in a continuous temperature range, as introduced in Chapter 1.2. For a typical variable temperature blackbody, its radiance temperature is represented by the cavity temperature that is monitored by a thermocouple. The deviation between the actual radiance temperature and desired setpoint temperature is mainly dominated by the accuracy of the thermocouple that is stated as $T \pm \Delta T_b/2$. The deviation range, ΔT_b, is usually given by the thermocouple supplier. Assuming ΔT_b follows the rectangular distribution, the standard uncertainty can be computed by

$$u_2(T_b) = \left|\frac{\partial\varepsilon_s}{\partial L_b}\right| \cdot \left|\frac{\partial L_b}{\partial T_b}\right| \cdot \frac{\Delta T_b}{\sqrt{3}} \tag{8.13}$$

where ΔT_b is the deviation range of a thermocouple used to measure the temperature of a blackbody.

8.1.3 Sample radiance temperature

The true sample surface temperature is unknown during emissivity measurements. A thermocouple is usually placed as close as to the sample surface. The temperature of the sample substrate is used to represent the sample radiance temperature. The uncertainty evaluation is similar to Chapter 8.1.2. By assuming ΔT_s follows the rectangular distribution, the standard uncertainty can be computed by

$$u_3(T_s) = \left|\frac{\partial \varepsilon_s}{\partial L_b}\right| \cdot \left|\frac{\partial L_b}{\partial T_s}\right| \cdot \frac{\Delta T_s}{\sqrt{3}} \tag{8.14}$$

where ΔT_s is the deviation range of a thermocouple used to measure the temperature of a sample.

8.1.4 Temperature deviation between the sample and the blackbody cavity

In actual measurements, the true radiance temperature of a sample surface is not identical to the temperature indicated by a thermocouple. The deviation is due to various sources, for example, the temperature interference by approaching a cold shield to block the background radiation, the temperature interference by using a gold reflector to enhance the emission, and the existance of the thermal gradient along the sample substrate. The radiance temperature deviation between a sample and a blackbody is inevitable though both their thermocouples indicate the identical temperature. Hence, the deviation, ΔT, can be estimated by precision measurements or numerical simulations, which should be undertaken case by case. By assuming ΔT follows the rectangular distribution, the standard uncertainty can be computed by

$$u_4(T_{Dev}) = \left|\frac{\partial \varepsilon_s}{\partial L_b}\right| \cdot \left|\frac{\partial L_b}{\partial T}\right| \cdot \frac{\Delta T}{\sqrt{3}} \tag{8.15}$$

where ΔT is the radiance temperature deviation range between a sample and a blackbody.

8.1.5 Size of source effect

The size of source effect (SSE) describes the phenomenon that a radiometer receives radiation from the region outside the nominal measurement area. In radiation

thermometry, the nominal measurement area is defined as the size of a diffuse surface area which encloses 90% (or above) radiant energy at a given working distance, by comparing that with the size of infinite measurement area. SSE arises as a consequence of optical aberrations, diffractions, reflections and scattering between lens interfaces [3]. If SSE is measured by the direct method, the deviation of radiance, ΔL, received by a radiation thermometer comparing to that emitted from the nominal measurement area can be given by Equation 2.98

$$\Delta L(\lambda, T_b) = |1 - \sigma_{SSE}(r, r_{max})| \cdot L_b(\lambda, T_b) \tag{8.16}$$

where $\Delta L(\lambda, T_b)$ is the deviation of radiance, and $\sigma_{SSE}(r, r_{max})$ is the value of SSE when $S(r,\ L) \geq 90\% S(r_{max},\ L)$.

By assuming ΔL follows the rectangular distribution, the standard uncertainty can be computed by

$$u_5(L_{SSE}) = \left|\frac{\partial \varepsilon_s}{\partial L}\right| \cdot \frac{\Delta L}{\sqrt{3}} \tag{8.17}$$

8.1.6 Responsivity correction

For emissivity measurements, radiance emitted from a sample and a blackbody should be captured and converted to electrical signals by using radiation thermometers. Their spectral responsivities are slightly different due to the variation in spectral response of photodiodes. If multiple radiation thermometers are used, their spectral responsivity curves should be characterised and corrected. A conventional method is to select a reference radiation thermometer and use its spectral responsivity curve to correct the rest radiation thermometers by using linear least squares method [4]. The uncertainty can be evaluated from the maximum residual, ΔR_{RES}, by assuming it follows the rectangular distribution

$$u_6(R) = \left|\frac{\partial \varepsilon_s}{\partial R}\right| \cdot \frac{\Delta R_{RES}}{\sqrt{3}} \tag{8.18}$$

where ΔR_{RES} is the deviation range of the maximum residual of the spectral responsivity curves fitting.

8.1.7 Electronic noise

The radiation thermometer output fluctuated during the course of the measurement, adding additional uncertainty due to electronic noise. Electronic noise generates the error in multiple measurements, leading to the uncertainty, $u_7(S)$. This uncertainty follows the normal distribution and can be estimated by repeat measurement.

$$u_6(S) = \left|\frac{\partial \varepsilon_s}{\partial S}\right| \cdot \Delta S_{SD} \tag{8.19}$$

where ΔS_{SD} is the standard deviation of repeat measurements due to electronic noise.

8.1.8 Drift

The spectral responsivity of a radiation thermometer is known to change over time due to many impacts including the aging of detector sensors and readout circuits. The drift may change the output signal of a radiation thermometer continuously over a long period or cause a jump of output signal suddenly. In general, a radiation thermometer is required to be calibrated regularly if it is required to work for a long period. The uncertainty due to drifts, $u_8(S)$, can be estimated by the calibration, by assuming it follows the rectangular distribution.

$$u_6(S) = \left|\frac{\partial \varepsilon_s}{\partial S}\right| \cdot \Delta S_{Drift} \tag{8.20}$$

where ΔS_{Drift} is the maximum variance of the output signal due to drifts.

8.1.9 Positioning

For each measurement, samples should be loaded into the instrument for heating. Radiation thermometers should be aligned to a sample and a blackbody. The actual working distance and viewing direction of the radiation thermometer cannot be maintained identical for each measurement, introducing the uncertainty due to positioning errors. The variations of the working distance and viewing direction change both the solid angle and the size of measurement area simultaneously. For example, the decrease of working distance increases the solid angle whilst decreasing the size of the measurement area. The variation of solid angle can be computed straightforwardly, as

discussed in Section 2.2.1. However, the size of the measurement area depends on many parameters, as discussed in Section 2.4.3. A convenient method is to assume these two factors are independent with each other though it will overestimate the overall uncertainty. Thereafter, the uncertainty, $u_{III}(\Omega)$, due to the variation of solid angle, $\Delta\Omega$, can be estimated by assuming follow the rectangular distribution

$$u_{III}(\Omega) = \left|\frac{\partial \varepsilon_s}{\partial \Omega}\right| \cdot \frac{\Delta\Omega}{\sqrt{3}} \tag{8.21}$$

where $\Delta\Omega$ is the variation of solid angle due to the positioning error.

$$u_{IV}(A) = \left|\frac{\partial \varepsilon_s}{\partial A}\right| \cdot \frac{\Delta A}{\sqrt{3}} \tag{8.22}$$

where ΔA is the variation of the size of the measurement area due to the positioning error.

The uncertainty due to positioning error can be computed by

$$u_9(L_p) = \sqrt{u_{III}^2(\Omega) + u_{IV}^2(A)} \tag{8.23}$$

8.1.10 Combined standard uncertainty

The combined standard uncertainty can be computed by Equation (5.9) that offers a confidence level of approximately 68%. In this work, the coverage factor was selected as 2, which gives the expanded uncertainty with the level of confidence of approximately 95%.

This chapter focuses on the analysis of uncertainty due to the common error sources. However, uncertainties may be introduced by various error sources for actual measurements. The comprehensive uncertainty budget should be analysed case by case for a specific instrument, which will be given in each instrumental design chapter in this work.

References

[1] Land Instruments International, "SPOT Brochure-Specification and design," [Online]. Available: https://www.ametek-land.com/-/media/ameteklandinstruments/documentation/products/fixedspotnoncontactthermometers/spot/ametek_land_spot_brochure_marcom0355_rev_15.pdf, 2017.

[2] M. Vollmer, and K.-P. Möllmann, *Infrared thermal imaging: fundamentals, research and applications*: John Wiley & Sons, 2017.

[3] M. J. Hobbs *et al.*, "Quantitative thermal imaging using single-pixel Si APD and MEMS mirror," *Opt. Express,* vol. 26, no. 3, pp. 3188-3198, Feb 5, 2018.

[4] V. Milanovic, "Linearized gimbal-less two-axis MEMS mirrors," in *Optical Fiber Communication Conference*, 2009, pp. JThA19.

[5] H. W. Yoon, D. W. Allen, and R. D. Saunders, "Methods to reduce the size-of-source effect in radiometers," *Metrologia,* vol. 42, no. 2, pp. 89-96, 2005.

[6] Aremco Products Inc., "High Temperature Specialty Coatings. Valley Cottage," [Online]. Available: www.aremco.com/wp-content/uploads/2015/06/TechNote-840-M.pdf, 2015.